NASA CR-159441
AiResearch 31-2935-1

FINAL REPORT

ANALYSIS, DESIGN, FABRICATION AND TESTING OF THE MINI-BRAYTON ROTATING UNIT (MINI-BRU)

VOLUME I - TEXT AND TABLES

by F. X. Dobler, et al

AIRESEARCH MANUFACTURING COMPANY OF ARIZONA
A DIVISION OF THE GARRETT CORPORATION
Phoenix, Arizona

Prepared for

NATIONAL AERONAUTICS AND SPACE ADMINISTRATION

NASA Lewis Research Center
Contract NAS3-18517

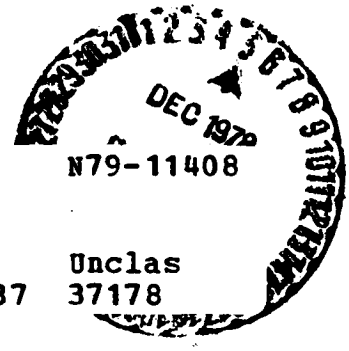

1. Report No.	2. Government Accession No.	3. Recipient's Catalog No.
NASA CR-159441		

4. Title and Subtitle	5. Report Date
Analysis, Design, Fabrication and Testing of the Mini-Brayton Rotating Unit (Mini-BRU)	October 1978
	6. Performing Organization Code

7. Author(s)	8. Performing Organization Report No.
F. X. Dobler, et al	31-2935
	10. Work Unit No.

9. Performing Organization Name and Address	11. Contract or Grant No.
AiResearch Manufacturing Company of Arizona 111 South 34th Street Phoenix, Arizona 85010	NAS3-18517
	13. Type of Report and Period Covered Contractor Report - April 1974 - June 1978

12. Sponsoring Agency Name and Address	14. Sponsoring Agency Code
NASA-Lewis Research Center 21000 Brookpark Rd. Cleveland, Ohio 44135	

15. Supplementary Notes

Program Manager, J. H. Dunn
NASA-Lewis Research Center

16. Abstract

A 500- to 2100-watt power output Mini-Brayton Rotating Unit (Mini-BRU) was analyzed, designed, fabricated and tested. Performance and test data for the various components is included. Components tested include the 2.12 in. diameter compressor, the 2.86 in. diameter turbine, the Rice alternator and the cantilevered foil-type journal and thrust bearings. Also included are results on the fabrication of a C-103 turbine plenum/nozzle assembly and on offgassing of the organic materials in the alternator stator.

17. Key Words (Suggested by Author(s))	18. Distribution Statement
Isotope Power Conversion System Radial Compressors, Radial Turbine, Rice Alternator, Columbium, Foil Bearings, Brayton Rotating Unit	Unclassified - Unlimited

19. Security Classif. (of this report)	20. Security Classif. (of this page)	21. No. of Pages	22. Price*
Unclassified	Unclassified	Volume I-221 Volume II-447	

* For sale by the National Technical Information Service, Springfield, Virginia 22161

FOREWORD

The work reported herein was conducted under NASA CONTRACT NAS3-18517 over the period from April, 1974 through June, 1978.

This report consists of two volumes:

Volume I - Text and Tables

Volume II - Figures and Drawings

During the period from 1 January 1978 through 30 June 1978 an intensive development effort was conducted to solve a fail journal bearing problem which occurred during integrated system testing under a DoE program (Contract EY-76-C-03-1173 Reference 44). That bearing development work, although conducted under an extension of this program, is reported separately in Reference 45.

TABLE OF CONTENTS

TABLE OF CONTENTS (Contd)

TABLE OF CONTENTS (Contd)

SUMMARY

Analysis and design were conducted to synthesize a Brayton Rotating Unit capable of producing from 500 to 2100 watts of electrical output power when operating in a closed Brayton cycle power system. This unit has been subsequently referred to as the Mini-BRU.

The unit was designed as a compact, high power density unit with foil type journal and thrust bearings. An innovative design was the placement of the journal bearings in the secondary magnetic flux gap to minimize the rotor length. The rotating group utilized a single stage radial outflow compressor, a single stage radial inflow turbine with a Rice alternator rotor between.

Specific tasks were conducted to design, fabricate, and test the compressor stage, the turbine stage, the bearings, the alternator stator, the bimetallic brazed alternator rotor, and the C-103 turbine plenum/nozzle assembly. Attendant thermal and stress analyses were also conducted to assure the structural integrity of the components. Additionally, tasks were completed to characterize the nature and quantity of effluents from the organic materials in the alternator stator during operation and to characterize some of the problems associated with integrating the Mini-BRU into a space dynamic power system.

The latter task was subsequently extended by the United States Department of Energy wherein the Mini-BRU was integrated into a prototype Brayton Isotope Power System and successfully tested for 1000 hours, achieving predicted overall cycle efficiency.

INTRODUCTION

From the early 1960's to the present, numerous design studies and hardware development programs were conducted to develop "technology readiness" for the closed Brayton cycle in anticipation of future space mission requiring dynamic power conversion systems. Of significance was the NASA-Brayton Rotating Unit program in which a 10 kW_e closed gas turbine was developed and successfully tested at the NASA-Lewis Research Center for over 38,000 hours of operation with a cycle efficiency of 30 percent.

In 1972, the NASA sponsored a study in which many candidate space power conversion systems were evaluated for mission requirements from 200 to 2500 W_e. As a result, the closed Brayton cycle was identified as a favored system due to its high cycle efficiency, compatibility with nuclear heat sources, high reliability, growth potential, design flexibility (modularization and/or scalability potential) and advanced development status.

Subsequently, a study contract was awarded by the NASA to define in more detail a system that could be modularized to operate with high efficiency and near minimum weight over the whole range of desired power output; hence, the origin of the all-purpose Mini-BRU (Miniature Brayton Rotating Unit) concept. Later, a system study was conducted to define a complete space power conversion system in the same power range. The results of these studies led to the award, in 1974, of the NASA sponsored Mini-BRU, recuperator, and Heat Source Assembly hardware programs. In June 1975, the Brayton Isotope Power System (BIPS) Phase I program for the development of a system integrating the components was awarded to AiResearch by DoE.

This report, summarizes the 51 month program sponsored by the NASA-Lewis Research Center to analyze, design, fabricate, test and deliver two Brayton Rotating Units (hereafter referred to as Mini-BRU) capable of producing from 500 to 2100 watts of electrical power.

The Mini-BRU, shown in Figure 1 was subsequently integrated into a Brayton Isotope Power System (BIPS) under DOE sponsorship (Ref. Contract EY-76-C-03-1173).

This baseline system is a 7 year life, 450 lb, 1300 We unit using Brayton cycle hardware developed for the NASA LeRC and two 2400 Wt multi-hundred watt isotope heat sources developed for DoE.

The Mini-BRU design combines ruggedness and simplicity thus engendering reliability. The component parts of the unit are

shown in Figure 2. A radial inflow turbine, radial outflow compressor and brushless four pole Rice alternator shaft are combined on a common shaft with a total of only eight parts. The shaft rotates at 52,000 rpm on foil journal and thrust bearings.

The Mini-BRU design is flight prototypical and easily adapted to any attitude thus making it compatible with systems for a wide variety of applications.

The first Mini-BRU unit delivered under this contract has successfully completed a 1000 hour test in the Brayton Isotope Power System utilizing electrical heaters to produce 1200 kW_e at 1385°F turbine inlet temperature. This test was conducted from 4 April 1978 through 22 May 1978.

DESIGN PARAMETERS, COMPONENT PERFORMANCE AND SYSTEM PERFORMANCE

The design analysis was conducted in accordance with the specifications set forth in the contract work statement. System analysis were conducted to determine performance at various power levels.

Design Requirements

The Mini-BRU package shall consist of a radial-flow turbine, a radial-flow compressor, and a radial gap alternator mounted on a common shaft rotating nominally at 52,000 rpm and supported on gas lubricated hydrodynamic journal and thrust bearings. The Mini-BRU shall produce up to 2.4 kW_e gross power. The alternator shall be cooled by the working fluid from the compressor discharge. The complete unit shall include a flight-type housing and turbine and compressor inlet and exit ducting. Mounting pads shall be provided to permit the unit to be installed in a space power system. The unit shall include bases or pads machined for the required instrumentation.

The Mini-BRU shall be designed for ease of assembly and disassembly such that alteration and replacement of major components is facilitated. The components shall be designed to maintain high efficiency over the entire specified rated power output range.

The following design requirements shall be employed in the design of the Mini-BRU:

General Requirements

(1) Unit optimized for operation at conditions of Case IV (Table I)

(2) 52,000 rpm single shaft, radial flow turbine and compressor, radial gap alternator

(3) Cycle working fluid - He-Xe (molecular weight = 83.8)

(4) 10 year design life at maximum rated power and turbine inlet temperature in space vacuum

(5) 1000 start-stop thermal cycle capability

(6) Capable of delivering power over the range of 300 - 2400 watts electric

TABLE I. - NOMINAL REFERENCE OPERATING CONDITIONS

[The following table defines the expected performance of the Mini-BRU at its nominal reference operating conditions.]

	CASE			
	I	II	III	IV
Alternator output power, kw	0.350	0.696	1.509	2.162
Gross cycle efficiency, percent*	0.236	0.29	0.314	0.300
Compressor efficiency, percent	0.755	0.758	0.760	0.76
Turbine efficiency, percent	0.780	0.797	0.820	0.832
Alternator efficiency, percent	0.85	0.902	0.921	0.917
Lost pressure ratio parameter (β)	0.947	0.961	0.975	0.980
Recuperator effectiveness (E_r)	0.973	0.980	0.980	0.975
Compressor inlet temperature, °R	458.	468.5	501.2	534.2
Compressor inlet temperature, psia	12.8	20.9	44.	70.6
Compressor pressure ratio	1.61	1.59	1.54	1.5
Bearing loss, kw	0.098	0.116	0.147	0.184
Windage loss, kw	0.013	0.020	0.038	0.056
Compressor flow rate, lb/sec	0.071	0.117	0.235	0.357
Turbine inlet temperature, °R	2060.	2060.	2060.	2060.
Rotating group speed, rpm	52000.	52000.	52000.	52000.

*Gross Cycle Efficiency = $\frac{\text{GROSS OUTPUT AT ALTERNATOR TERMINALS}}{\text{TOTAL HEAT AVAILABLE}}$

(7) Ease of assembly and disassembly such that alteration and replacement of major components is facilitated

(8) Flight-type housing and turbine and compressor inlet and exit ducting

(9) Environmental conditions as stated in work statement, Section E

(10) No separate cooling loop

(11) Overspeed capability to 120 percent design speed

(12) Interchangeable superalloy and refractory metal turbine scrolls with minimum of rework

Alternator Requirements

(1) Stationary excitation coil, brushless, Rice type Lundell alternator

(2) Optimized for performance over the range of 1/2 to 3 heat source capsules

(3) Maximum continuous power - 2400 watts net dc

(4) Voltage - 120 vdc

(5) Series and shunt wound field coils

(6) Vacuum impregnated organic insulated windings

(7) Maximum hot spot temperature - 400°F

(8) Motoring start capability

(9) Phase balance and short circuit capability per MIL-G-21480 as modified by work statement

Gas Bearings Requirements

(1) Minimum power loss

(2) All attitude in 1-G field

(3) Dry starting (no hydrostatic start)

(4) Breakaway (starting) torque consistent with motoring start capability

Instrumentation Requirements

(1) Three magnetic speed pickups installed in the compressor shroud and sensing compressor impeller blade passing frequency

(2) A flux coil consisting of one full pole pitch

(3) Two static pressure taps, one each in the compressor and turbine

(4) A total of nine thermocouples located in the alternator stator

(5) Thermocouples located at each journal bearing and on each face of the thrust bearing

ENGINE DESIGN AND DEVELOPMENT

Engine Design

Layout studies were conducted concurrently with design analysis of the various subassemblies and components. The final configuration, shown in Drawing 240610, conforms to the expected rugged Brayton design and meets every design criteria. This design was evolved from the baseline configuration originally presented in the program proposal.

The component arrangement was based on the highly successful BRU configuration designed and developed under contract NAS3-9427. The Mini-BRU was in reality, an extension of the BRU design. The basic changes were as follows:

(1) A plenum rather than an involute scroll was used for the turbine inlet.

(2) The journal bearings were located in the Rice alternator secondary gap to minimize the bearing span and to increase the rotor bending critical frequency.

(3) The journal and thrust bearings were cooled primarily by conduction to the alternator frame and compressor.

(4) The alternator was cooled by heat conduction to the compressor discharge gas stream via a finned axial heat exchanger at the alternator outer diameter.

(6) Foil journal and thrust bearings were the baseline design.

(7) The turbine plenum design was such that Columbium alloy C-103, Hastelloy X or Waspaloy versions could be fabricated and used interchangeably depending on the system requirements.

Materials Selection

Mini-BRU materials were selected on the basis of the following guidelines:

(1) Duty cycle and environment

(2) BRU experience

(3) Past experience on other engines on programs

Table II lists the materials used in the Mini-BRU along with the function and basis for selection. Drawing 3604335 shows the materials utilization within the unit.

Engine Assembly and Conformance Tests

Engine assembly. - The first Mini-BRU unit was assembled in accordance with engineering assembly instructions written specifically for this engine. Instrumentation was installed per Drawing SKP32488.

These instructions detailed methods of determining the required shimming dimensions and specified critical dimensions to be recorded. This procedure is very simple and once established, repeatable builds could be obtained.

The engine assembly was accomplished with virtually no rework required to any parts. This excellent hardware compatibility resulted largely from the design philosophy applied throughout the program that all development test rig component hardware was to be interchangeable with engine assembly hardware. This allowed major fabrication development to be accomplished on rig hardware.

This philosophy paid off many times. For example, the compressor test rig diffuser shroud assembly serves as a development test bed for the BIPS motoring start control which utilized the speed pickup sensing from the compressor wheel. This whole subassembly could be assembled on to the alternator test rig so that the correct rotor inertia and magnetic and field effect could be included.

During preconformance engine testing, and for tests out of the loop, the turbine test rig stainless steel plenum/nozzle assembly was used to drive the rotor when neither the Waspaloy or C-103 plenums were available.

Engine conformance testing. - Mini-BRU Engine, S/N 01, was conformance tested on April 6 and 7, 1977. The unit performed flawlessly through 5 hours of 100 percent speed (52,000 rpm) and 5 minutes of 120 percent speed (62,400 rpm) operation. Following this, electrical phase sequence, phase unbalance and field time constant test were performed. This was followed by a motor start using the ramped frequency induction start control developed for the ERDA BIPS program. A completely assembled Mini-BRU ready for delivery is shown in Figure 3.

Component Performance

Table III summarizes the tested component performance as measured against the initial design goals.

TABLE II - MINI-BRU MATERIALS.

Item No.	Description	Materials	Function	Basis for Selection
1	Impeller, Comp.	CRES 410	Gas Compression	Good Strength Good Thermal Conductivity
2	Tie Bolt	INCO 718	Retain Rotor Assy.	Good Combination of Strength and Fatigue Properties
3	Nut, Tie Bolt	4340 Steel	Retain Rotor Assy	Good Strength
4	Washer, Tie Bolt	CRES 347	Locks Item 3	Past Experience
5	Rotor, Thrust Brg.	6260 Steel	Thrust Support	Strength and High Hardness
6	Wheel, Turbine	INCO 713LC or Astroloy	Energy Extraction	Past Experience - High Temp. Strength & Fabricability
7	Rotor, Alternator	HP9-4-20,713LC	Interrupt Flux Field	Past Experience with TAC
8	Heat Shunt	Copper	Conduct Heat from Thrust Rot. to Comp. Impeller	High Thermal Conductivity
9	Foil Bearing, Journal	CRES 302 Teflon Coated	Radial Shaft Support	Past Experience
10	Foil Bearing, Thrust	CRES 302 Teflon Coated	Axial Shaft Support	Past Experience
11	Spring, Foil Brg.	CRES 302	Foil Leaf Support	Past Experience
12	Sleeve, Foil Brg. Comp.	4340 Steel	Retain Foil Leafs	Thermal expansion Compatibility
13	Sleeve, Foil Brg. Turbine	4340 Steel	Retain Foil Leafs	Thermal Expansion Compatibility
14	Ret. Foil Journal	CRES 300	Retain Foil Leafs	Good Fabricability Low Cost
15	Plate, Thrust Brg.	17-4PH Stainless	Thrust Brg Support	High Strength - Good Fatigue Compatible Thermal Experience
16	Shim, Thrust Bearing	CRES 300	Control Thrust Bearing Clearance	Corrosion Resistance, Low Cost
17	Spacer, Thrust Brg.	17-4PH Stainless	Space Thrust Plates	Thermal Expansion Compatibility
18	Shim, Comp.	CRES 300	Control Compressor Clearance	Corrosion Resistance, Low Cost
19	Seal Comp. Back Shroud	CRES 347	Control Gas Circulation on Backside of Rotor	Corrosion Resistance, Good Fabricability
20	Inlet, Comp.	CRES 347	Channel Gas Flow	Corrosion Resistance, Good Fabricability
21	Diffuser, Comp.	CRES 17-4PH	Increase P_s	Corrosion Resistance, Good Fabricability, High Strength
22	End Bell, Comp.	1018 Steel	Channel Magnetic Flux	Good Magnetic Properties Good Thermal Conductivity
23	End Bell, Turbine	1018 Steel	Channel Magnetic Flux	Good Magnetic Properties Good Thermal Conductivity
24	Housing, Alternator	1018 Steel, CRES 347	Channel Magnetic Flux	Good Magnetic Properties Good Thermal Conductivity
25	Turbine, Back Shroud	C-103	Control Gas Circulation on Backside of Rotor	High Temperature Capability
26	Plenum, Turb.	C-103/Waspaloy	Channel Turbine Gas	High Temperature Strength and Creep Life
27	Field Coil Bobbins	Al 2024	Contain Field Windings	Good Thermal Conductivity Nonmagnetic
28	Shim, Turbine	CRES 300	Control Turbine Clearance	Corrosion Resistance, Low Cost
29	Ring, Hermetic Seal	CRES 347	Gas Seal to Atmosphere	Corrosion Resistance, Good Weldability
30	Ring, Hermetic Seal	CRES 347	Gas Seal to Atmosphere	Corrosion Resistance, Good Weldability
31	Shim Alt. Adj.	CRES 300	Control Alternator Position	Corrosion Resistance, Low Cost
32	Cover, , -2 Alt Leads -1	CRES 347	Protect Alternator Terminals	Corrosion Resistance, Low Cost
33	Orifice, Bleed Flow	CRES 347	Meter Turbine Bearing Cooling Gas Flow	Corrosion Resistance, Low Cost
34	Stack Laminations	AL4750 Steel	Channel Magnetic Flux	Good Magnetic Permeability
35	Coating, Foil Bearings	Teflon-S	Reduce Friction During Startup	High Temperature Capability, Low Friction Durability

TABLE III. - MINI-BRU COMPONENT PERFORMANCE.

Component	Design goal	Test result
Compressor	η_{T-T} = 75.8% $\frac{W\sqrt{\theta}}{\delta}$ = 0.0753 lb/sec	η_{T-T} = 77% $\frac{W\sqrt{\theta}}{\delta}$ = 0.0753 lb/sec
Turbine	η_{T-T} = 83.4% $\frac{W\sqrt{\theta}}{\delta}$ = 0.0996 lb/sec	η_{T-T} = 83.6% $\frac{W\sqrt{\theta}}{\delta}$ = 0.1031 lb/sec
Alternator	η_{DC} = 85.13 @ 1.928 kW_e Max starting torque = (1.67) X (bearing start torque) Voltage out = 120 vdc Current out = 16.3 adc Max temp = 214°F	η_{DC} = 84.19% @ 1.928 kW_e Max starting torque 3.0 in-lb Voltage out = 120.6 vdc Current out = 16.43 adc Max temp = 183°F
Journal bearings	Design point Power loss = 38.2 watts/brg	Design point Power loss = 45 watts*/brg
Thrust bearing	Design point Power loss = 77.5 watts	Design point Power loss = 110 watts*
Bearing Start Torque	T = (0.6) X (available alternator motoring start torque)	Start torque = 1.75 in-lb

* Based on test data obtained in air, krypton and argon and translated to Xe-He

In every case except alternator efficiency and bearing power loss the design goal was met or exceeded.

System Performance Analysis

Introduction and summary. - Throughout the design effort, system analysis was conducted to assess the effects of small changes in component performance or efficiency on overall system performance.

At the completion of the interim design review, the latest design information was input into the cycle analysis program to determine the off-design component performance and cycle state points at 7200 Wt, 4800 Wt, and 2400 Wt. The results from this study vary almost imperceptibly from the original design study.

Presented in this section are sensitivity studies of key parameters. A general observation regarding this data is that the system performance is not particularly sensitive to the performance of any individual component.

Mini-BRU performance at 1, 2 and 3 heat source modules (2400 Wt each), each having 10 percent thermal loss, ranges from 27 to 30 percent. This efficiency also includes parasitic power losses relating to power conditioning.

Discussion. - The most radical departure from the original preliminary design involves the philosophy of the thermal design. Extensive analysis revealed impingement cooling of the thrust bearing rotor was no longer required. The final design employs bleeding 2 percent flow at the exit of the alternator heat exchanger and injecting this into the turbine end journal bearing. The compressor end journal bearing and thrust rotor will utilize the compressor, front endbell, and the alternator as a heat sink. The bearing cooling mechanism is shown in Figure 4. The thermal analysis has not shown the exact split of the heat flux. Cycle analysis indicates that this split has negligible effect on performance and, therefore, all of the heat from the front bearings is assumed to enter the compressor. The commensurate increase in compressor inlet temperatures is considered in the compressor design. The windage, electromagnetic losses and turbine end bearing loss are absorbed completely by the working fluid in the alternator heat exchanger. The bleed flow enters the rear bearing and counteracts the heat flux from the turbine wheel. It is pumped up the backface of the turbine into the turbine inlet.

No credit is taken from the work available in this fluid for the sake of conservatism. It is assumed to mix with the main stream fluid at the turbine exit; hence the difference between turbine exit temperature and recuperator LP inlet temperature as shown in Tables IV through VI.

TABLE IV. - MINI-BRU DESIGN POINT - 7200 W_T

Net Output	2.079 KW	Net System Efficiency	.289
Control Output	.059 KW	Working Fluid	Xe/He (83.8)
Gross Output	2.138 KW	Shaft Speed	52,000 rpm
Bearing Loss	.154 KW	Lost Pressure Ratio	.98
Windage Loss	.085 KW	Alternator Efficiency	.92

Component	Flow lb/sec	T_{in} °R	T_{out} °R	P_{in} PSIA	P_{out} PSIA	EFF	P/P %	Comments
Compressor	.363	542	665	71.7	107.0	.761		Bearing heat added r_c = 1.491
Alternator HX	.363	665	679	107.0	106.9		.1	Bleed flow exits
Recuperator HP	.355	679	1768	106.9	106.6	.975	.22	
Heater	.355	1768	2060	106.6	106.4		.2	
Turbine	.355	2060	1819	106.3	72.8	.832		r_t = 1.461
Recuperator LP	.363	1796	728	72.6	72.3	.955	.46	
Radiator	.363	728	537	72.3	71.7		.70	

Recuperator Total Pressure Drop = .69%

TABLE V. - MINI-BRU AT 4800 W_T

Net Output	1.441 KW	Net System Efficiency	.30
Control Power	.042 KW	Working Fluid	Xe/He (83.8)
Gross Output	1.483 KW	Shaft Speed	52,000 rpm
Bearing Loss	.139 KW	Lost Pressure Ratio	.975
Windage Loss	.058 KW	Alternator Efficiency	.927

Component	Flow lb/sec	T_{in} ^oR	T_{out} ^oR	P_{in} PSIA	P_{out} PSIA	EFF	P/P %	Comments
Compressor	.239	511	635	45.	68.8	.761		Bearing Heat Added r_c = 1.528
Alternator HX	.239	635	649	68.8	68.7		.1	
Recuperator HP	.235	649	1765	68.7	68.5	.98	.31	
Heater	.235	1765	2060	68.5	68.3		.3	
Turbine	.235	2060	1811	68.2	45.8	.82		r_t = 1.49
Recuperator LP	.239	1787	693	45.7	45.4	.96	.67	
Radiator	.239	693	504	45.4	45.0		.78	

Recuperator Total Pressure Drop = .98%

TABLE VI. - MINI-BRU AT 2400 W_T

Net Output	.656 KW	Net System Efficiency	.273
Control Power	.021 KW	Working Fluid	Xe/He (83.8)
Gross Output	.677 KW	Shaft Speed	52,000 rpm
Bearing Loss	.126 KW	Lost Pressure Ratio	.964
Windage Loss	.032 KW	Alternator Efficiency	.909

Component	Flow lb/sec	T_{in} °R	T_{out} °R	P_{in} PSIA	P_{out} PSIA	EFF	P/P %	Comments
Compressor	.120	483	608	21.8	34.1	.76		Bearing Heat Added r_c = 1.567
Alternator HX	.120	608	625	34.1	34.1		.1	Bleed Flow Exits
Recuperator HP	.118	625	1767	34.1	33.9	.983	.53	
Heater	.118	1767	2060	33.9	33.7		.6	
Turbine	.118	2060	1810	33.7	22.3	.798		
Recuperator LP	.120	1786	667	22.2	22.0	.963	1.17	
Radiator	.120	667	470	22.0	21.8		.9	

Recuperator Total Pressure Drop = 1.69%

Updated loss predictions for the bearings were incorporated in the computer model as required. This curve is flatter than had been previously estimated and is lower at the 2 kW_e level and higher at the 700 W_e level.

The control and parasitic losses were incorporated into the model to allow direct calculation of the dc output. This assumes a doubly redundant rectifier as specified by NASA.

At the same time, the latest alternator performance curve and compressor and turbine maps were incorporated.

The geometry and weight of the radiator and recuperator were taken from the work conducted under the Mini-BRU Preliminary Design Study. The pressure drop in the heat source was also the same as in that study. The percent pressure drop of the ducts was assumed to be constant regardless of power level.

Results. - A summary of the state points and component performance is given in Tables IV through VI. The corresponding cycle schematics are Figures 5 through 7. As can be seen in these charts, the system performance ranges from 27 to 30 percent. If this is compared with Table IV, only small changes are apparent. The alternator windage has increased, but this has been cancelled by the increase in alternator efficiency and decrease in bearing loss. It should be noted that the control and parasitic losses are not included in Table IV but are included in the results presented in these figures. The increase in compressor inlet temperature is a result of the front bearing heat being absorbed by the compressor; this is an "effective" change in temperature and cannot actually be measured.

The heat flux actually enters the compressor midway in the flow path, but due to the low tangential velocity here, very little work has yet been transferred to the fluid. Hence, this initiated the decision to change the compressor inlet temperature. Changes in other parameters are insignificant.

Table VII shows the effect on system performance due to small changes in component performance. The compressor and turbine have the most significant effect on system performance; therefore, justification exists for optimizing their performance as much as possible. Increasing alternator efficiency will also significantly increase system performance.

Mini-BRU Physical Data

The weight of the assembled Mini-BRU including a Waspaloy turbine plenum is 36.7 lb. The rotating group weight is 2.566 lb and the polar moment of inertia is 0.00127 in-lb-sec^2.

TABLE VII. - MINI-BRU PERFORMANCE SENSITIVITY

Nominal Performance @

Turbine Inlet Temperature = 1600°F
Compressor Efficiency = 76%
Turbine Efficiency = 83%
Alternator Efficiency = 92%

Capsules	3	2	1
Overall Cycle Efficiency (%)	28.9	30.0	27.3
Output Power (KW)*	2.08	1.44	0.656

*Doubly redundant rectifier is assumed.

	Performance	Sensitivity	
Variable	ΔVariable	Δηcy (pts)	
Turbine Inlet Temperature (T_6)	-100°	-2.	0.02 pts η_{cy}/°TIT
	-200°	-4.4	0.022
Compressor Efficiency	-2 pts		
TIT = 1600°F		-1	0.5 pt η_{cy}/pt η_c
1500°F		-1.1	0.55
1400°F		-1.2	0.60
Turbine Efficiency	-2 pts		
TIT = 1600°F		-1.1	0.55 pt η_{cy}/pt η_t
1500°F		-1.2	0.6
1400°F		-1.2	0.6
Alternator Efficiency	-2 pts		
TIT = 1600°F		-0.6	0.3 pt η_{cy}/pt η_a
1500°F		-0.6	0.3
1400°F		-0.6	0.3

(i.e., TIT has no effect on alternator performance sensitivity)

Bearing Loss	100% increase in thrust bearing loss	
3 capsules		-1.2 pts in η_{cy}
2 capsules		-1.7
1 capsule		-3.1

(TIT has no effect on sensitivity)

The center of gravity of the unit is located 5.75 inches aft of the compressor inlet flange.

Table VIII shows the specific physical data for the unit.

The cross section of the assembled unit is shown in Drawing 240610; the unit outline drawing is shown in Drawing 240611.

TABLE VIII. - MINI-BRU PHYSICAL PARAMETERS

Design Rotational Speed, rpm	52,000	
Allowable Overspeed, rpm	62,400	
Output Voltage, Design, V_{L-N} (ac)	65.9	
Output Amps, Design (ac)	12.27	
Output Power, kW Maximum	2,100	
Alternator Frequency, Hz	1,733	
Turbine Inlet Temperature, Maximum, °F	1,600	(Refractory System)
	1,400	(Superalloy System)

COMPRESSOR DEVELOPMENT

The design and test of the compressor stage was conducted in two phases. The initial design incorporated a cascaded diffuser design which tested several points low in efficiency. Consequently the diffuser was redesigned as a more conventional single stage diffuser which exceeded the required stage efficiency goal.

Compressor Stage Design

Design point summary. - A summary of the design point parameters is as follows:

Impeller		Stage	
Gas	= Xe-He; MW = 83.8	η	= 0.758
$W\sqrt{\theta}/\delta$	= 0.0753, lb/sec	P_{T3}/P_{T1}	= 1.500
$N/\sqrt{\theta}$	= 51,153 rpm	$\Delta T/T_{OA}$	= 0.2313
η	= 0.876		
P_{T2}/P_{T1}	= 1.579		
$\Delta T/T_{EULER}$	= 0.2289		
Specific Speed	= 47.4 - Defined as $N_S = \frac{N\sqrt{Q_{AVG}}}{H_{ACT}^{3/4}}$		
No. of Blades:	13 full blades 13 splitters	where N = RPM	
Slip Factor	= 0.931	$Q_{AVG} = (Q_1 Q_2)^{1/2}$, ft^3/sec	
P_{o_1}	= 70.8 psia		
T_{o_1}	= 536°F	H_{ACT} = Head, ft.	
N_{PHYS}	= 52,000 rpm		
Diameter Tip	= 2.12 inch		
Inducer Hub	= 0.509 inch		
Inducer Tip	= 0.931 inch		

The values of impeller efficiency, impeller pressure ratio, and Euler work were calculated during the preliminary design analysis (Reference 1).

Design logic. The compressor design is conducted in accordance with the logic shown in Figure 8. Three basic computer codes are used in the process.

The impeller design iteration is started by selecting a meridional hub and shroud surface, with leading and trailing edge radii compatible with the preliminary design analysis, and an assumed blade angle distribution into the impeller geometry program. The output from the geometry program is then input to the compressible flow analysis program along with aerodynamic loss and blockage distributions and a flow solution is obtained. If the blade loadings calculated are unacceptable, either the blade angle distribution or the meridional flowpath is changed and re-entered to the impeller geometry program. This process is then repeated until satisfactory blade loadings are achieved.

The diffuser is then designed and analyzed using the Channel boundary layer analysis program. Vane shapes are generated external to the program and then analyzed. The vane shape is changed until the maximum predicted pressure rise coefficient (CP) is achieved.

Impeller design. -

(1) Aerodynamic assumptions. - Three aerodynamic quantities which must be supplied to the compressible flow analysis program to describe variations of the flow conditions within the impeller are the loss, blockage and deviation angle.

The loss input relates the total pressure to the total temperature at any point in the flow field. it is given by

$$Q = \frac{(P/P_1)^{\frac{\gamma-1}{\gamma}}}{T/T_1}$$

This value was varied linearly with meridional distance from the impeller leading edge, where it was taken to be 1.0, to the impeller exit where its value was compatible with the design impeller efficiency. This efficiency includes the friction, secondary flow, and clearance losses as estimated in the preliminary design analysis.

The aerodynamic blockage, representative of the boundary layer displacement thickness growth, is input to the compressible flow analysis as the ratio

$$\lambda = A_{eff}/A_{geo}$$

The impeller leading edge value was calculated from boundary layer displacement thicknesses which resulted from the inlet hub and shroud velocity distributions. The impeller exit blockage was selected to be consistent with current design and test experience for this magnitude of Reynolds number. A linear distribution with meridional distance was used between these end points.

Due to the small size of this component, the impeller blade fillet radii imposes a blockage not normally accounted for. Therefore, the aerodynamic blockage on the hub streamline was modified to account for this additional blockage.

Deviation of the flow from the blade is required to properly account for the effects of incidence at the impeller leading edge and deviation (slip) at the trailing edge. At the leading edge, the relative fluid angle is faired into the blade meanline angle at a point just inside of the covered portion of the blade. At the trailing edge, the fluid angle is faired, using a parabolic fit, from the estimated starting point of deviation to the final deviation angle at the impeller exit. The final deviation angle is calculated to be consistent with the slip factor used in the preliminary design analysis.

(2) Geometric input. - Blade normal thickness distribution was selected to give the blade sufficient stiffness to prevent deflection by the cutting tool. Blade stresses at maximum operating speed were well below the allowable margin for the selected normal thickness. The number of blades was set by the minimum cutter size which would fit between adjacent blade surfaces in the inducer hub region.

(3) Design details. - The final flowpath from the inlet to the impeller exit station is shown in Figure 9. The solid lines cutting across the impeller flowpath are the compressible flow analysis calculation stations. The dashed line shows the position of the splitter blade leading edge.

The inlet hub and shroud wall velocity distributions are shown in Figure 10. Each profile is seen to have no large diffusion which could cause poor boundary layer conditions entering the impeller.

The final hub blade loading is shown in Figure 11. The splitter vane location was selected to prevent a pressure surface diffusion ratio based on local velocity of below 0.5 from occurring and to allow sufficient blade normal spacing for manufacturing purposes.

The shroud blade loading is given in Figure 12. The leading edge of the splitter was positioned to minimize the peak suction surface velocity. With the exception of a point just inside the inducer, where the suction surface velocity ratio reached a value of 1.124, the maximum suction surface over velocity was held to a ratio of less than 1.1 of the inlet value. This criteria is based on past AiResearch designs which gave good compressor performance.

The final blade and gas angle distributions to the first design are given in Figure 13. The dashed lines show the variation of the gas from the blade direction in the leading and trailing edge regions as discussed in previous section (Aerodynamic Assumptions).

A comparison of the minimum loss incidence angles (Reference 2) at the impeller leading edge, compared to design values, is given in Figure 14. An exact match could not be achieved due to the 608 impeller geometry program limitations. However, the maximum difference of 0.65 degrees is not significant for the level of Mach number in this design.

An axial view of the impeller, with splitters, is shown in Figure 15. The final vector diagrams are given in Figure 16. The exit vector diagrams are calculated inside the impeller blade row; the inlet vector diagrams are outside the blade.

Diffuser Analysis and Design

The design requirement for the diffusion system is to diffuse the flow from an inlet Mach number of 0.502 down to an exit Mach number of 0.025 with all swirl removed. For the large amount of area change required, a two-stage vane island diffuser with deswirl vanes was used in the first design.

The flowpath with a summary of pertinent quantities is shown in Figure 17.

First Vane Row Analysis and Design - Selection of vane number is of primary importance to the diffuser design as it sets the diffuser aspect ratio, depicted in Figure 18. From data on two-dimensional diffusers published by Runstadler (Reference 3), the peak pressure recovery is seen to occur at an approximate aspect ratio value of 1 (Figure 19). For the throat area of this design, a vane count of 23 was selected.

Several restrictions were placed on the first vane row. First, an area distribution to give the maximum diffuser effectiveness (C_p/C_{pi}) was required since the largest efficiency loss will be incurred by this vane row. Second, it was decided to limit the maximum calculated boundary layer shape factor to approximately 2.2 to prevent flow separation from occurring within the vane passage. Current literature (References 4 and 5) indicates turbulent boundary layer separation in channel flow may not occur until the shape factor (displacement thickness/momentum thickness) reaches a value of 3.0.

Design selections were made for vane incidence angle and throat area. A plot of diffuser loss coefficient versus mean-line incidence is shown in Figure 20. This figure is based on test data from a diffuser with similar inlet Mach number magnitude and air angle. The minimum loss incidence is seen to occur at a value of approximately -5 degrees. However, at this value of incidence, the desired value of throat area could not be achieved. From calculations with the channel boundary layer analysis, larger ratios of throat to inlet area gave better pressure recovery. It was therefore decided to base the design selection more heavily upon the channel flow boundary layer analysis. For this reason, the design incidence was -1.4. While this value of incidence angle puts the diffuser on the surge side of the loss characteristic, maximum flow range was not a primary consideration for this compressor.

To maximize the first row effectiveness, area ratios of 2.25, 2.5 and 2.74 were evaluated for a constant value of L/w, of 15. A boundary layer analysis of the initial design, which had parallel end walls, indicated a convergence of the end wall boundary layers for area ratios greater than 2.43. Since there is no proven analytical tool to calculate the boundary layer growth for a fully developed profile under a positive pressure gradient, it was decided to diverge the end walls to accommodate the current design tools. Also, one would expect an improved pressure recovery if the end wall boundary layers have not merged. The total passage height increase from inlet to exit for the first vane row was based on a previous AiResearch 3-dimensional design. A straight line passage height variation with radius was used to provide a reasonable shape for manufacture.

Diffuser vanes with constant and variable thickness were analyzed for the three area ratios. However, during vane development for the 2.5 and 2.74 area ratios, the constant thickness vanes gave a poor area distribution. Hence, the vane thickness was allowed to vary for these two configurations. A comparison of diffuser effectiveness for each area ratio is given in Figure 21. From this comparison, the area ratio of 2.5 was selected for the first vane row. The loss in adiabatic efficiency through this vane row is 0.066 points.

Second Vane Row Analysis and Design - The second vane row was designed to give maximum static pressure rise. Due to the large inlet boundary layer thickness, a full channel boundary layer solution through the vane could not be obtained. Hence, the design was based on experimental data from Johnston and McMillan (Reference 6) for low aspect ratio diffusers with fully developed inlet profiles. Their data shows that the maximum static pressure recovery obtainable for a diffuser with "no substantial stall" occurs at an $L/w_1 = 6$ and an area ratio of 2.4. The "no substantial stall" regime corresponds to geometries which are below the line a-a of Fox and Kline (Reference 7). The "no stall" condition was also verified experimentally by Johnston and McMillan.

A three-dimensional configuration was also used for this design, primarily to improve the local passage aspect ratio. The static pressure recovery used to calculate the exit flow conditions from this diffuser was taken from the Johnston data. No attempt was made to account for distorted inlet conditions caused by the first vane row wakes. However, due to the considerably reduced inlet dynamic head, the possible error in the estimated loss is not expected to be large.

Circumferential spacing of the two vanes rows in shown in Figure 22. The second vane row leading edges were placed midway between the trailing edges of the first vane row exit.

Bend, Deswirl Vane Design - The bend was designed with increasing annular area to mid bend and decreasing area back to the inlet value at the exit. This was done to prevent excessive velocity increase on the hub surface.

The original intent for the deswirl vanes was to remove all the swirl. However, the calculated diffusion factor, a parameter commonly used in axial compressor blading design (Reference 2), was quite large for this amount of turning. By leaving 15 degrees of swirl in the flow, the deswirl vane loss factor was reduced approximately 30 percent. The incidence loss at the cooling fin leading edge was calculated to be negligible.

A complete summary of the efficiency decrements, swirl angles and Mach numbers through the diffuser was presented in Figure 17. The final design calculated efficiency is seen to be 0.005 of an efficiency point below the value estimated in the preliminary design analysis (Reference 1).

Initial Compressor Stage Performance Testing

Compressor test rig. - The test rig utilized for compressor development testing is shown in Drawing 3604021. This rig contained provision for evaluating vaneless diffusers, vaned diffusers without deswirl vanes and finally the complete diffuser system with deswirl vanes.

The rig was driven by an existing laboratory air turbine drive module.

The overall rig design was such that the impeller and shroud hardware was identical with engine hardware. This would allow future use of the rig for evaluation of problem hardware, reverification after extended loop tests or product improvement development tests.

Test results. - The impeller and the two-stage radial diffuser (before assembly) are shown in Figures 23 and 24.

The compressor map of the original Mini-BRU compressor stage is presented in Figure 25. Performance mapping was conducted with Krypton as the working fluid. At design corrected speed and a corrected flow of 0.0753 lbm/sec, the compressor work input is approximately 6 percent higher than the design

objective, whereas the stage efficiency was more than 10 points below the design goal.

In Figures 26 through 34, performance and vector diagram information is presented for the original design at the desired corrected speed. Comparisons with the related design objective values clearly indicate that most of the performance decrement was caused by the diffusion system. Specifically, from Figure 29, it can be seen that the deduced impeller efficiency was within 2.5 points of the design objective at the design corrected flow, and from Figures 30 and 31, the diffusion system minimum loss coefficient is seen to be nearly twice that of the objective value. Since the diffuser minimum loss occurred at a corrected flow which was close to the objective value, a restaggering of the diffuser vane i.e., stage rematch, offers very little gain in efficiency - the major problem is caused by the high level of diffuser losses. Note also from Figure 29 that a higher than desired impeller efficiency was obtained at a corrected flow which was lower than the design objective flow.

Comparisons between impeller Test 1 data presented in Figure 29 through 34 and the corresponding design objectives are summarized in Table IX. High levels of work input and impeller exit Mach number appear to be caused mainly by the higher than expected level of impeller slip factor.

Impeller shroud static pressure distributions at the design corrected speed are shown in Figure 35 for several data scans ranging from choke to surge. Agreement between the shroud static pressure distribution from Test 1 and that predicted by the design program (axisymmetric flow analysis) from Figure 35 is seen to be good for the design corrected flow.

Vaned diffuser static pressure data was obtained along the shroud surface of a passage meanline of the first- and second-stage radial diffusers. Diffuser meanline static pressure distributions at the design corrected speed are shown in Figure 26 for several data scans ranging from choke to surge. A rather large discrepancy between the first-stage diffuser design calculations and the level actually obtained for the design corrected flow can be seen from Figure 36.

TABLE XI. - COMPARISON OF IMPELLER TEST DATA.

ITEM	TEST 1	DESIGN OBJECTIVE	PERCENTAGE DIFFERENCE
$N/\sqrt{\theta}$ (rpm)	51153	51153	0
$W\sqrt{\theta}/\delta$ (lb/sec)	0.0753	0.0753	0
$\Delta T/T$	0.245	0.2313	+5.92
$(P_{02}/P_{01})_{IMP}$	1.60	1.577	+1.46
P_{S2}/P_{01}	1.275	1.286	-0.86
η_{IMP}	0.8415	0.8644	-2.85 (or 2.4 PTS)
SLIP FACTOR	0.977	0.9327	+4.75
β_{2FL} (DEG)	75.5	74.7	+1.07
M_2 (INSIDE BLADE)	0.5314	0.508	+4.41

Prior to charging the test loop with Krypton for performance mapping, argon was used for system and data reduction check-out. This period was also used for investigating the effects of Reynolds number on compressor performance. Figures 37 and 38 show the effects of Reynolds number on compressor stage and impeller performance. These data were taken at 70 percent of the design corrected speed (in argon)* because of a physical speed limitation of the bearings. By varying the loop pressure level, the compressor Reynolds number, characterized by compressor inlet stagnation conditions and impeller exit diameter and tip speed, was varied from 0.61×10^6 to 1.5×10^6. Because of loop pressure limitations, the Reynolds number at which the Mini-BRU compressor was tested in krypton was only 1.35×10^6 compared with the design point value of 4.74×10^6. An increase in performance due to Reynolds number effects can be expected when operating at the actual Mini-BRU engine pressure levels.

During compressor testing, a certain amount of flow leaks down the compressor backface through the carbon face seals (see Drawing 3604021). The magnitude of this flow is difficult to measure. An analytical study was performed to evaluate the effect of backface flow rate and backface clearance on disc friction losses. The result of this study is shown in Figure 39. With a design point compressor horsepower input requirement of 3.72 hp, the disc friction losses can account for up to 2 points in efficiency. This loss is seen to decrease with increasing backface flow rate.

Compressor Stage Redesign

After reviewing the test data the following recovery plan was implemented:

(1) The existing impeller shroud would be recontoured to obtain the highest practical level of impeller efficiency at the design corrected flow without requiring a tooling change. This recontour would take advantage of the higher levels of impeller efficiency which were demonstrated for flows lower than the objective corrected flow.

(2) A new single-stage radial diffuser would be designed to match the flow conditions existing from the recontoured impeller.

*Seventy percent of design corrected speed in argon is equivalent to 101.4 percent of design corrected speed in krypton.

Impeller shroud recontour. -

(1) General. - A review of the data from the test of the original compressor design clearly indicated that the major contributor to the performance decrement was the poor performance of the diffiser. However, as can be seen from Figure 29, the peak impeller efficiency at the design corrected speed, occurs at a flow which is lower than the design corrected flow. Thus, the efficiency of the impeller at the design corrected flow can be improved by a recontour of the impeller shroud which increases its flow capacity.

From Figures 30 and 35, it can be seen that the compressor work input and the impeller exit flow angle for the original impeller were higher than the objective values of the design corrected flow. If a simple shroud recontour is employed to achieve higher impeller efficiencies at the Mini-BRU design flow, even higher work input and impeller exit flow angles result. Thus, a preliminary design study was conducted to determine the optimum way of decreasing the compressor input work level after increasing the impeller flow capacity.

(2) Preliminary design. - A preliminary design tradeoff study was conducted for determining the optimum method of decreasing compressor work input after "high flowing" the impeller. Staying within the framework of utilizing the basic existing impeller design, the two practical procedures available were: (1) decreasing the impeller exit diameter, and (2) decreasing the impeller exit width. Data from Test 1 were used to establish baseline values for impeller performance and slip factor.

Figures 40 and 41 show the effects of simultaneously increasing the impeller flow area by varying amounts and decreasing the impeller exit diameter to reduce the compressor work input to the original design objective value. The major advantage of this method is that the impeller exit width tends to increase with increasing flow area change and, thus, tends toward lower impeller clearance losses. The major disadvantages

of this method includes increases in relative diffusion from impeller inlet to exit and increased (more tangential) impeller exit flow angle. Since the major disprepancy in the performance of the original compressor design was attributable to the diffuser and since the vaned radial diffuser inlet flow angle was already high, further increases in impeller exit flow angle were considered to be very undesirable. Therefore, a reduction in impeller exit diameter was not implemented during this redesign effort.

Increasing the impeller flow area by modifying the shroud streamline in conjunction with decreasing the impeller exit width to obtain the original objective pressure ratio results in an impeller exit width of 0.062 inches. Because of a concern for the axial clearance losses resulting from this low exit width, a study was performed to determine the impact of changes in overall compressor pressure ratio. Figure 42 presents the results of the study and shows that a small increase in compressor pressure ratio has a relatively minor impact on the cycle.

Figures 43, 44 and 45 show the effects of increasing the impeller flow area by the addition of a shroud streamline with (a) no subsequent decrease in impeller exit width and (b) a decrease in impeller exit width to 0.079 in. (the original impeller design value). It can be seen that increasing the impeller flow without decreasing the impeller exit width is not attractive because of the higher relative diffusion required, the higher resultant overall pressure ratio, and especially becuase of the high impeller exit flow angle. All of these objections disappear if the impeller exit width is reduced to 0.079 in. for all values of increased impeller flow. This procedure was selected for the impeller recontour.

(3) Details of impeller shroud recontour. - The impeller performance goal for the redesign effort was selected to match a Test 1 operating point at a corrected flow of 0.06 lb/sec. Thus, the impeller shroud recontour consisted of increasing the impeller flow area by 25.5 percent (to provide, at the Mini-BRU design corrected flow of 0.0753 lb/sec, the impeller efficiency that currently exists for a corrected flow of 0.06 lb/sec).

The impeller exit width was then reduced to its original design value of 0.079 in. The final shroud contour was obtained by blending smoothly from the 125.5 percent streamline at the impeller inlet to the 100 percent streamline at the impeller tip.

Figures 46 and 47 show the final impeller and inlet meridional flowpath. These figures show calculation station identification numbers and a comparison of the new and the old shroud contours.

Blade loadings resulting from this modification were checked. Relative velocity loading diagrams for the shroud and hub streamlines are shown in Figures 48 and 49. Also shown in these figures are comparisons of these loading distributions with those obtained from a simulation of Test 1 data at a corrected flow of 0.06 lb/sec. This comparison indicates that no problems should be expected due to this impeller shroud recontour.

Figure 50 shows incidence distributions obtained from the axisymmetric flow analysis for the recontoured impeller operating at the design corrected flow and for the original impeller operating at a corrected flow of 0.06 lb/sec. These distributions are generally within a degree of each other.

The vector diagram information obtained from Test 1 data analysis and from the impeller shroud recontour analysis was used in the diffuser redesign effort.

Diffuser Redesign. -

(1) General. - From the full stage test of the original compressor design (Test 1), very high diffuser loss levels were observed even though the diffuser was well matched to the impeller (see Figures 30 and 31). The requirement for a diffuser redesign was clearly indicated.

During the design and testing of the Mini-BRU compressor, a parallel effort was being conducted at AiResearch to develop a compressor for a 1.5 to 3 kW generator set for the U.S. Army Mobility Equipment Research and Development Center. This compressor which was slightly larger than the Mini-BRU compressor demonstrated excellent performance. Reference 9 presents details of the design, development, and testing of the MERDC 1.5 to 3 kW compressor.

Where possible, the diffuser design philosophy of the MERDC 1.5 to 3 kW compressor was applied to the Mini-BRU compressor diffuser redesign. Figures 51 and 52 show the geometries of the 1.5 to 3 kW diffuser and the original Mini-BRU cascade diffuser. It appears that the relatively high diffuser passage turning downstream of the throat for the first-stage of the Mini-BRU compressor, though it was in the direction of low absolute turning, caused high diffuser losses.

The stage compressor map for the 1.5 to 3 kW compressor (shown in Figure 53) shows relatively high efficiency levels when compared with those obtained in Figure 25 for the Mini-BRU compressor.

One of the main differences between the Mini-BRU and the 1.5 to 3 kW diffusers is the different level of diffuser inlet Mach number (0.485 for Mini-BRU and 0.812 for 1.5 to 3 kW diffuser). This appears to be a favorable difference because the Mini-BRU diffuser has a considerably lower diffuser inlet Mach number than does the 1.5 to 3 kW diffuser, which should cause its performance to be relatively insensitive to inlet flow angle. This insensitivity to diffuser inlet flow is demonstrated in Figure 31 where the Test 1 diffuser losses are seen to be very close to the minimum loss over a rather broad range.

(2) Radial diffuser redesign. - The principal design tools used for the radial diffuser design were a boundary layer analysis based on Reference 9 and the Katsanis blade-to-blade analysis based on Reference 10.

A summary of the final redesigned diffuser and estimated performance is shown in Figure 54.

A design summary for the final radial diffuser redesign is shown in Table XI in addition to a comparison to the corresponding design requirements and geometric parameters for the 1.5 to 3 kW radial diffuser. Most of the parameters for the two designs exhibit close agreement. Besides the lower inlet Mach number requirement for the Mini-BRU diffuser, other significant differences include the larger area ratio requirement and the lower value of negative incidence of the Mini-BRU diffuser. This lower value of negative incidence was determined from Test 1 data (Figures 30 and 31). The Mini-BRU diffuser design seemingly has a higher throat-to-capture area ratio than for the 1.5 to 3 kW diffuser, but when compressibility effects accounting for the different inlet Mach number levels are considered, the agreement is seen to be close. The final radial diffuser design geometry is shown in Figure 55.

Diffuser area distributions are shown in Figure 56 for the final design configuration. The corresponding pressure rise recovery and shape factor distribution are shown in Figures 57 and 58. Diffuser vane loading diagrams obtained from a Katsanis blade-to-blade analysis are shown in Figure 59 for the final design. The effective Katsanis solutions were chosen to account for the boundary layer blockage predicted by the boundary program. This loading distribution does not indicate any problems.

(3) Elbow design. - The elbow for the redesigned radial vaned diffuser is shown in Figure 60 and its area distribution is shown in Figure 61. This design is consistent with that of a minimum loss elbow.

(4) Deswirl vane design. - Constant thickness deswirl vanes were designed by the method described in Chapter 7 of Reference 4. Figure 62 shows the final deswirl vane design as well as an aerodynamic and a geometric design summary. Inlet and exit vector triangles are shown in Figure 63.

TABLE XI. - DIFFUSER COMPARISON

ITEM	1.5/3 kW	MINI-BRU
B_2 (IN.)	0.077	0.079
VANELESS R_3/R_2	1.046	1.05
DIFFUSER L.E. RAD, R_3 (IN.)	1.320	1.113
NUMBER OF DIFFUSER VANES	24	17
AREA RATIO, R_4/R_3	3.0	4.2
LENGTH TO INLET WIDTH RATIO	16.7	17.5
ASPECT RATIO $(\frac{\text{b-WIDTH}}{\text{INLET WIDTH}})$	0.92	0.93
VANE DIFFUSER L.E. THICKNESS (IN.)	0.008	0.008
VANE DIFFUSER L.E. MEANLINE ANGLE (DEG)	80.0	79.26
VANE DIFFUSER THROAT/INLET WIDTH (MINI-BRU EQUIVALENT INCLUDING COMPRESSIBILITY)	1.099 (1.18)	1.21
VANE DIFFUSER EXIT RADIUS (IN.)	2.06	1.92
VANE DIFFUSER T.E. NORMAL THICKNESS (IN.)	0.150	0.204
IMPELLER EXIT MACH NO., M_2	0.892	0.526
IMPELLER EXIT FLOW ANGLE, β_2 (DEG)	75.3	78.24
VANE DIFFUSER INCIDENCE $(\beta_{2FL} - \beta_{3VANE})$ (DEG)	-4.7	-1.02
VANE DIFFUSER INLET MACH NO.	0.812	0.485
VANE DIFFUSER AVG. EXIT MACH NO. (INSIDE VANE)	0.191	0.105
$\bar{\omega}$ - IMPELLER EXIT TO VANE DIFFUSER EXIT (INSIDE VANE)	0.215	0.216

Compressor Stage Retest

During September, 1976, the following tests were conducted:

(1) Vaneless diffuser mapping (impeller only) of the recontoured impeller.

(2) Stage mapping at four corrected speeds with nominal axial clearance setting of the recontoured impeller, the redesigned single-stage radial diffuser and the redesigned axial deswirl vanes. This data was obtained with an inlet pressure of 25 psia (compared to the design level of 70.8 psia) in order to minimize the consumption of krypton.

(3) Design speed stage mapping with axial clearance values larger and smaller than nominal.

(4) Design speed stage mapping with nominal axial clearance and with the compressor inlet pressure increased to 45 psia in order to determine the effects of Reynolds number on compressor performace.

The results of these tests indicate that the program compressor performance goals were exceeded:

(1) Impeller efficiency at the design corrected flow increased by more than four points as a result of the impeller shroud recontour.

(2) Stage efficiency at the design corrected speed indicated a peak very near the design corrected flow for each of the stage tests that were conducted.

(3) With nominal axial clearance and with an inlet pressure of 25 psia, the peak efficiency was approximately 0.756 (compared with the design objective efficiency of 0.758).

(4) Decreasing the axial clearance from 0.0059 to 0.0048 in. increased the peak efficiency to 0.762.

(5) With a nominal axial clearance setting, increasing the compressor inlet pressure from 25 to 45 psia, which corresponds to a Reynolds number increase from approximately 1.6×10^6 to 2.9×10^6,

results in a peak efficiency increase to 0.770. (The Reynolds number corresponding to the design point is approximately 4.4×10^6).

Test 2 results - recontoured impeller, vaneless diffuser test. - The vaneless diffuser compressor map of the recontoured impeller is shown in Figure 64. A comparison of Figure 64 with Figure 32 shows that at the design corrected speed and flow, the total-to-total efficiency of the recontoured impeller increased by more than four points over that of the original design. This increase was more than a point higher than expected.

Test 3 results - recontoured impeller, redesigned diffuser stage test.

Nominal axial clearance, inlet pressure of 25 psia. - The performance of the stage consisting of the recontoured impeller, the redesigned radial diffuser (Figure 65), and the redesigned axial deswirl vanes is shown in Figure 66. These data were taken with a nominal axial clearance setting and with an inlet pressure of 25 psia. Comparison of the stage performance to the corresponding objective values at the design corrected speed and flow shows excellent agreement.

In Figures 67 through 74, performance and vector diagram information is presented for the design corrected speed. Comparison to the related design objective values generally shows close agreement. Significant differences are shown in Figures 70 and 71 where the impeller total-to-total efficiency is seen to be more than a point higher than the objective and the diffusion system's loss coefficient is seen to be higher than expected. From Figure 69, it can be seen that these differences tend to cancel each other so that the overall stage efficiency is very close to the objective value. Also from Figure 69, it can be seen that peak efficiency occurs very close to the design corrected flow.

Impeller shroud static pressure distributions at the design corrected speed are shown in Figure 75 for several data scans ranging from choke to surge. The shroud static pressure distribution at the design corrected flow is seen to deviate from that predicted by an axisymmetric flow analysis downstream of the splitter vane leading edge. This difference was larger than was demonstrated for the original impeller (see Figure 35), but the qualitative agreement is good.

Axial clearance data. - The effect of axial clearance on compressor performance settings at the design corrected speed was investigated in Test 3A. The inlet pressure was held at 25 psia and the axial clearance increased and decreased from the nominal setting.

The stage compressor maps for both the increased and the decreased axial clearance levels are shown in Figure 76 Performance data for the three clearance values are compared in Figures 77, 78 and 79 for the overall performance, impeller performance, and diffuser performance respectively. This compressor is seen to be relatively insensitive to axial clearance, and, as expected, the observed performance changes are attributed mainly to the impeller.

Reynolds number data. - The effect of Reynolds number on compressor performance at the design corrected speed was investigated in Test 3B. The axial clearance was set very close to the nominal value of 0.006 in. and the compressor inlet pressure level was increased to 45 psia. As a result of this inlet pressure change, the Reynolds number (characterized by the compressor inlet stagnation conditions, impeller exit diameter and wheel tip speed) increased from 1.6×10^6 to 2.9×10^6 (the Reynolds number corresponding to the engine design point is approximately 4.4×10^6).

The stage compressor map for the increased Reynolds number is shown in Figure 80. Performance data for the two Reynolds number levels are compared in Figures 81, 82 and 83 for the overall performance, impeller performance, and the diffuser performance, respectively. The effect of Reynolds number is seen to be significant over the range that was investigated. From Figures 80 and 81, it can be seen that the design efficiency of 0.758 was exceeded by over a point. From Figures 82 and 83, it can be seen that this increase in Reynolds number caused an increase in both impeller and diffuser performance. Note that at this higher Reynolds number level (but lower than the design Reynolds number), both the impeller and the diffuser exceeded the design performance goals.

One relationship that has been used to correlate loss with Reynolds number for compressors is:

$$\frac{1 - \eta}{1 - \eta_{ref}} = \left[\frac{Re_{ref}}{Re}\right]^n$$

An exponent of n = 0.1 was found to closely approximate the Reynolds number of Reference 6 over a range of Reynolds numbers from 0.34×10^6 to 3.03×10^6 (see Figure 9 of Reference 12). The current Reynolds number data also exhibited this trend between the two Reynolds numbers considered with an exponent of

0.099. If this exponent were used to extrapolate the data to the design Reynolds number of 4.4×10^6, the compressor efficiency would be 0.779, or 2.1 points higher than the design goal. Even if a value of n = 0.06, the value presented in Reference 6 for the higher Reynolds number data were used for the data extrapolation, the compressor efficiency at the design conditions would be 0.776, or 1.8 points higher than the design goal. Obviously, an exact level of compressor efficiency cannot be precisely determined without actually operating at design conditions.

Conclusions

The Mini-BRU compressor program has yielded several results which can be utilized for future applications requiring small compressors with high efficiency. These results indicate:

(1) Extremely small compressor stages can be efficient. The Mini-BRU compressor stage (with the 2.12 in. diameter impeller) demonstrated a level of efficiency (in excess of 0.77) which was heretofore considered unattainable for such a small compressor.

(2) Vaned diffusers with passage widths of the same order of magnitude as the boundary layer can be efficient. Since vaneless diffusers are relatively inefficient, low loss vaned diffusers are required to provide a usable exit Mach number.

(3) Small, high area ratio single stage radial diffusers can be efficient. The diffuser area ratio of 4.2 of the current design is one of the highest in the recent history of AiResearch. The demonstrated high performance provides an alternative to multistage diffusers for applications requiring high diffusion.

(4) Reynolds numbers effects for the Mini-BRU compressor closely resemble the effects reported in Reference 6. Between Reynolds numbers of 1.6×10^6 and 2.9×10^6, the relation

$$\frac{1 - \eta}{1 - \eta_{ref}} = \left[\frac{Re_{ref}}{Re}\right]^n$$

acceptably correlates the observed data if $n \approx 0.1$.

TURBINE DEVELOPMENT

Turbine Stage Design

Introduction. - This section describes the design procedures that were used to establish the basic configuration of a radial turbine for the Mini-BRU. Working fluid for the turbine is a helium/xenon mixture having a molecular weight of 83.8. Design speed is nominally 52,000 rpm, and the maximum weight flow requirement is set at 0.357 lb/sec.

Radial turbine performance was examined thoroughly, and Mini-BRU performance was predicted based on previous NASA test experience with the BRU turbine. An optimization study was conducted to establish the design inlet gas angle to the turbine rotor. The rotor was then designed using standard AiResearch design practice. Close coordination between the aerodynamic and stress requirements was necessary for this design. The stator vanes were designed from two-dimensional cascade sections which are transformed into the radial plane. The transformed vane shape was analyzed aerodynamically, and blade loadings were compared with previous designs.

The final phase of the radial turbine design program included the examination of previous diffuser design experience and the design of an annular diffuser configuration. The design incorporated a region for mixing prior to any diffusion as an aid to the overall diffusion process. Strong evidence exists indicating that mixing prior to diffusion is necessary for good turbine diffuser performance.

Literature review. - Extensive testing of Brayton cycle power system components by the NASA-Lewis Research Center has produced an abundance of experimental data concerned with radial turbines (see References 13-25). This information has been factored into the design of the radial turbine for the Mini-BRU space power system where possible. An excellent summary article discussing pertinent results and conclusions from the NASA investigations is presented in Reference 21. Specific applications of this information in the design effort will be noted by references in the following text.

Stage performance. - Design specific speed, N_S*, for the Mini-BRU turbine is 44.6. Experience in this low specific speed range is limited throughout the industry. NASA has performed limited testing in this range utilizing the BRU turbine with modified stators and a rotor exducer extension. This effort also

*See Figure 84 for definition of specific speed.

include both basic rotor performance and cutback rotor performance over a range of stator settings. The latter configuration was employed to investigate performance at high specific speeds.

The composite performance curve from these tests is shown in Figure 84. Note that at the design specific speed of the Mini-BRU turbine, the measured total efficiency is approximately 87.5 percent. The test configuration that resulted in this performance level had a stator closed to 42 percent of the design throat area and an exducer extension. Obviously these modifications to the basic turbine, which were designed for much higher specific speeds, cannot represent optimum turbine performance in the low specific speed range. However, lacking additional information at low specific speeds, the 87.5 percent efficiency level was accepted as representing reasonably good stage performance at the Mini-BRU turbine design speed. This value then served as the base for estimating performance of the new turbine under consideration herein.

A performance summary is presented in Table XII which includes a listing of the various effects considered to reconcile with measured efficiency on the BRU turbine. In order to adequately compare performance between the two turbines, it is first necessary to establish a base efficiency level for the BRU turbine. This requires specific calculated losses to be factored out where obvious influences of turbine size and operating conditions are evident. In the case of the BRU turbine, performance corrections are made for operation at a non-optimum blade-jet speed ratio, disk friction losses, and clearance effects.

Eliminating known losses from the BRU turbine data results in a base efficiency of 89.9 percent. This corresponds to various unseparable losses, such as rotor and stator friction, blade loading, secondary flow losses, plus any losses associated with the inlet scroll. While these losses are influenced by viscous effects throughout the flowpath, any relative change can be approximated by a Reynold's number correction to the predicted performance based on a reference Reynold's number for the measured data. The correction was developed as a result of a series of radial turbine tests conducted by NASA-Lewis. The empirical formula for making this correction is shown below:

$$\frac{1-\eta_T}{1-\eta_{T\ BRU}} = 0.4 + 0.6\left[\frac{Re}{Re_{BRU}}\right]^{-1/5}$$

After correcting the Mini-BRU turbine base performance for viscous effects, additional corrections were applied for blade

TABLE XII. - TURBINE PERFORMANCE SUMMARY

Description	BRU η_{T-T}	BRU $\Delta\eta$	MINI-BRU η_{T-T}	MINI-BRU $\Delta\eta$
BASE EFFICIENCY, η_{BASE}	0.8990		0.8990	
REYNOLD'S NO. EFFECTS		0.0		-0.020
η_{CORR} (REYNOLD'S NO.)	0.8990		0.8790	
CLEARANCE LOSSES		-0.0143		-0.0333
η_{CORR} (RE. NO. + CLEARANCE)	0.8847		0.8457	
DISK FRICTION LOSSES		-0.0074		-0.0106
η_{CORR} (RE. NO. + CLEAR. + D.F.)	0.8773		0.8351	
SPEED RATIO EFFECTS		-0.0023		-0.0012
η_{T-T} (TURBINE EXIT)	0.8750		0.8339	
DIFFUSER LOSS				-0.0055
η_0 OVERALL STAGE EFF.			0.8284	

A35538

clearance, disk friction, and non-optimum, blade-jet speed ratio to arrive at a design turbine efficiency. Reiterating a point made earlier, the loss models employed here are identical to those used to establish base performance for the BRU unit.

Because of the small size of the Mini-BRU turbine, clearance effects on performance are quite large. The influence of clearance is readily apparent when referring to Figure 85. This is a carpet plot illustrating the influence of inducer and exducer clearances on overall stage efficiency. From mechanical considerations, design clearances for the inducer and exducer sections are both set at 0.008 in. Holding design clearance will be essential for maintaining good performance. When viewed on the basis of an absolute clearance rather than clearance ratios (absolute clearance/passage width), the importance of holding both inducer and exducer clearances is quite evident as illustrated on Figure 85.

One additional correction must be considered to arrive at a stage efficiency for the Mini-BRU turbine. This correction was applied to account for losses in the exhaust diffuser for the proposed configuration. With diffuser losses accounted for, the predicted stage efficiency of the Mini-BRU turbine was 82.8 percent. This is 0.4 percent lower than the originally estimated performance (83.2 percent).

Preliminary turbine design. - Preliminary design of the radial turbine was accomplished by means of a computer program which requires the following input variables:

(1) Wheel rotating speed

(2) Gas properties

(3) Inlet total pressure and temperature

(4) Weight flow

(5) Hub radius and exit Mach number

(6) Diffuser static pressure rise coefficient

(7) Design pressure ratio

(8) Rotor-shroud clearance

(9) Absolute gas angle at the rotor inlet

The program has provision for determining a base efficiency for the turbine through an iteration on specific speed. A curve fit of base efficiency against specific speed is internal to the

program. However, this part of the program does not provide for a Reynold's number correction to the base efficiency. Therefore, base efficiency was input to the program as that efficiency after the Reynold's number correction as shown on Table XII.

The program computes losses corresponding to clearance effects, disk friction, and blade-jet speed ratio. In essence, a trade-off is made between the latter two loss terms to arrive at the optimum tip radius for a specified inlet gas angle. The basic computer program has no provision for internal optimization of the inlet gas angle. In fact, the program indicates that as the gas angle is increased, turbine performance improves due to a clearance loss reduction. This reduction is a result of the increased blade width for the inducer section which effectively reduces the clearance width ratio and thereby the clearance loss penalty. Since the program could not handle the optimization of the stator gas angle, an empirical method was devised to perform this task.

The increased "b" width at the turbine inlet for higher inlet gas angles, also influences inlet stator losses. While greater turning increases the blade profile loss, the passage aspect ratio improves resulting in an overall decrease in stator loss with higher inlet gas angles. The method used to determine relative stator performance differences, as influenced by inlet gas angle, is similar to the technique described in Reference 26.

Axial turbine experience has shown that large blade blockages at the trailing edge of an upstream stator can seriously impair rotor performance. AiResearch experience along these lines has shown that as long as the trailing edge blockage for the stators is less than ten percent of the passage area, stator losses are readily predicted by analytical methods. However, above ten percent blockage at the stator trailing edge, the performance loss for an axial stage increases significantly over that predicted analytically. Existing test data for stators with large blockages has been empirically curve fit to predict stage losses for those cases where blockage values exceed ten percent. This same data was applied to determine an optimum inlet gas angle for the Mini-BRU radial turbine under the assumption that the relative effect on performance would be the same as experienced in an axial turbine. The results of the inlet gas angle optimization are shown on Figure 86. This shows an efficiency change as a function of stator exit angle for three different values of trailing edge thicknesses. Note that the blade normal thickness, employed in this comparison, translates into larger blade blockages as the stator exit angle increases. This produces a performance peak at lower stator exit angles as the trailing edge thickness is increased. This comparison is made for 17 stator blades which appears to be the minimum necessary for satisfactory turning of the flow to the desired inlet gas angles.

As evident on Figure 86, the thinner stator exit thickness values yield higher performance. The Applied Mechanics Group was consulted concerning (1) what trailing edge thickness would be required to avoid thermal stress cracking during transient operation and (2) structural life under normal operating conditions. The analysis concluded that a 0.015 inch normal thickness for the stator trailing edge was a minimum requirement for the Mini-BRU operating conditions. Optimum stator exit angle for a 0.015 inch trailing edge thickness is approximately 76 to 77 degrees. However, performance changes with stator exit angle are quite small between 75 to 78 degrees. The higher angle, 78 degrees, was selected for the final configuration as this will result in higher rotor reaction. Increased rotor reaction should have a beneficial effect on rotor performance. However, the precise relationship between rotor reaction and stage performance is not established.

Vector diagram. - Vector triangles for the turbine rotor as determined by the preliminary design program are presented on Figure 87. The results of the preliminary design program are then used to start the detailed design of the turbine rotor.

Turbine rotor design. - Detailed design of the turbine rotor follows the design logic outlined on Figure 88. Initially a meridional flow path is assumed based on previous design experience. The flow path is fit to a supercircle curve and radius, axial length, curvature and wall slopes obtained for input to the blade thickness program. The blade angle variation with axial length and for a fixed radius is then assumed from past experience. Radial variations of blade angle for a specific length are obtained from the following relationship:

$$\left(\frac{\text{Tan } \beta}{R}\right)_z = \text{const}$$

An initial estimate of the blade thickness requirements for four axial stations along the flow path is supplied by the Applied Mechanics Group. This information is then input to the blade thickness program where the necessary blade descriptive properties are interpolated for several stations within the flow field of interest. Output includes blade thickness, blade angle, and blade curvatures for input to the streamline curvature, flow analysis program.

The flow program requires that loss distribution as a function of meridional distance be specified as an input. In this program, losses are input as a ratio of the entropy function, Ω, to the corresponding value along the same streamline at the preceding station. The entropy function is defined as follows:

$$Q = e^{-s/C_P} = \left(P/Poi\right)^{\frac{\gamma-1}{\gamma}} \Big/ \left(T/Toi\right)$$

In this expression, P and T are pressure and temperature along a streamline and may either be static values, absolute stagnation values or relative stagnation values as long as a consistency is maintained.

The subscripted pressure and temperature refer to any convenient state or zero entropy level (i.e., inlet stagnation conditions). Initially, the loss distribution is assumed to vary linearly from inlet to exit stations within the turbine rotor with no streamline variation included. Later iterations of the flow field conditions included empirical loss distributions in the meridional direction as well as across streamlines.

Output of the flow solution includes two parameters or interest to the designer. First, the desired overall turbine work must be satisfied. Several iterations are normally required to meet this criteria since both the total turning and the overall loss assumptions influence the result. Once the overall work has been satisfied, the blade loadings in terms of suction and examined along each streamline. Previous experience is used to determine what parameters must be changed to obtain the desired blade loadings. Meridional flow path, overall turning, and the general shape of the blade angle variation with length may be altered to improve the blade loadings.

Once the work and blade loading criteria are satisfied, a complete stress analysis is run on the turbine rotor. If there are any stress problems, the assumed blade thicknesses are changed and the design loop reentered. After all stress considerations have been satisfied, the final tooling layouts are drawn by a flat bed plotter from coordinates obtained from the blade thickness program.

The final meridional flowpath through the turbine is shown on Figure 89. Ten full blades and ten splitters are employed in the turbine rotor. Note that the rotor tip radius (1.429 inches) for the final configuration is slightly larger than the corresponding preliminary design value (1.410 inches). In performing the detailed design of the rotor, clearance effects are accounted for external to the flow solution by adding a work equivalent to the clearance loss term. The higher effective work output may be accomplished in either of two ways. One method is to increase the overall turning required within the rotor by going to higher (more tangential) exit blade angles. The second means for increasing the effective work term is to go to a larger inlet tip radius. The

latter method was selected for this design because the exit blade angles were already sufficiently high such that machining in the exducer blade root region is difficult.

The final blade angle distribution as a function of axial distance is shown on Figure 90. Note that this curve applies to one specific radius (R = 0.842 inch). Determination of the radial variations in blade angle for a given length is described earlier in this report. The general shape of the blade angle variation with length is characteristic of previous AiResearch design experience in radial turbines.

In the streamline curvature solution to the internal flow field a total of 15 calculation stations were employed within the rotor. The alignment of these stations along the meridional flowpath is shown on Figure 91. Each station is made up of a straight line element which cuts across the flowpath from hub to shroud.

In the initial design of the turbine rotor, the assumption was made that no streamline variation in losses existed. With a constant loss at the rotor exit, the assumed loss distribution for each station line is shown on Figure 92. The shape of the loss curve was intuitively derived based on the premise that blade-fluid incidence results in a steep gradient for the inducer section, and boundary layer build-up within the rotor influences the loss gradient for the exducer. After several iterations to arrive at an aerodynamically acceptable flow solution, an empirically derived loss distribution was employed to perform the final flow calculations.

Test results from radial turbine experimental programs have shown a definite trend in loss variation in the radial direction at the turbine exit. These results indicate a region of higher losses exists near the shroud. An explanation for this effect is that the boundary layers along the internal surfaces of the rotor will migrate outward due to centrifugal forces in the rotating flow field. Design pressure ratio across the turbine seems to have an influence on the degree of distortion in the loss profile at the rotor exit as shown on Figure 93. The higher pressure ratio data from an AiResearch turbine has a much greater variation in losses at the exit than the lower pressure ratio data from the BRU turbine. Since the Mini-BRU design will operate at a lower pressure ratio level than the BRU turbine, the exit loss variation is expected to be even less than the BRU has demonstrated. As a result, the loss variation shown on Figure 94 was empirically derived for the purpose of improving the detailed design calculations.

With the loss variation presented on Figure 94, each streamline was assumed to exhibit a distinct overall loss

characteristic. Employing the general shape of the loss distribution curve through the rotor (Figure 92) while matching the overall loss variation at the exit permitted adequate representation of the rotor losses to be accomplished. When this was incorporated into the detailed flow solution, the vector triangles shown on Figure 95 resulted. The conditions presented on Figure 95 are outside the blade row or just upstream of the rotor inlet and immediately downstream of the exducer section. Note that the exit flow is underturned in the shroud region and overturned at the hub. This is characteristic of most radial turbines designed for zero swirl and was the case of the BRU turbine at design test conditions. To avoid swirl in the exit flow, it would be necessary to depart from pure radial blading by incorporating lean in the blade. However, the degree of swirl computed for the Mini-BRU turbine represents an insignificant loss in terms of overall energy remaining in the turbine exhaust stream is approximately 1.8 percent of the input energy while the integral average energy of the swirl component represents only 2.7 percent of the exhaust value. Thus the energy loss due to swirl is less than 0.05 percent of the input kinetic energy for the turbine.

The design blade loading curves in terms of surface velocities versus meridional distance are presented on Figures 96, 97, and 98 for the shroud, mean, and hub streamlines respectively. These loadings are typical of recent AiResearch design experience with radial turbines where good performance was obtained in subsequent test programs.

The foregoing discussion summarizes the design of the turbine rotor for the Mini-BRU. A front view of the turbine rotor is presented on Figure 99. All leading and trailing edges for the blades should be rounded to an elliptical shape for smooth entry and discharge conditions.

Axial thrust. - The remaining parameter investigated in connection with the turbine rotor was the axial thrust during steady-state operation. Axial thrust for the rotor is comprised of:

(1) A backface pressure force

(2) The integrated static pressure-area terms along the shroud

(3) A momentum and static pressure force at the rotor exit

(4) A static pressure force for the downstream hub section

A separate computer program is employed to compute the backface pressure force. This program includes the effects of cooling flow and wall-wheel spacing on the pressure profile across the backface. The various thrust terms and the net axial thrust for the Mini-BRU turbine without scallops is presented in Table XIII.

TABLE XIII. - AXIAL THRUST CALCULATIONS

1.	Integrated Shroud Pressure, Area	340.7 LB_f
2.	Rotor Exit Momentum + Pressure, area	67.9 LB_f
3.	Exit Hub Pressure, Area	55.6 LB_f
4.	Integrated Backface Pressure, Area	-460.0 LB_f
	Net Axial Thrust (Forward)	4.2 LB_f

As is evident from the above tabulation, the net thrust is the difference between two large opposing forces. This makes the significance of the resultant somewhat doubtful, but testing will provide a means for a more precise determination of this parameter.

Axial thrust calculations for the compressor have indicated it will exert a net thrust of 33 pounds in the aft direction. Combined thrust for the turbine and compressor is then 29 pounds in the aft direction. Since this is a larger thrust than desirable for this application, because of the associated thrust bearing loss, turbine rotor scalloping was investigated as a means for alleviating the problem. Several scallop depths were examined and the corresponding effects on the net thrust are shown on Figure 100. Note that it is possible to null out the net thrust with a scallop of a reasonably shallow depth. However, as indicated above, precise values of thrust can only be determined by testing, and it may be necessary to redesign the scallops after experimental evaluation of axial thrust.

The effects of scalloping on radial turbine performance were examined experimentally by Hiett and Johnston (Reference 27). The results indicate that turbine efficiency is not affected by scalloping as long as the scallop does not extend below the shroud diameter of the exducer section. Each of four configurations evaluated had special back-plates manufactured to match backface alterations in the turbine wheel thereby minimizing clearance problems.

AiResearch has experimentally investigated the effects of scalloping on radial turbine performance as well as the effects of backface clearance on scalloped wheel performance. The results of this investigation are presented, on Figure 101, in terms of design point efficiency change versus backface clearance ratio. Note that the smallest clearance tested resulted in identical performance to the unscalloped wheel (also tested), and that the loss is essentially linear with clearance at higher clearance ratios. A range of possible clearances for the Mini-BRU turbine have been included on Figure 101, since a design value cannot be selected without extensive thermal analysis of the surrounding components. Once the thermal growth of the confining wall has been established for scalloped wheel operating conditions, the minimum design clearance will be determined. With this information, the overall effect of scalloping on rotor performance may be determined, and an assessment can be made as to the utility of scalloping for reducing the axial thrust.

Inlet stator design. - Optimum spacing between the stator exit and the rotor inlet was experimentally evaluated in an investigation reported in Reference 28. This investigation, conducted at Keio University in Tokyo, included tests on the same rotor with four sets of inlet stators where the gap distance (radially) varied from 3 to 15 millimeters. Correlation of the test data from Keio University was in terms of adiabatic efficiency versus spiral path length (S) divided by passage width (b). An optimum S/b of 2.0 was determined on the basis of the peak efficiency comparison. Since the radial gap is simply the spiral path length times the cosine of the mean flow angle, the optimum gap spacing was determined to be 0.054 inches. This establishes 1.483 inches as the radius to the trailing edge of the inlet stators.

Many blade shapes can be generated to satisfy a given vector triangle. Design logic for arriving at the final stator configuration is outlined on Figure 102. Note that again close coordination between the stress analyst and aerodynamicist is necessary to define a blade shape that best meets the requirements of the turbine stage.

Optimum chord to spacing ratio is obtained from Zweifel's loading coefficient (Reference 29) for airfoils in a cascade configuration. A value of 0.7 is assigned to the loading coefficient for optimum conditions as specified in the following expression:

$$\psi = 2 \left(\frac{S}{C_X}\right) \frac{\text{Cos } \beta_2 \text{ Sin } (\beta_1 + \beta_2)}{\text{Cos } \beta_1}$$

where: ψ = Zweifel loading coefficient

S = Spacing

C_X = Axial chord

β_1 = Inlet gas angle

β_2 = Exit gas angle

AiResearch practice is to use prime numbers in selecting the number of blades for the nozzle section. Prime numbers are employed to minimize nozzle-rotor interferences at all but the fundamental frequency of the nozzle blades. Seventeen blades were selected for this design although both 19 and 13 blade configurations were examined. A minimum normal thickness of 0.015 inches for the trailing edge blockage was greater than ten percent of the available flow area. As previously mentioned, past experience has shown the nozzle losses to be excessively high for blade blockages above ten percent. Examination of the 13 blade design indicated that the uncovered portion of the blade was quite extensive. This can result in poor guidance for the exit flow with some penalty to the work input to the rotor. The seventeen vane configuration has less uncovered blade section while maintaining exit blade blockage within the design criteria.

The two-dimensional blade profiles are developed by fitting an involute curve to the suction surface and specifying channel width variations to yield the pressure surface. Variations in involute curvature and channel width distributions will influence the blade loading, and changes are introduced until the loadings are satisfactory. The suction surface turning downstream of the throat is limited to six degrees or less. Flow conditions through the cascade section are obtained by assuming free vortex potential flow in the curved regions and uniform potential flow in any straight sections. The corresponding velocity distribution along each surface are used to calculate boundary layer properties (displacement and momentum thicknesses for the suction and pressure surfaces). These are employed in the computation of downstream flow conditions after mixing, using the method described in Reference 30.

The plane sections are transformed to an equivalent radial plane through the use of an appropriate conformal transformation. Conformal transformations provide a one-on-one mapping of a given region from one complex plane to another such that the detailed shape of infinitesimal area elements is invariant. However, this does not imply that finite area elements are unchanged. Conformal transformations to the radial plane

result in a small increase in the geometric throat dimension. The program is therefore set up to modify the transformed profile of the suction surface to maintain the desired throat dimension.

Outputs from the radial transformation program include computer plots of the stator cross section and the mean angle distribution for the blade. Figure 103 shows the stator cross section for all 17 blades for the design configuration. A plot of the angle change with radius for a mean line through the blade is presented on Figure 104.

A further check of the loading distribution for the inlet stator is made with a finite difference program which computes blade-to-blade flow conditions for the transformed blade profile. This program was developed by T. Matsanis and is described in Reference 31. The computed loading distribution for the inlet stators is shown on Figure 105. Again the loading is reported as a function of wall velocity versus path length and the resulting loading is quite satisfactory for this inlet stator application.

Diffuser design. -References 24 and 20 contain examples of problems with annular diffusers when operating downstream of a radial turbine. Reference 32 also discusses the problem and attempts to evaluate the mechanisms which are responsible for low diffuser performance. It is the assessment of the latter article that flow maldistribution and exit swirl downstream of the turbine are primarily responsible for the observed performance characteristics. It is suggested that a constant area mixing region might be beneficial toward increasing diffuser effectiveness.

In the NASA work reported in Reference 24 conical diffuser performance is compared with two diffusers designed for a constant static pressure rise with constant lengths. All diffusers were tested behind the same turbine under identical operating conditions. The constant pressure rise diffusers had the same overall area ratio as the conical diffuser with a minor increase in length. Diffuser performance was determined from survey data (static pressure, total pressure, total temperature and flow angle) at the diffuser inlet and exit station. The conical diffuser had a diffuser effectiveness of 0.4 at design conditions. Effectiveness for the two constant pressure rise configurations ran between 0.6 and 0.65. The net result was an increase in total efficiency for the stage of approximately one percent, attributable to the diffuser configuration.

A method for designing and predicting performance for annular diffusers is presented in Reference 34. A technique

employed to describe the influence of inlet boundary layer thickness on pressure recovery in optimum diffusers is described in the referenced article. This method was used to calculate pressure recovery-versus area ratio for annular diffusers as shown on Figure 106. The experimental results of the previously discussed NASA testing have been included on this figure. Also included are some experimental results for an annular diffuser downstream of a compressor. This work, reported in Reference 35, included extensive probing of the compressor discharge flow to determine the influence of the size of the blade wakes on the performance characteristics of a cylindrical core, annular diffuser. Three diffusers of constant length, but varying outer wall slope, were tested behind an axial compressor. The configuration tested has a constant area mixing section of $L/\Delta R \sim 1.25$ between the compressor discharge and diffuser entrance section. Static pressure recovery from these tests has been included on Figure 106. Note that the diffuser with the largest area ratio (corresponding to a 15 degrees outer wall) is operating in stall. The correlations of Sovran and Klomp (Reference 34) show this design should operate in a transitory stall mode where diffuser effectiveness is seriously degraded. The conclusion drawn from this study was that the performance compared quite favorably with existing data and correlations for annular diffusers.

Tests conducted with about 12 degrees of inlet swirl showed almost no effect of performance for the small area ratio diffuser but indicated a 10 and 15 percent gain for the intermediate and largest area ratio configurations respectively. Other investigations have shown that swirl is beneficial from a performance standpoint, however, too much swirl can result in flow separation on the cylindrical centerbody with subsequent performance degradation.

All evidence points toward the maldistribution of flow downstream of the turbine as being the mechanism for poor conical diffuser performance. On this basis, a somewhat different approach was taken in the design of the Mini-BRU exhaust diffuser. The proposed design is shown on Figure 107. Four separate regions make up the entire diffuser. The entrance region is a constant area mixing section with a legnth prescribed as $L/\Delta R_1 = 1.0$. This is followed by an initial diffusion region with a contoured outer wall designed to produce a nearly linear static pressure rise. The third region is a conical expansion section extending to the design area ratio of the diffuser. A constant area section makes up the final region of the Mini-BRU diffuser. The latter section is added both to increase recovery and to help stabilize flow conditions in the upstream diffusion regions. The utility of a downstream tailpipe in diffuser applications is demonstrated experimentally in Reference 34.

Selection of the final configuration was based on a boundary layer analysis for several diffuser configurations. Initially a comparison was made between the calculated displacement thickness with length for the BRU conical and linear pressure rise diffusers. This comparison is shown on the upper half of Figure 108. The linear pressure rise diffuser has a rapid thickening of the displacement thickness during the latter stages of diffusion which should cause unstable conditions with boundary layer separation. The program indicated separation should have occurred at a lower static pressure recovery in the linear pressure rise diffuser than for the conical diffuser. Since the experimental data showed an opposite effect, there is good reason to believe that mixing may be the culprit. However, it is still extremely difficult to visualize how the linear pressure rise diffuser performed as well as it did in the BRU application. It is considered good diffuser design practice to reduce the rate of diffusion as the boundary thickens under adverse pressure gradient conditions.

The final Mini-BRU diffuser configuration is therefore a combination of previous turbine experience plus intuitive reasoning based on conventional diffuser information. The calculated displacement thickness increase with axial length is shown on the lower half of Figure 108 for the Mini-BRU design. These calculations indicate the boundary layer development is stable, with any regions of excessive thickening avoided entirely. It is believed that the performance of this diffuser design will be quite satisfactory.

Summary and conclusions. - Verification of predicted stage performance for the Mini-BRU radial turbine was accomplished using existing experimental data from BRU component tests conducted by NASA. Predicted performance at design conditions indicated the overall stage efficiency should not be less than 82.8 percent. Since the base performance has been obtained from a non-optimum design, higher performance is anticipated for the Mini-BRU configuration. Clearance loss is a significant portion of the overall loss. Efforts to minimize rotor-shroud clearances could pay reasonable dividends in terms of cycle efficiency.

Turbine design conditions and the resulting design parameters are summarized on Table XIV. The rotor incorporates ten full blades and ten splitters with an inducer tip radius of 1.429 inches. Twenty blades are required for the inducer section to avoid excessive loading and stalling along the pressure surface. The splitters are terminated in a region where the loadings begin to drop off rapidly. Having just ten blades in the exducer section of the turbine rotor eases the manufacturing problems to a large extent.

A total of 17 stator vanes was selected for the Mini-BRU design. This selection was made on the basis of limiting

TABLE XIV. - DESIGN PARAMETERS FOR MINI-BRU RADIAL TURBINE

General		Rotor	
Working fluid	XeHe mixture 83.8 M.W.	No. of blades	10 full blades 10 splitters
Inlet pressure	105 psia	Inducer tip radius	1.429 inches
Overall pressure ratio	1.47	Exit shroud radius	0.842 inches
Inlet temperature	2060°R	Exit hub radius	0.5 inches
Design weight flow	0.3571 lb/sec	$\beta_{2_{SHROUD}}$ = 69.6°	$\beta_{2_{HUB}}$ = 57.9°
		Inlet Stators	
Rotating speed	52,000 rpm	No. of blades	17
Specific speed	44.7	Inlet radius Exit radius	1.876 inches 1.483 inches
Stage efficiency	82.8 percent	β_{IN} = 0°	β_{OUT} = 78°

trailing edge blockage effects while maintaining a reasonable length for the uncovered portion of the flow. The exit flow angle of 78 degrees is higher than normal radial turbine design practice, but the improved aspect ratio of the stators shows this to be advantageous.

Maldistribution of flow downstream of the turbine has been identified as the primary mechanism causing performance difficulties with other turbine diffusers. Therefore, the diffuser design for Mini-BRU turbine application starts with a constatnt area mixing section followed by a linear static pressure rise section with limited diffusion. After the flow has had sufficient opportunity to dissipate blade wakes and accompanying vortices, the major portion of the diffusion required occurs in a section having a conical outer wall. Finally a constant area extension is added to stabilize the upstream flow while further enhancing recovery. The multi-sectioned diffuser for the Mini-BRU turbine should perform well at design conditions while maintaining reasonably good performance during off-design operation.

A summary of mean gas conditions at several locations within the turbine stage is shown on Figure 109. This includes total pressures, total temperatures, adiabatic efficiencies, and Mach numbers where significant. The data presented on Figure 109 serve to indicate the need for precise instrumentation when measuring performance, specifically in the diffuser section.

Turbine Stage Test

Introduction and summary. - This section summarizes the cold air test results of the radial turbine used in the Mini-Brayton Rotating Unit (Mini-BRU). The aerodynamic design conditions and air equivalent design values of this turbine are presented in Table XV. The flowpath is illustrated in Figure 110.

The test program consisted of a stator flow calibration and two turbine tests. Test No. 1 was conducted to establish the overall performance level of the turbine at the design point and to determine its off-design characteristics over a range of speeds and pressure ratios. Test No. 2 was performed to examine the axial clearance effects on the turbine performance along the 100 percent speed line. The design point total-to-wheel exit total efficiency of 0.836 was attained after corrections for effects of clearance, Reynolds number, internal heat transfer and inlet plenum pressure loss were made and is in good agreement with the design intent of 0.834. The test results also indicate a surprising sensitivity of efficiency to axial clearance below the design value of 0.008 in.

All tests were performed with cold air as the working fluid. However, by assuming the equivalence in specific work and no change in efficiency, the final test results were translated into the HeXe fluid for direct use in the Mini-BRU performance program. Comparison of results obtained with HeXe mixture and cold air as the working fluid indicated a very small difference in turbine performance over the range of tested pressure ratios and speeds.

Reynolds number significantly affected performance level of this turbine due to its small size. In order to minimize the Reynolds number effect on the performance, the design point test was run with cold air at an inlet temperature of 578°F and an inlet pressure of 30.1 psi which corresponds to the design Reynolds number of HeXe mixture at equivalent design point speed and pressure ratio.

TABLE XV. - AERODYNAMIC DESIGN VALUES SUMMARY

	Design Point Values	Air equivalent Design values (U.S. Standard Sea Level)
Cycle working fluid	Xe-He	Air
Equivalent molecular weight	83.8	
Inlet total pressure, psi	150.0	
Inlet total temperature, °R	2060.0	
Exit total temperature, °R	1814.7	
Specific work, $\Delta H/\Theta$, Btu/lb	9.882	9.882
Blade jet speed ratio, $F_v/T-T$, $U_t/\sqrt{gJ\Delta H_{id}}$		
Pressure ratio (total-to-wheel exit total)	1.47	1.4194
Pressure ratio (total-to-diffuser exit static)	1.474	1.4228
Efficiency (total-to-wheel exit total)	.834	.834
Efficiency (total-to-diffuser static)	.829	.829
Physical speed, N, rpm	52000.	42851.
Corrected speed, $N/\sqrt{\Theta}$, rpm	26093.	42851.
Inlet corrected flow, $W\sqrt{\Theta}/\delta$, lb/sec	.0996	.05525
Physical weight flow, W, lb/sec	.3571	.05525
Reynolds number, $W/\mu\delta$	$.659 \times 10^5$	$.71 \times 10^5$*
Specific speed	44.7	45.21*
Axial clearance, inch	.008	
Radial clearance, inch	.008	
No. of rotor blades: full	10.	
half	10.	

*Based on cold air design point test conditions

Test rig description. - The turbine test rig consists of an inlet pipe with a flow measuring section, an inlet plenum, a turbine stator and rotor, a diffuser, a discharge duct with flow measuring section, a centerbody housing, a rotating assembly, a high speed quill shaft, and the Mini-BRU compressor which was used as a power absorber. The test rig assembly is shown in Drawing 3604610. The turbine wheel is overhung on a shaft supported by angular contact ball bearings. The test rig is a duplicate of the engine configuration from plenum inlet to diffuser exit, and the aerodynamic components are identical with those of the Mini-BRU, including the use of the same backface configuration of the turbine wheel and mating shroud. Figure 111 shows the test rig mounted on a test stand, while Figures 112 and 113 show stator and rotor prior to assembly.

This test rig was also used to statically flow the nozzle to obtain a flow coefficient for the plenum inlet-stator portion, without the rotor and bearing assembly group. The test setup is shown in Figure 114.

Instrumentation. - Instrumentation employed in this test rig is depicted in Figure 115. Airflow was measured by an ASME flat plate orifice and then measured again with a sonic nozzle. The inlet air temperature was set by mixing the cold and hot air in the laboratory inlet system so that the turbine discharge temperature was approximately cell ambient. This together with the insulation around the discharge duct section maintained the heat transfer to or from the surroundings to a minimum. Capacitance probes were located at the turbine wheel inlet and exit to determine the running clearance during data acquisition.

Rotor speed was measured with a magnetic speed pickup.

Stator Inspection and Flow Test. - Stator hardware was inspected before the test rig assembly. The measured stator throat dimensions and other critical dimensions are listed in Table XVI. The measured throat area of 0.23605 $in.^2$, with an average fillet radius of 0.015 in., is 3.25 percent less than the design value of 0.24396 $in.^2$.

Following this inspection, a flow calibration of radial rig configuration, without the rotating group bearing carrier in place, was conducted. This was accomplished by running successively higher total-to-static pressure ratios across the nozzles until choked flow was achieved. At designated airflows, manual surveys at the 90° bend inlet were taken using bent tube

TABLE XVI. - STATOR DIMENSIONS

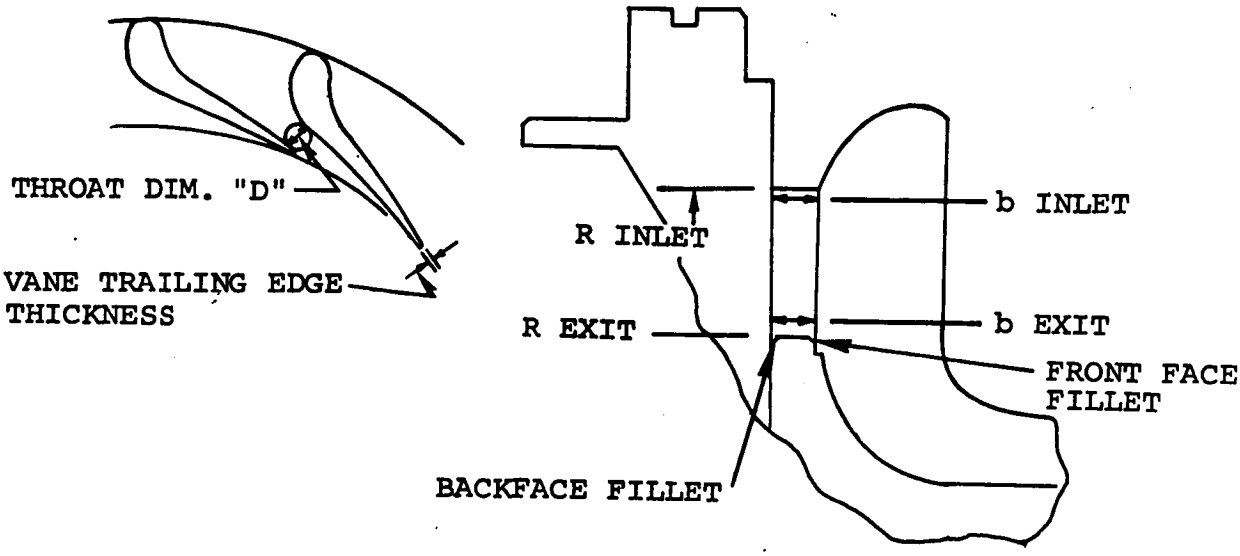

VANE NO.	THROAT DIM. (IN.)	EXIT "b" (IN.)
1	0.108	0.128
2	0.109	0.128
3	0.109	0.128
4	0.109	0.128
5	0.109	0.128
6	0.110	0.128
7	0.110	0.128
8	0.111	0.128
9	0.110	0.128
10	0.109	0.128
11	0.109	0.128
12	0.109	0.128
13	0.109	0.128
14	0.109	0.128
15	0.109	0.128
16	0.109	0.128
17	0.109	0.128
AVE.	0.109235	0.128

AVE EXIT "b"	0.128 in.
AVE RADIUS	
INLET	1.876 in.
EXIT	1.483 in.
AVE EXIT FILLETS	
FRONT FACE	0.015 in.
BACK FACE	0.015 in.
MEASURED THROAT AREA	0.23605 $in.^2$
DESIGNED THROAT AREA	0.24396 $in.^2$

$\Delta A/A_{DESIGN}$ = -3.25 PERCENT CLOSED

total pressure probes. The objective of this flow test was to provide an insight into the loss distribution in this turbine component and ascertain the effective area of the nozzle.

In addition to the normal side screen rotor blade shape inspection, the rotor throat dimension was measured at two radii for each of the 10 full blades. Figure 116 shows the design variation of rotor throat opening (excluding filter blockage) as a function of exducer radius. Numerical integration gives a design throat area per passage of 0.0555 $in.^2$. The corresponding measured throat area represented by dashed curve in the figure yields a measured throat area per passage of 0.05152 $in.^2$ which is 7.2 percent smaller than the design intent. However, the stator was 3.25 percent small so that stator throat to rotor throat area ratio for the tested turbine is only 4.26 percent larger than design intent (rotor tip clearance effects excluded).

Mechanical checkout. - After the test rig was installed into the test cell, a preliminary mechanical checkout run was initiated. During this run, high vibration levels were experienced in the range of desired operating speeds. Review of critical speed calculations indicated that rigid body critical speeds were apparently contributing higher forces than anticipated. A proven solution for this type of problem is to mount the anti-friction bearing outer races on fluid film mounts. This procedure was implemented and the resulting vibration characteristics were acceptable. Parameters such as vibration, rotor shroud clearance, oil temperature, rotor dynamic movement, and bearing temperatures were continually observed during all the testing.

Test No. 1. - During this turbine baseline performance testing, trouble was encountered in matching the turbine and the load compressor (Mini-BRU closed loop compressor rig) at low and high turbine pressure ratios. At the low turbine pressure ratio points, the compressor work could not be reduced enough to match the turbine output power. This situation was remedied by running the closed loop compressor in a vacuum to match the turbine output power. At high turbine pressure ratios, the load compressor was unable to absorb all the power produced by the turbine even with the maximum possible compressor loop pressure. This problem was solved by opening the loop, reversing the compressor flow direction, and running the turbine with a vacuum discharge. The test covered four equivalent corrected speed lines of 60, 80, 100 and 110 percent of the design value with design clearance. Data for five pressure ratios for each speed line were recorded.

Test No. 2. - The hardware was identical to that of Test 1 except the shims were changed to adjust the axial clearance. Tests with two different axial clearances of 0.0034 in. and 0.0128 in. for a constant 0.010 in. radial clearance were run at 100 percent speed over a range of pressure ratio. These data were used to determine the effect of axial clearance on cold air turbine efficiency.

Test data acquisition. - Test data such as pressure, temperature, speed, and clearance probe output, etc., were acquired through a system of scanner valve-transducers, multiplexers, and a high speed digital system capable of recording data at a rate of 200 samples per second. These data are then transcribed to tape for use later in the data reduction program which converts test measurements to engineering units, and plots performance curves.

Test Results

Stator flow coefficient. - The plenum inlet corrected flow as a function of imposed inlet-to-ambient static pressure ratio is shown in Figure 117. The upper curve in the figure represents the first test results which yielded a choking flow coefficient greater than 1.0. A leak was suspected, and further inspection indicated a small amount of vane end wall clearance was present. This clearance was eliminated and a second test was performed. The results of the second test are shown in the lower curve of Figure 117. Comparison to the sonic isentropic flow of 0.080997 lb/sec attainable with the measured geometric throat area of 0.23605 $in.^2$ indicates a choked flow coefficient of 0.9726. This implies a pressure loss of 0.0274 in $\Delta P/P$ from plenum inlet to stator throat when the throat is in a choked condition.

Baseline turbine performance. - The test was conducted in the AIRPHX turbine test cell which is generally used to test much larger turbines. As a consequence, Mini-BRU turbine flow rates were such that flow control valves were operated in a barely cracked position which resulted in flow instabilities and difficulties in obtaining the desired stable operating conditions. As a result, some of the test data was scattered which presented some slight difficulties in its analysis. However, test results were correlated with the aid of the relationship between F_v and ψ.

As described in References 36, 37 and 38, a small radial turbine performance can be characterized by F_v as a function of ψ. F_v is a nondimensional parameter which relates wheel

tip speed and pressure ratio. ψ is a torque parameter equal to η/F_V where η is efficiency. For a fixed speed line, a linear variation of F_V with c can be approximated within a small range of F_V.

The test data was then nondimensionalized by plotting F_V as a function of ψ as shown in Figures 118, 119, and 120. The deduced test result of efficiency as a function of pressure ratio for the four speed conditions is presented in Figures 121 122, 123, and 124. The corrected flow parameter is shown in Figure 125.

In order to permit use in the Mini-BRU performance program, the cold air test results were translated from air to He-Xe mixture, as shown in Figures 126 through 130, by utilizing the equations described in Reference 36. The corrected flow of He-Xe mixture at design point condition was increased by a factor of 1.803 times the equivalent cold airflow rate.

Axial clearance effect on turbine efficiency. - The cold air turbine tests were also run with the different axial clearances of 0.0034 in. and 0.0128 in. at 100 percent speed over a range of pressure ratios for a constant radial clearance of 0.010 in. Figure 131 shows a comparison of these results to the baseline data. For the test using 0.0128 in. axial clearance the results are within 0.5 percent of the baseline value except in the lower pressure ratio region where the efficiency drops rapidly for decreasing pressure ratio. The performance improvement for the small axial clearance is readily apparent through the whole pressure ratio range as compared to that of the baseline curve. Figure 132 shows a comparison of the measured axial clearance effect with the correlation curve used in the design phase (see Figure 133). The test results indicate a surprising sensitivity of efficiency to axial clearance below 0.008 in.

Turbine axial thrust at engine design operating condition. - The local static pressures along the backface and rotor shroud were measured by static pressure taps as shown in Figure 134. The local static pressures of the He-Xe at engine design condition were obtained by translating the inlet total to local static pressure ratio from air to He-Xe mixture. The resulting axial thrust was found to be 24.7 lb_f which is composed of various force terms as tabulated in Table XVII.

TABLE XVII. - TURBINE AXIAL THRUST FORCES

Force due to backface static pressure	-468.0 lbf
Force due to static pressure along rotor shroud, rotor exit and downstream hub section	+491.2 lbf
Force due to the momentum exchange by the fluid	+ 1.5 lbf
Net Axial Thrust (Forward)	+ 24.7 lbf

"+" indicates the forward direction or opposite of flow direction.

Design point efficiency. - The measured 0.82 total-to-total efficiency was obtained with a running axial clearance of 0.008 in. and a radial clearance of 0.010 in. The radial clearance of 0.010 in. was slightly higher than the design value of 0.008 in. A 0.4 percent efficiency gain can be obtained if the radial clearance correction is made from 0.010 in. to 0.008 in. based on the correlation curve illustrated in Figure 132.

The inlet plenum total pressure loss, which was assumed to be negligible in the design phase, was found to be 0.2 percent in $\Delta P/P$ and thus results in a net loss of 0.4 percent in overall turbine efficiency.

The internal heat transfer played an important role in determining the efficiency in this test because of the small overall temperature drop. The approximate value calculated from the measured test condition was 0.5°F, which results in a one point efficiency decrement.

The calculated Reynolds number for cold air at the tested design point condition was 71720 which is 9 percent higher than the design value of 65880. Therefore, a Reynolds number correction to the measured efficiency value was made based on the empirical formula developed by NASA-LeRC in Reference 39. The correction showed that the design point efficiency corrected to the design Reynolds number was decreased by 0.2 percent.

After the measured cold air efficiency value was corrected for all previous stated effects, as shown in Table XIX, the corrected efficiency value of 0.836 is in good agreement

TABLE XIX. - DESIGN POINT EFFICIENCY CORRECTIONS

	Total-to-Wheel Exit Total Efficiency
Efficiency measured at design point condition	0.82
Efficiency corrected to design clearance	0.824
Efficiency excluding the 0.2 percent inlet plenum pressure loss	0.828
Efficiency excluding 0.5°F internal heat transfer effect	0.838
Efficiency corrected to design Reynolds number	0.836
Design efficiency predicted	0.834

with the design intent of 0.834. The corrected flow at design speed and pressure ratio is 3.5 percent higher than the design value. In Section 3.1.1 the ratio of stator throat to rotor throat area for this turbine was found to be 4.26 percent greater than design intent. This may have been a contributing factor in spite of the fact that the stator throat area was 3.25 percent too small. No other cause is readily apparent without further investigations beyond the scope of this program. Comparison of the test results with design values are listed in Table XX.

Diffuser performance. - The exhaust diffuser consists of four separate regions as shown in Figure 135. It starts with a constant area mixing section followed by a limited diffusion region with a contoured outer wall designed to produce a nearly linear static pressure rise. After the flow has had sufficient opportunity to dissipate blade wakes and accompanying vortices, the major portion of the diffusion required occurs in a conical expansion section extending to the design area ratio of the diffuser. The last constant area section is added to help stabilize the upstream flow conditions while further enhancing recovery.

Based on the values of area ratio and non-dimensional length of this diffuser, the correlations of Souran and Klomp (Reference 40) predict a range of static pressure recovery from 0.62 to 0.72 corresponding to the magnitude of the inlet layer boundary thickness ratio ranging from 0.01 to 0.08. However, this prediction is only applicable to those diffusers having symmetrical and uniform inlet velocity profiles. Any deviation from this ideal inlet condition would result in the degradation of the above predictions. In some of the experimental work performed by NASA-LeRC, a high diffuser performance of 0.65 static pressure recovery was demonstrated. The diffuser was designed with the linear static pressure rise method. Based on intuitive reasoning from the literature and some previous AIRPHX design experience, the final prediction of 0.6 static pressure recovery for this diffuser was determined.

The measured diffuser static pressure recovery, C_p, at design point condition was 0.589 and is in close agreement with the design value of 0.6. The percent of total pressure loss, as measured by the Kiel probes, was found to be 0.015 which resulted in a loss coefficient, $\bar{\omega}$, of 0.251 for the inlet Mach number of 0.093. Assuming one dimensional incompressible flow, the following relation can be derived.

$$C_p + \bar{\omega} = C_{pi}$$

TABLE XX. - COMPARISON OF TEST RESULTS WITH DESIGN VALUES

	Design Values (Xe-He)	Measured Results (Cold Air)	Translated Values (Xe-He)
Percent corrected speed	100	100	100
Pressure ratio total-to-wheel exit total	1.470	1.423	1.474
Efficiency total-to-wheel exit total	0.834	0.836	0.836
Pressure ratio total-to-diffuser exit static	1.474	1.427	1.479
Efficiency total-to-diffuser exit static	0.829	0.830	0.830
Corrected flow	0.0996	0.0572	0.10312

where

$$C_{pi} = 1 - (1/AR)^2$$

The term C_{pi} is the ideal static pressure recovery coefficient and is a functional only of the diffuser area ratio, AR. The sum of the measured values of C_p and $\bar{\omega}$ is 0.840 and is in good agreement (0.4 percent), with the ideal static pressure recovery, C_{pi}, of 0.837 which was independently calculated from the area ratio.

The static pressure distribution along the length of the diffuser is shown in Figure 136. The static pressure distribution is also presented here in terms of a local static pressure recovery coefficient, defined as;

$$C_p \text{ local} = \frac{P_{s,L} - P_{s,DI}}{\bar{P}_{t,DI} - \bar{P}_{s,DI}} = \frac{P_{s,L} - P_{s,DI}}{\bar{q}_{DI}}$$

where $P_{s,L}$ is the local static pressure, $P_{s,DI}$ is the static pressure at diffuser inlet hub or shroud, and $\bar{P}_{s,DI}$ and $\bar{q}_{DI}$ are the diffuser inlet average static pressure and dynamic pressure, respectively. This local recovery parameter, as well as the ideal recovery, is plotted in Figure 137 versus diffuser axial length. It can be seen that the major portion of the diffusion is completed in the region having a conical outerwall while in the linear static pressure rise region, the diffusion is limited to a relatively small amount. In the last constant area section, the flow shows continuing diffusion even without area variation.

This diffuser shows relatively good performance with a 0.704 diffuser effectiveness ($E = C_p/C_{pi}$) bleed on the design area ratio of 2.5 and $C_p = 0.589$. This performance is due to sufficient length being provided to allow the flow to diffuse gradually without significant separation occurring.

BEARING DEVELOPMENT

Introduction

Closed Brayton cycle power systems operate on an all-gas thermodynamic cycle which requires heat exchangers to introduce, reject, and recuperate the thermal input. Contamination of these heat exchangers can destroy the effectiveness of the entire power system. For this reason, it is highly desirable to support the rotating components of a closed Brayton cycle engine on cycle gas bearings, thereby eliminating the possibility of system contamination from an external lubrication system. In addition to eliminating a contamination source, gas bearings also provide low power loss and extremely high reliability.

Summary

Foil gas bearings were designed and developed for the Mini-BRU application on the basis of providing the most reliable, stable, and low power loss bearing system compatible with motoring starts. Primary importance was placed on minimum power loss so as to assure high BRU efficiency at low electrical power levels of operation. The bearings were required to operate in a helium-xenon (HeXe) gas mixture with a molecular weight of 83.8 over a pressure range of 29 to 100 psia. Journal and thrust bearings were designed to operate under a 1-g environment in all attitudes. The journal bearing design had the additional requirement of carrying the imbalanced magnetic loads of the alternator rotor. The magnetic imbalanced loads varied as a function of rotor eccentricity and power level. The thrust bearing was required to carry aerodynamic loads which varied as a function of the pressure and power level of operation and ranged between 2 and 10 pounds. Design speed of the bearing system was 52,000 rpm.

The development of the bearing system involved 143 separate tests on journal and thrust bearing test rigs. The bearing development encompassed the following design variations:

(1) Six foil segment-journal bearing

(2) Eight foil segment-journal bearing

(3) Sway space variation-journal bearing

(4) Preformed radius variation-journal bearing

(5) Ten pad thrust bearing

(6) Twelve pad thrust bearing

(7) Leaf type thrust bearing spring

(8) Three-dimensional integral thrust bearing spring

(9) Stainless 302 (PCM) foil material

(10) Inconel 750X foil material

(11) Teflon-S foil coating

(12) OBD-26 foil coating

Test rig bearing development was concluded with the selection of a Mini-BRU foil bearing system design which was subsequently subjected to proof testing in the Mini-BRU Simulator and Alternator unit. The bearing design selected consisted of an eight foil Teflon-S coated journal bearing and a ten pad Teflon-S coated thrust bearing with a three-dimensional photochemically machined (PCM) spring. The dimensions for the journal and thrust bearing are shown in Table XXI.

The journal and thrust bearing geometric nomenclatures are illustrated in Figures 138 and 139 respectively. A thrust bearing spring of the geometry shown in Figure 140 is used to generate the proper bearingshape shown in Figure 141.

The actual journal and thrust bearing design configurations are shown on Drawings 3604338, and 3604339 attached. The thrust bearing spring is shown on Drawing 3604340.

The basic dimensions of the thrust bearing rotor used in conjunction with the Mini-BRU thrust bearing are shown in Figure 142 and on Drawing 3604334.

Preliminary Design

Engine design features. - Initial sizine of the Mini-BRU foil bearing system was made using the iterative process of cycle analysis, alternator sizing, layout, rotor dynamics, and aerodynamic analysis. The engine assembly shown in Figure 143 depicts the bearing arrangement selected for the Mini-BRU rotating group. The rotating group is supported radially by two foil gas journal bearings straddling the Rice alternator rotor. The bearings are located in the secondary "air" gaps of the alternator system. This design feature causes the alternator flux to pass directly through the foil bearings, but provides a compact rotating group arrangement and a high third (shaft bending mode) critical speed. The axial support for the rotating group is provided by a double acting foil gas thrust bearing located between the compressor and alternator rotor. The basic characteristics of the bearing spacing and rotating group are shown in Figure 144.

TABLE XXI. - FOIL BEARING DIMENSIONS

Journal Bearing

Number of Foils	8
Foil Thickness (Total)	0.006 in.
Preformed Radius	0.570 in.
Foil Arc Length	0.770 in.
Sway Space	0.008 in.
Foil Coating	Teflon-S, 0.001 in. thick
Foil Material	Stainless 302
Shaft Diameter	1.038 in.
Axial Foil Length	0.900 in.

Thrust Bearing

Number of Pads	10
Pad Thickness (Total)	0.004 in.
Base Thickness	0.006 in.
O.D.	1.750 in.
I.D.	1.090 in.
Foil Coating	Teflon-S, 0.001 in. thick
Foil Material	Stainless 302
Spring	Stainless 302 Integral PCM

Journal bearing sizing. - Because of the decision to place the journal bearings into the alternator secondary air gaps, the bearing diameter became a function of the area required to pass the peak alternator flux without choking. Alternator design optimization requirements necessitated the selection of a 1.038 inch shaft diameter and thereby set the bearing diameter to the same value. The bearing axial length of 0.9 inches was tentatively selected on the basis of providing an adequate bearing area necessary to support the predicted dynamic and magnetic loads. Secondary influences on the selection were L/D ratio and rotor dynamics.

Thrust bearing sizing. - Preliminary aerodynamic analysis indicated that the net aerodynamic thrust would vary between 2 and 10 pounds as a function of the pressure and power level of Mini-BRU operation. The net thrust values were calculated as the difference between the large opposing thrust loads of the compressor and the turbine and as such were subject to a high percentage of error. In consideration of the objective of designing a bearing system with minimum power losses, it was decided to size the thrust bearing on the basis of the calculated ten pound aerodynamic thrust load. In the event that subsequent aerodynamic tests of the compressor and turbine components revealed higher net thrust loads, the turbine wheel would be scalloped to balance the thrust within the capability limits of the original thrust bearing design. This procedure would assure a minimum bearing loss system. Should aerodynamic component testing confirm net aerodynamic thrust loads of lower than 10 pounds, modifications could be made to the thrust bearing which would result in a further decrease in bearing losses.

The initial sizing of the foil thrust bearing incorporated a 1.75 inch OD and a 1.09 inch ID and provided a bearing area of 1.47 square inches.

Bearing spring rates. - Tentative selection of desirable bearing spring rates was made on the basis of rotor dynamics, aerodynamic clearances, magnetic imbalance of the alternator rotor and thermal analysis.

Journal bearing. - Rotor dynamics analysis indicated that rigid body criticals controlled by journal bearing spring rates occurred between 9000 and 19,000 rpm for spring rates of 2500 to 7500 pounds/inch. The critical speeds as functions of foil bearing spring rates are shown in Figure 145. Since the criticals were relatively insensitive to the spring rates, the factors of magnetic imbalance, aerodynamic clearances and thermal growth dominated the criteria for spring rate selection.

Magnetic imbalance is primarily a function of rotor eccentricity to the alternator stator. The imbalance may be considered as a negative spring rate and is summarized in Table XXII. The selection of bearing spring rates must be made on the basis of maintaining the minimum rotor eccentricity consistent with bearing preload, rotor weight, and the negative spring rate of the alternator. The load-deflection characteristics of the final Mini-BRU journal bearing design are shown in Figure 146. It can be seen from this curve that the rotor weight of approximately 1 pound per bearing would cause an eccentricity of approximately 0.0002 inch. The resulting magnetic imbalance in the form of a negative spring rate would be approximately 206 pounds/inch at full design speed. The net spring rate of the bearing can be derived by subtracting the magnetic imbalance spring rate from the value derived from the load deflection curve. For example:

Between 1 and 3 pounds load

$$K_{Brg} = \frac{2}{0.00079} = 2531 \text{ pounds/inch}$$

$$\text{Net } K = K_{Brg} - K_{Alt} = 2531 - 206 = 2325$$

Net K = 2325 pounds/inch

This spring rate provides good bearing stability and minimizes the dynamic loads in the bearings. In addition, the radial clearances of the alternator and aerodynamic components are maintained within close limits which assure maximum efficiencies of all components.

Thrust bearing. - The rotor dynamics analysis revealed no significant axial loads to the thrust bearing. Consequently, the thrust bearing springs were designed to provide precise control of the preloads and maintenance of the aerodynamic component axial positioning within 0.001 inch over the entire operating range.

The thrust bearing spring load-deflection characteristics are shown in Figure 147.

Ideally, on a double acting foil thrust bearing, it is desirable to preload each bearing near the knee of the spring load-deflection curve. In this manner, it is possible to utilize the non-linear spring characteristics to provide close axial control of the rotating group while maintaining bearing stability and minimum power loss. For example, the Mini-BRU thrust

TABLE XXII. - MAGNETIC IMBALANCE - ALTERNATOR OPERATION

STANDSTILL FORCE "SPRING RATE"[1]

LOCATION	1/2 CAPSULE	1 CAPSULE	2 CAPSULES	3 CAPSULES	MOTOR START 300 Hz 1.6 P.U. V/Hz
AUXILIARY GAP (EACH BEARING) LB/IN. OF DISPLACEMENT	616	712	992	1307	-
MAIN GAP LB/IN. OF DISPLACEMENT	963	1057	1295	1524	2695

[1]VALUES ARE IN THE DIRECTION OF MINIMUM AIR GAP.

EFFECT OF ROTATION: THE SPRING RATE WILL BE REDUCED BY A FACTOR OF 2 AT SPEEDS GREATER THAN 7000 RPM AND WILL BE DIRECTED AT AN ANGLE OF 24.5 DEGREES PRECEEDING THE MINIMUM AIR GAP.

bearing is assembled to provide approximately 2.5 pounds preload on each bearing. A cross section of the thrust bearing is shown in Figure 148 and illustrates how each spring preloads the bearing against the rotor in opposition to the bearing and spring on the other side of the rotor. Referring to the load-deflection curve of Figure 147, it can be seen that under a preload of 2.5 pounds, each thrust spring is deflected approximately 0.00175 inch. In actual operation, as a thrust load is applied to one side of the thrust bearing, the spring under the bearing deflects and moves up the load-deflection curve until a balance of spring forces and aerodynamic loads is reached. The opposite spring is unloaded and moves down the load-deflection curve to minimize the load and power loss for the unloaded bearing. Due to the non-linear shape of the load-deflection curve, a 10 pound aerodynamic load can be carried by a 10.5 pound load on one bearing and a 0.5 pound load on the opposite bearing. It is noted that the maximum aerodynamic load is carried with approximately a 0.001 inch axial deflection, thereby assuring maximum aerodynamic performance over the entire range of power output.

Bearing Materials and Coatings

Thermal analysis. - The thermal analysis of the Mini-BRU is shown in Figure 149 and Figure 150 which show the engine steady state temepratures for low power and high power operation. This analysis provided the basis for the initial selection of the foil materials and coatings. Soakback temperatures resulting from engine shutdown were also calculated and found to be highest at the turbine-end journal bearing. The maximum soakback temperature was established at 550°F.

Material selection. - On the basis of the thermal analysis, the journal and thrust foil bearings would not exceed 450°F steady state temperatures or short term soakback temperatures of 550°F. These temperatures are considered to be well within the acceptable temperature range of most metallic foil materials, except aluminum. Considering the moderate temperature environment, the selection of foil materials could then be made on the basis of the required physical and chemical properties. As a practical matter in fabricating, handling, assembly and service, a corrosion resistant material was desirable. In addition, the material properties, such as a high modulus of elasticity, high endurance limit, and factors relating to desirable spring characteristics, were of primary consideration. Based on prior experience, spring temper 302 Stainless and Inconel 750X materials were selected for evaluation. The Inconel 750X material offers forming advantages and a higher modulus of elasticity, while the 302 Stainless offers ready availability, low cost, and absence of high cost heat treat requirements. Bearings

were fabricated and tested using both materials, resulting ultimately in the selection of 302 Stainless because no significant advantage could be found for the more expensive Inconel 750X.

Foil coatings. - Coatings are applied to the foil bearings to reduce starting friction and prevent damage to the journal or foil during startup and shutdown when high shock load operating conditions develop and surface-to-surface contact is made. Based upon the thermal analysis and predicted foil surface temperatures, two coatings were selected for comparative testing. One coating, designated Teflon-S, is a stratified composition of Teflon and proprietary resins furnished by DuPont. This coating has been used successfully in foil bearing applications for over 60 million hours of operation, but is limited to approximately 550°F steady state operation. The second proprietary coating is produced by Thermec Engineering and is designated OBD-26. It is a multi-layer coating consisting of aromatic and polyimide compounds. This coating has an operating temperature capability of approximately 650°F but is softer and less tough than the Teflon-S coating. The coatings have different friction characteristics and, therefore, impact the motoring start requirements of the Mini-BRU.

Starting Characteristics

The Mini-BRU is started and brought to self-sustaining speed by using the alternator as a motor. The motor must exceed the starting drag torque of the foil bearings and provide sufficient excess torque for acceleration of the rotating group to operational speed.

The foil bearing design preload characteristics and foil coating play a decisive role in a successful motoring start of the Mini-BRU. The inidividual starting torque characteristics of the journal and thrust bearings coated with Teflon-S are shown in Figures 151 and 152. These individual torque characteristics are combined for two journals and two thrust bearings and result in the starting torque versus speed relationships for the complete Mini-BRU bearing system shown in Figure 153. As can be seen from this figure, the alternator motoring start characteristics must lie to the right of the bearing torque-speed curve if a successful start is to be made. Teflon-S coating was selected in preference to the OBD-26 coating because less torque is required to accelerate the rotor above 2000 rpm. A comparison of the starting drag torque of geometrically identical journal bearings coated with Teflon-S and OBD-26 is shown in Figure 154. Teflon-s coated foils with lower starting torques permit a larger differential motor torque availability for acceleration and increasing aerodynamic loads.

Another factor influencing starting drag torque was identified during development testing. Variation of the curing temperature of the Teflon-S foil coatings produced the general starting drag torque trends shown on Figure 155. The final bearing design included a 650°F Teflon-S cure which provided the lowest overall starting drag torque and the best resistance to wear.

Bearing Performance

Bearing system power losses. - For reasons of economy and ease of testing, the bulk of the Mini-BRU foil bearing development was conducted using air as the test gas. Final bearing configurtations were then operated in an argon environment and correlation factors established to permit analytical prediction of the bearing performance in the Mini-BRU helium-exenon environment. Tests were also conducted at various ambient pressures to establish bearing correlation factors for operation in the Mini-BRU pressure environment.

The predicted bearing system losses of the Mini-BRU, operating at the design conditions of 52,000 rpm with Xe-He gas and with 1, 2, and 3 isotope capsule power, are shown in Tables XXIII and XXIV. Table XXIII presents the predicted bearing data for the 1-g, horizontal orientation while Table XXIV presents predicted bearing data for the 1-g, vertical orientation. These values for bearing losses are calculated by taking measured test rig bearing performance and conditions, and applying corrections for gas viscosity, bearing loadings, and pressure conditions of the Mini-BRU.

The predicted Mini-BRU bearing losses may be higher than would actually be experienced in operation due to the inability to accurately measure the internal gas temperature of the test rig bearings and provide a positive temperature reference for corrections to the Mini-BRU operating conditions.

Some evidence exists in the test rig data reduction that actual internal bearing temperatures may be several hundred degrees higher than indicated by the metal foil temperatures. As a result, all corrections, based upon the differentials between the test rig metal foil temperatures and the Mini-BRU bearing temperatures as determined by thermal analysis, would be higher than corrections based upon suspected bearing internal gas temperatures. Determination of the exact values for bearing losses of the Mini-BRU is not possible with the data presently available. The predicted bearing losses are conservative in the sense that actual losses will probably be lower and thereby provide a margin for Mini-BRU efficiency and thermal allowances such as alternator and bearing cooling.

TABLE XXIII. - PREDICTED MINI-BRU BEARING POWER LOSSES

FOR A 1-G, HORIZONTAL ORIENTATION

	Total Journal Bearing Loss, Watts	Total Thrust Bearing Loss, Watts	Total
1 HSA (Maximum pressure = 34 psia)	90	81	171
2 HSA (Maximum pressure = 69 psia)	126	110	236
3 HSA (Maximum pressure = 106 psia)	164	145	309

TABLE XXIV. - PREDICTED MINI-BRU BEARING POWER LOSSES

FOR A 1-G, VERTICAL ORIENTATION

1 HSA (Maximum pressure = 34 psia)	46	90	136
2 HSA (Maximum pressure = 69 psia)	54	119	173
3 HSA (Maximum pressure = 106 psia)	61	154	215

In the event that absolute bearing loss values for the Mini-BRU must be established, the most practical method of measuring the losses would be a modification to an operational Mini-BRU to permit direct reading of each bearing reactive torque. This modification would be costly to incorporate and would require sophistication to maintain the accuracy and repeatability of Mini-BRU characteristics.

An optional approach to the problem would be to modify the existing test rigs to permit simulation of the Mini-BRU environment with respect to gas type, temperature, and pressures. Again the costs would be high, and exact simulation of the Mini-BRU characteristics would be difficult.

A third approach to the problem would be to attempt measurement of the actual gas temperatures within the test rig bearings and apply corrections on that basis. The installation of subminiature thermistors within the test rig bearings would provide better temperature data than presently available; however, such instrumentation would also be costly and probably would extensive testing and analysis to assure accuracy.

Individual bearing losses. - The bearing system power losses were derived from the summation of individual bearing losses established for air and argon gases. The journal bearing losses of the final bearing configuration operating at the design speed of 52,000 rpm and with air and argon gas are shown in Figure 156 and Figure 157.

The corresponding power losses of the final thrust bearing configuration are shown in Figures 158 and 159. Corrections for gas, pressure, and temperature of the Mini-BRU system were applied in accordance with the relationships shown in Figures 160 through 165. These corrected individual bearing losses were then summarized to produce the predicted Mini-BRU bearing system losses previously shown in Tables XXIII and XXIV.

Load capacity. - The ultimate load capacities of the journal and thrust bearings were not established primarily due to pressure limitations of the test rig bearing loading gage and an interest in preventing damage to the test rigs in the event of a bearing failure. However, the bearings were tested well above design loads, and each indicated a good margin of safety. The thrust bearing was tested to 20 pounds load in air, and the resulting data indicated that the ultimate load capacity was in excess of 30 pounds. The journal bearing was tested to 11 pounds load in air. Analysis of the test data indicates that 11 pounds is very near the ultimate load capacity of the bearing operating in air. A plot of the journal bearing power losses versus load in air is shown in Figure 166. As can be seen, the power losses

jumped from 27 watts at a 10 pound load to 39 watts at an 11 pound load indicating very thin gas films. It should be noted that the bearing was not damaged in any manner while operating at the 11 pound load.

A corresponding test in argon using the same test bearing was also made. The results of that test are shown on Figure 167. Operation in argon gas permitted loads to 11 pounds without any jump in power losses as experienced in air at an 11 pound load. The increased viscosity of the argon gas compared to air provided a thicker gas film and a larger load margin. The corresponding power loss jump for the bearing operating in argon gas was not established during the test because the jump characteristic was not recognized until the data was reduced. Corresponding load capacity improvement with higher viscosity gases has been documented on the thrust bearing.

Based on previous testing in other programs, the Mini-BRU journal and thrust bearings operating in He-Xe gas probably have ultimate load capacities of approximately 15 and 40 pounds, respectively. When compared to the design loads of 1.5 and 10 pounds for the journal and thrust bearings, it would appear that the bearings were grossly over-designed. This is not the case, because both bearings were designed to generate gas films at low speeds and reduce the starting torques to values within the capability of the starting motor, i.e., alternator. Another dominant consideration in the sizing of the bearings was the permissible radial and axial deflection of the bearings under aerodynamic, and magnetic loads. Bearings designed to meet only load capacity requirements would have resulted in low bearing spring rates and excessive displacement of the rotating group, and loss of aerodynamic and alternator clearances.

Test Description

Test equipment. - To facilitate the development of the Mini-BRU foil bearing system, separate test rigs for the thrust and journal bearings were designed and fabricated. Each test rig incorporated a rotating group supported on gas bearings and driven by a small air turbine. Individual journal and thrust test bearings were mounted to permit loading and measurement of the bearing reactive torque.

Thrust bearing test rig. - A cross section of the thrust bearing test rig is shown in Figure 168. Initially the rotating group was supported on carbon hydrostatic air bearings, but was subsequently modified to foil type air bearings to improve stability over the wide speed range of testing. The test bearing rotor was mounted on the end of the rotor and is identified

as Item 14. The test foil bearing(s) were mounted in a bearing support which incorporated a spherical seated hydrostatic air bearing. This provision enables the test bearing reactive torque to be transmitted without friction to the strain gaged beam (Item 18) seen in View B-B. It should be noted that the test rig design also allows for transmission of the reactive torque of the rotor windage to the readout system. Windage is generated in two areas around the rotor as shown in Figure 169. When a single thrust bearing is under test, windage is generated on the outside clindrical surface and one face of the rotor. When a double thrust bearing is under test, windage is generated only on the cylindrical surface. To obtain actual thrust bearing losses from the test data, the windage losses must be analytically calculated and deducted from the total measured. Initially, the windage calculations were based upon NASA Reports TMX-52851 and -52905. The results were suspect, however, and tests 141 and 142 were conducted on the Thrust Bearing Test Rig to establish actual windage data for air and argon gases. The data from these tests was subsequently used to determine the actual losses of the final thrust bearing design.

The strain gaged beam shown in Figure 170 was equipped with two resistance type strain gages on each side of the beam. The strain gages were connected in a full bridge circuit shown in Figure 171. The strain gage bridge was connected to a Doric Model DS 300-T2 digital transducer indicator which permitted direct readout of the bearing rig reactive torque. The transducer indicator is shown in Figure 172. Four tests were conducted using an SR-4 strain gauge meter while the Doric transducer indicator was receiving some minor repairs. The SR-4 meter did not provide the accuracy or repeatability of the Doric indicator and was not subsequently used.

Load was applied to the test bearing by a 0.25 $in.^2$ area pneumatic piston acting through the hydrostatic spherical air bearing. The rig design permitted test of single thrust bearings or the complete Mini-BRU bi-directional thrust bearing assembly. The assembled thrust bearing test rig is shown in Figure 173.

Journal bearing test rig. - The journal bearing test rig design incorporated the basic features of the thrust bearing test rig relative to rotor support, drive, and test bearing loading. The journal bearing test rig was designed for horizontal operation of the rotating group with a single journal test bearing located between the test rig shaft support bearings. As with the thrust bearing rig, the journal bearing rig initially incorporated hydrostatic shaft support bearings, but was subsequently modified.

A cross section of the journal bearing test rig is shown in Figure 174. As on the thrust bearing test rig, the test bearing was mounted on a spherical hydrostatic air bearing which permitted bearing reactive torque to be measured directly through a strain gaged beam. It should be noted that the journal bearing test rig measured only bearing reactive torque without any windage losses included. Load was applied to the bearing by a 0.25 square inch area pneumatic piston acting through the spherical hydrostatic bearing. The assembled journal bearing test rig is shown in Figure 175.

Torque measurement. - Two strain gaged beams of different thicknesses were used during the testing. A thick beam (0.054 in.) was used to measure bearing torques during the start tests where torques were relatively high. A thin beam (0.047 in.) was used for all other running tests where torques were low and maximum sensitivity was desired. Sensitivities were such that torques could be read to within 0.001 in.-lb repeatability.

Calibration. - In order to assure the utmost accuracy of the test data, the test rig instrumentation was calibrated prior to each test. Special emphasis was placed on accurate and frequent calibration of torque and speed instrumentation. The strain gaged torque beams on each rig were dead weighted and calibrated to assure accuracy and repeatability of 0.001 in.-lb torque. Speed measurements were made by monopole magnetic pickups sensing a six toothed rotor on the test rig shafts for all tests above 15,000 rpm. Low speed tests, such as starting torque tests, were made using a 30 toothed gear to assure reliable low speed measurement. Speed signals were displayed on digital readout Doric meters and recorded on Sanborn chart recorders. Conventional pressure gages, calibrated and certified to laboratory standards, were used for measuring bearing loads as applied by pneumatic pistons. Laboratory gages were also used to measure the ambient pressure during pressure testing of the journal and thrust bearings.

Test summary. - One hundred forty-three separate tests were conducted during the development of the Mini-BRU foil gas bearing system. Sixty-one tests were conducted on the thrust bearing or related components. Eight-two tests were conducted on journal type foil bearings.

Test rigs. - Both journal and thrust bearing test rigs exhibited "air hammer" characteristics of the hydrostatic load pistons and hydrostatic thrust bearings on first assembly. The air hammer was eliminated in each case by reducing the air pockets and increasing the supply pressures. Initial accelerations of the thrust bearing test rig were made without a

test bearing installed. Smooth operation was attained on the rig hydrostatic journal and thrust bearings up to 16,000 rpm; however, all attempts to drive through the first critical speed of approximately 20,000 rpm were met with violent vibration. The vibration was traced to contact between the shaft and carbon hydrostatic journal bearings. Attempts to detune the hydrostatic journals at the first critical were unsuccessful.

Initial instrumentation checkout of the thrust bearing test rig was made with a single oversized twelve pad foil thrust bearing and spring which had been designed for and proven on another application. Speeds were limited to 16,000 rpm in order to stay below the problems at the first critical speed. Following a successful checkout with the known bearing, a ten pad thrust bearing of the Mini-BRU design was installed and operated up to 16,000 rpm for comparative data.

Due to the problems associated with passing through the first critical speed on hydrostatic bearings, the decision was made to convert the test rigs to foil type journals while retaining the hydrostatic thrust bearing. Foil journal bearings were designed to support the test rig rotating groups. Following a brief development of these bearings, both rigs were converted to foil journal bearings. Initial checkout indicated that both rigs were capable of safe operation to 100,000 rpm. All subsequent testing operations on foil journals was without incident.

Test results. - As each test was concluded, the raw data was reviewed and plotted. In some cases, the data was reduced only to the extent of showing a trend or indicating a direction that should be taken in bearing development. The curves, shown in Figures 176 and 177, reflect the type of data reduction used in the test cell to quickly focus in on the best geometric designs. Figures 156 through 167 illustrate the more formal rigorous data reduction accomplished with the help of a computerized routine.

ALTERNATOR DEVELOPMENT

Alternator Electrical Design

Summary. - This section provides a complete description of the Mini-BRU alternator in its final design configuration. A detailed thermal summary is also included. Figure 178 is a photograph of the first unit, and Table XXV is a summary of salient data for the final machine.

Design selection. - The selected alternator is a four pole Rice machine designed for high efficiency over a wide range of load conditions. Optimum system speed was determined to be 52,000 rpm. Preliminary studies at 41,000, 52,000 and 60,000 rpm for two, four, six and eight pole alternator designs indicated that a four pole machine had the smallest, lightest rotor at each speed (refer to Table XXVI. Although total alternator weight was slightly less for six and eight poles, efficiency of these machines was reduced by higher windage losses caused by larger diameter rotors.

Since high efficiency rather than minimum weight was a design goal, the four pole machine was selected for further optimization and analysis. Practical considerations of fabrication also favored a four pole machine.

The analysis employed a computer design code based on conventional salient pole alternator theory. The model included the following routines:

(1) Pole and flux collector geometry, stator geometry

(2) Pole leakage

(3) Rotor windage loss

(4) End bell design and leakage

(5) Control and series field design

(6) Pole head loss

(7) Eddy factor for stator windings

(8) Apparent power factor, ac volts and amps, dc volts and amps, distortion factor, and rectifier losses for operation into a three phase, full wave load

(9) Iteration of stator turns to achieve specified commutation reactance

TABLE XXV. - ALTERNATOR DESIGN SUMMARY

TYPE:	FOUR POLE RICE GAS COOLED 3 PHASE "Y" CONNECTED 4 PARALLEL SHUNT FIELD COILS
DESIGN RATING:	2 KW_E, RECTIFIER LOAD 12.27 AMPS PER PHASE 65.90 VOLTS LINE TO NEUTRAL* 1733 HZ
MATERIALS:	ROTOR - HP 9-4-20/INCO 713 LC STACK - AL 4750, .006" LAMINATIONS FRAME & END BELLS - SAE 1018 FIELD & STATOR WINDINGS - COPPER
GEOMETRY:	24 SLOTS 2 PARALLEL CIRCUITS 5/6 COIL PITCH 2/3 ROTOR POLE PITCH 1.51" DIA ROTOR 0.020 AIR GAP 0.72" STACK WIDTH

*INTRINSIC VOLTAGE BEHIND X_{COM} IN RECTIFIED MODE.

TABLE XXVI. - MINI-BRU SPEED AND POLE STUDY

DATA DESIGN POINT: 2.169 KW, 66.24 VOLTS, 13.19 AMPS –0.8271 PF, X_L = 0.15 PU, Z_{BASE} = 5.02 OHMS								LOSSES – WATTS						
	SPEED RPM	FREQ Hz	N* %	N_e %	DROT INCHES	WTOT POUNDS	WROT POUNDS	STATOR COPPER	STACK	POLE HEAD	FIELD	STRAY	FRICTION & WINDAGE*	TOTAL
8 POLE	41,000	2733	86.36	90.10	1.9	7.060	1.828	46.25	81.76	8.97	97.61	3.81	104.0	342.5
	52,000	3467	84.25	89.68	1.8	5.937	1.532	40.22	101.1	8.50	94.7	5.02	156.0	405.5
	60,000	4000	82.84	88.96	1.7	5.433	1.406	36.39	125.2	7.58	92.67	5.66	179.2	446.8
6 POLE	41,000	2050	87.99	90.95	1.8	6.750	1.509	52.99	59.29	17.20	83.83	2.65	80.08	296.0
	52,000	2600	86.42	90.71	1.7	5.714	1.278	45.71	76.37	16.20	80.78	2.94	118.80	340.8
	60,000	3000	85.66	90.47	1.6	5.170	1.150	41.25	91.20	14.35	78.46	3.24	134.40	363.0
4 POLE DESIGN SELECTION	41,000	1367	88.41	90.67	1.7	7.090	1.280	64.09	41.04	45.59	71.00	1.40	61.18	284.3
	52,000	1733	87.51	90.78	1.6	5.977	1.079	55.33	52.50	42.48	68.33	1.57	89.35	309.5
	60,000	2000	87.26	90.89	1.5	5.366	0.956	50.05	61.96	37.30	66.35	1.76	99.29	316.7
2 POLE	41,000	683	87.83	90.77	1.8	11.03	1.451	96.52	27.02	56.93	39.05	0.98	80.0	300.5
	52,000	867	86.88	91.21	1.7	9.183	1.204	83.41	33.83	53.68	36.82	1.08	118.4	327.2
	60,000	1000	86.66	91.55	1.6	8.227	1.068	75.71	38.77	48.13	36.12	1.21	133.7	333.7

*INCLUDES WINDAGE LOSSES IN THE MAIN GAP AND 1/2 OF THE CONE SECTION

The operation of the alternator design program is such that the initial or "design" load condition synthesizes a basic geometry. Then, when subsequent load conditions are applied, performance is calculated using the initial basic geometry. The basic geometry can readily be changed either by changing the initial "design" load data or by changing initial design parameters such as pole flux density, winding reactance, or an air gap dimension.

The design program made it possible to rapidly compare many design variations while maintaining consistent values for flux densities, winding reactance, or geometric features as appropriate. Figure 179 shows the effect of different designs on efficiency at various load conditions. The 1.51 inch diameter rotor design was selected to meet the maximum output requirements and provide good efficiency at part load.

Field coil configuration. - For flexibility of operation, the field coil was comprised of four separate and equal toroidal coils, two on each side of the stack as can be seen in Figure 180. This allowed a variety of different hookups depending on the requirements. The configuration selected for test evaluation was a dual parallel arrangement where the two outboard coils were paralleled and the two inboard coils were paralleled. The internal wiring arrangement was such that this could be changed without a serious problem.

Figure 181 is a wiring diagram of the alternator with the shunt field excitation, an example of the arrangement available with the existing circuitry.

Rotor material magnetic Properties. - The alternator design is based upon magnetic properties of the HP9-4-20 rotor material at 500°F. This was defined during a previous program and is shown on Figure 182. Subsequent tests during this program, with material processed through a duplicate heat treat cycle, resulted in slightly lower magnetic characteristics; however, the properties at approximately 400°F, Figure 183 (H7A, 385°F) which is the maximum expected rotor temperature, are consistent with the 500°F data used for design.

During the development of the bimetallic rotor braze joining process, it was determined that a modification of the basic H7A heat treat was required. This modification was required because of braze joint cracking during the 1750°F soak portion of the thermal cycle.

To insure integral rotors, this high temperature soak was eliminated from the heat cycle resulting in a small compromise in magnetic properties. The magnetic characteristic of this

material is shown on Figure 184 with high temperature characteristics replotted on Figure 182. (The temperature description on the plots is an average temperature that approached 400°F at the maximum excitation.) The net effect of this is that the efficiency of the alternator with three capsules and this particular rotor should be reduced by approximately 0.5 percent.

Alternator Characteristics

Alternator Characteristic Curves and Parameters. - Significant electrical parameters of the alternator are listed in Table XXVII. These values are based on the design load case in which base alternator voltage is 65.9 V_{L-N}, base alternator current is 12.27 amps ac, and the frequency is 1733 Hertz. Since a rectifier load is specified, the subtransient reactance is a critical parameter for this application because it determines the apparent power factor of the load as a function of load current.

Excitation characteristics for short circuit, no-load, zero power factor and unity power factor are shown in Figures 185 and 186.

Figures 187 and 188 show the alternator vector diagrams for unity and -0.8217 power factors respectively.

Equivalent AC load. - Equivalent values for per unit voltage and power factor were determined and written into the computer math model to enable an ac simulation of the rectified load for the base and various off-load cases. Circuits (1) and (2) in Figure 189 plus equations A through D illustrate the method used in these calculations.

The actual computed values for these five cases in both ac and dc modes are listed in Tables XXVIII and XXIX.

Figure 190 is a graph of the excitation characteristic of the alternator with ac equivalent load at various load currents.

Magnetic data. - Figure 191 describes the magnetic circuit used in the alternator math model. An understanding of this circuit is necessary to interpret the magnetic data presented in Table XXX.

Tables XXVIII and XXIX presented magnetic circuit data for the initializing or design load case and for four different dc load conditions corresponding to the power available from 1/2, 1, 2 and 3 energy capsules.

TABLE XXVII. - ALTERNATOR PARAMETERS

REACTANCE & RESISTANCE, FIELD TIME CONSTANT

BASE IMPEDANCE	Z_{BASE}	5.371 OHM
RESISTANCES		
ARMATURE (@ 360°F)	R_A	0.0938 OHM
FIELD (@ 350°F) – 4 CONTROL FIELDS IN PARALLEL	R_{CF}	14.58 OHM
REACTANCES		
DIRECT AXIS SYNCHRONOUS	X_D	1.046 PER UNIT
QUADRATURE AXIS SYNCHRONOUS	X_Q	0.559 PER UNIT
ARMATURE LEAKAGE	X_L	0.153 PER UNIT
FIELD LEAKAGE	X_F	0.280 PER UNIT
ZERO SEQUENCE	X_0	0.066 PER UNIT
NEGATIVE SEQUENCE	X_2	0.197 PER UNIT
TRANSIENT, UNSATURATED	X_{DU}	0.433 PER UNIT
SUBTRANSIENT DIRECT*	$\approx X''_D$	0.381 PER UNIT
SUBTRANSIENT QUADRATURE*	$\approx X''_Q$	0.381 PER UNIT
FIELD TIME CONSTANT (HOT) SHORT CCT	TPD	0.0145 SECONDS
OPEN CCT	TPDO	0.0397 SECONDS

*ESTIMATED VALUE FOR RICE ROTOR WITH NO DAMPER CAGE

TABLE XXVIII. - EQUIVALENT AC LOAD CASES

VPU	APU	PF	KW_{AC}	Z_{AC} PU
0.9216	1.0	-0.8924	2.467	0.9216 /26.8°
0.9323	1.13	-0.8828	2.79	0.8251 /28.02°
0.8977	0.7760	-0.9102	1.902	1.1568 /24.47°
0.8473	0.3710	-0.9484	0.894	2.284 /18.49°
0.8225	0.1896	-0.9702	0.454	4.338 /14.03°

Per unit Voltage = 65.9 VAC
Per unit current = 12.27 AMPS
Per unit impedance = 5.371 Ω

TABLE XXIX. - APPARENT AC LOAD CASES

VPU	APU	PF	KW_{DC}	KW_{AC} Net
1.0	1.0	-0.8225	2.467	1.928
1.025	1.13	-0.8029	2.790	2.17
0.9530	0.7760	-0.8573	1.902	1.49
0.8670	0.3710	-0.9268	0.894	0.7
0.8300	0.1896	-0.9614	0.454	0.351

TABLE XXX. - MAGNETIC DATA

	½ CAPSULE			1 CAPSULE			2 CAPSULES			DESIGN			3 CAPSULES		
	KILOLINES PER POLE	KILOLINES PER IN.^{2}	MMF/POLE, AMP TURNS	KILOLINES PER POLE	KILOLINES PER IN.^{2}	MMF/POLE, AMP TURNS	KILOLINES PER POLE	KILOLINES PER IN.^{2}	MMF/POLE, AMP TURNS	KILOLINES PER POLE	KILOLINES PER IN.^{2}	MMF/POLE, AMP TURNS	KILOLINES PER POLE	KILOLINES PER IN.^{2}	MMF/POLE, AMP TURNS
MAIN GAP	20.9	34.6	221.7	21.9	36.3	232.3	24.2	40.1	257.1	25.6	42.3	271.2	26.3	43.5	279.0
TEETH		76.9	3.8		80.6	4.4		89.2	6.8		94.1	10.12		96.8	17.3
CORE		24.2	0.2		25.4	0.2		0.2	0.2		29.6	0.26		30.5	0.3
ARMATURE REACTION			16.0			44.7			128.3			179.9			210.8
POLE LEAKAGE	6.4			7.5			10.4			12.2			13.5		
POLES*	54.6	69.4	68.2	58.7	74.6	78.2	69.2	88.0	121.5	75.6	96.0	174.4	79.5	101.0	223.5
FLUX COLLECTOR*	54.6	71.2	22.7	58.7	76.5	25.8	69.2	90.3	41.0	75.6	98.5	69.9	79.5	103.6	92.5
COLLECTOR GAP*	54.6	16.6	103.7	58.7	17.8	111.5	69.2	21.0	131.5	75.6	22.9	143.5	79.5	24.1	150.9
FIELD LEAKAGE*															
UNDER COIL*	4.3			4.9			6.8			8.3			9.5		
THRU COIL*	4.6			5.2			7.2			8.9			10.3		
END BELL*															
BESIDE FIELD	63.5	54.8	3.8	68.8	59.4	4.1	83.2	71.8	6.0	92.7	80.0	7.9	99.3	85.7	10.6
BELOW FIELD	58.9	56.2	3.7	63.6	60.7	4.0	76.0	72.5	5.8	83.8	80.0	7.4	89.0	85.0	9.6
FRAME	63.5	54.8	8.7	68.8	59.4	9.4	83.2	71.8	13.6	92.7	80.0	17.9	99.3	85.7	24.1
TOTAL AMP TURNS/½ MACHINE			452.5			514.5			711.8			875.5			1019

*VALUES PER ½ MACHINE (NOT PER POLE) IN ACCORDANCE WITH MAGNETIC CIRCUIT

Alternator losses. - The design program was used to predict alternator losses for the five different power capsule cases with both ac and dc loads summarized in Tables XXXI and XXXII. The ac loads used in Table XXX are the equivalent loads described in the previous paragraph (Equivalent AC Load).

Motor start characteristics. - The alternator is capable of operation as a motor to accelerate the mini-BRU to self-sustaining rotational speed (approximately 50 percent of nominal design speed) when the gas inventory is at 70°F and 100 psia.

The performance characteristics of the alternator when operated as an induction motor are shown in Figure 192.

Magnetic unbalance characteristics. - The standstill forces that would be developed with the rotor magnetically displaced and the unit excited for rated load and short circuit conditions are given as negative spring rates in Table XXXIII. These forces were calculated using standard magnetic theory.

It has been demonstrated that the force is significantly reduced when the rotor is rotated. As reported in NASA CR-1452, the force is reduced by a factor of four in a homopolar inductor alternator. Tests with a Brayton Rotating Unit (BRU) four pole Rice alternator demonstrated significant reduction, in that excitation at standstill locked the rotor, whereas the same excitation at a few hundred rpm only slightly affected the rotor orbit. A mathematical model of the Rice machine was developed to evaluate the effects of rotation on unbalance forces in the auxiliary gap. The results of the analysis indicated that the force was reduced by a factor of two, maximum, at speeds greater than 7000 rpm. A similar reduction in main gap force is expected.

The effect of magnetic unbalance due to field excitation is minimized by inhibiting excitation until the machine has passed through the critical speeds and the gas bearing film is established.

Displacement will also result in magnetic unbalance forces during motor starts. Figure 193 shows the expected "negative spring rate" as a function of speed for a motor start with 0.003 inch displacement and using a fixed 31 v, 600 Hertz supply as required to provide worst case starting torque.

Construction materials. - The various materials used in the construction of the Mini-BRU alternator such as resins, adhesives and potting compounds are listed in Table XXXIV together with pertinent data.

TABLE XXXI. - ALTERNATOR LOSSES (AC LOAD)

Losses - KW	Load - KW/Power Factor				
	.367/-.970	.723/-.948	1.538/-.910	1.995/-.892	2.256/-.883
Electromagnetic					
Core	0.0103	0.0113	0.0138	0.0154	0.0163
Teeth	0.0177	0.0194	0.0238	0.0265	0.0280
Stator Copper	0.0015	0.0059	0.0256	0.0426	0.0543
Stray	0.0001	0.0003	0.0015	0.0025	0.0031
Pole Head	0.0152	0.0178	0.0266	0.0332	0.0375
Field	0.0111	0.0144	0.0275	0.0417	0.0563
Total EM Losses	0.0559	0.0691	0.1188	0.1619	0.1955
Windage	0.0225	0.0380	0.0687	0.0846	0.0933
Field Control	0.0100	0.0100	0.0100	0.0100	0.0100
Total Losses	0.0884	0.1171	0.4975	0.2565	0.2988
Efficiency - %					
EM	87.09	91.39	92.87	92.53	92.06
Alternator	82.78	87.25	89.20	89.05	88.70
Net AC	80.59	86.06	88.62	88.61	88.30

C-2

C-2

TABLE XXXII. - ALTERNATOR LOSSES - RECTIFIER LOAD

Losses - KW	Net DC Output Power				
	.351 KW	.700	1.491	1.928 KW	2.171
Electromagnetic					
Core	.0103	.0113	.0138	.0154	.0163
Teeth	.0177	.0194	.0238	.0265	.0280
Stator Copper	.0016	.0060	.0257	.0426	.0543
Stray	.0001	.0004	.0015	.0025	.0031
Pole Head	.0153	.0178	.0266	.0332	.0375
Field	.0111	.0144	.0275	.0417	.0564
Total EM Losses	.0560	.0692	.1190	.1619	.1956
Windage	.0225	.0380	.0687	.0846	.0933
Rectifier ($3.0 V_{FWD}$)	.0090	.0178	.0378	.0410	.0556
Regulator Losses					
Field Control	.0100	.0100	.0100	.0100	.0100
Total Losses	.0975	.1350	.2354	.3055	.3545
Efficiency - %					
EM[1]	86.85	91.32	92.83	92.09	91.96
Alternator[2]	82.50	87.16	89.13	88.61	88.56
Net DC[3]	78.26	83.83	86.36	86.32	85.96

1 $EM = 100 \times \frac{\text{Net DC + Rectifier + Control}}{\text{Net DC + (Losses-Windage)}}$

2 $\text{Alternator} = \frac{\text{Net DC + Rectifier + Control}}{\text{Net DC + Losses}} \times 100$

3 Net DC = 100 x Net DC/(Net DC + Losses)

TABLE XXXIII. - MAGNETIC UNBALANCE - ALTERNATOR OPERATION

STANDSTILL FORCE "SPRING RATE"[1]

LOCATION	1/2 CAPSULE	1 CAPSULE	2 CAPSULES	3 CAPSULES	MOTOR START 300 Hz 1.6 P.U. V/Hz
AUXILIARY GAP (EACH BEARING) LB/IN. OF DISPLACEMENT	616	712	992	1307	-
MAIN GAP LB/IN. OF DISPLACEMENT	963	1057	1295	1524	2695

[1]VALUES ARE IN THE DIRECTION OF MINIMUM AIR GAP.

EFFECT OF ROTATION: THE SPRING RATE WILL BE REDUCED BY A FACTOR OF 2 AT SPEEDS GREATER THAN 7000 RPM AND WILL BE DIRECTED AT AN ANGLE OF 24.5 DEGREES PRECEEDING THE MINIMUM AIR GAP.

TABLE XXXIV. - CONSTRUCTION MATERIAL USED IN MINI-BRU ALTERNATOR

Ident. No.	Application	Material Type	Identification	Manufacturer and Part No.	Temperature Data	Amount Used and Location Used
1	Adhesive	One component RTV Silicone	105-097-9001 RS184C01 MIL-A-46106	GE Silicone Products Division, Waterford, New York - RTV 108	450°F maximum operating temperature	Approximately 0.0017 lbs thermocouple bond 9 places field and stator
2	Adhesive	Nitrile-Phenolic	105-050-9001	Chemical Division Chrysler Corporation 5437 W. Jefferson Trenton, Michigan K-183 Cycle Weld	400°F operating temperature	0.0714 lbs lamination and damper ring bond
3	Adhesive	Epoxy one part	105-070-9001	Minnesota Mining and Manufacturing Company St. Paul, Minnesota Scotch Weld 2214	400°F maximum	Field to stator bond
4	Potting Compound	RTV silicone rubber	RS105E08 MIL-C-81306	Dow Corning Corporation, Midland, Michigan, 96-069 Class 08	400°F maximum	0.1833 lbs field and stator encapsulation
5	Varnish	Solventless silicone resin		Dow Corning Corporation, Midland, Michigan, R-4 3157	-85°F to 437°F	0.10361 lbs field wire coating
6	Tape	Polyimide film (Kapton)	722-022-9101	Connecticut Hard Rubber Company, New Haven Connecticut, Temp-R-Tape Kapton No. 850	400°F maximum	0.01005 lbs stator insulation
7	Tape	Nylon creped (Nomex Type 410)	722-015-9001 MIL-I-24204	Edgewater Paper Company, Hoosick Falls, New York	428°F maximum	0.020 lb field bobbin corner insulation
8	Lacing Tape	Polyimide (Nomex) Microcrystalline Fungicide wax	MIL-T-43435 Type V Fin B Size 3	E.I. DuPont DeNemours and Company, Inc.	400°F operating temperature	Stator winding trace
9	Insulation Wire	Polytetrafluoroethylene (PTFE)	S8936, S8937 MIL-W-168780		-130° to 482°F	0.0008 lb connecting wire insulation, stator and field
0	Insulation Sleeving	ML Polyimide Resin coated fiberglas	S9050 MIL-I-3190	Bentley-Harris Manufacturing Company Conshohocken, Pennsylvania, Ben-Har 963C	482°F maximum	Stator wire insulation trace
1	Insulation Sleeving	Fluorinated Ethylene Propylene	S9051	Brand-Rex Company Box 498 Willimantic, Connecticut	275° - 400°F operating temperature	Field and stator assembly trace
2	Encapsulation	Epoxy Resin	219-116-9001	Emerson & Cuming, Inc., Dielectric Mtl. Div. Canton, Mass. Stycast 2850 G.T.	400°F maximum	Stator end turn encapsulation
3	Insulation	Nomex-Kapton-Nomex	2045432-7	Eralock Company Van Nuys, Ca.	400°F continuous	Field Bobbin inside insulation and end turn bobbin insulation <1.0 oz.
4	Covering	Fiberglas Cloth resin coated	None	Western Fibross Glass Products Company San Francisco, Ca. EM-51	400°F continuous	Field coil covering <0.5 oz.

The behavior of these materials under the conditions expected during system operation are characterized in the section entitled, "Alternator Materials Offgassing."

Alternator Thermal Analysis

Introduction. - This section summarizes the results of thermal analyses conducted on the alternator. The analysis was performed to find the maximum steady-state temperatures within critical regions of the alternator during various operating conditions and to find transient temperatures during alternator shutdown and startup. The critical alternator regions include the stator windings, field coil windings, and foil-type thrust and journal bearings.

The analysis was basically in two parts; the first involved two alternator thermal models with different cooling gas flow arrangements. Each model was analyzed using input interface temperatures and heat fluxes defined by the hot end thermal analysis described in the section titled Thermal Analysis.

For the second part of the analysis, the alternator and the Mini-BRU hot end turbine model were combined. Two simplified overall thermal models evolved from this combination. One model was analyzed to confirm the baseline design alternator results previously obtained in part one of the analysis and to find transient startup temperatures. The second simplified model was used to investigate transient soakback during power shutdown.

Design requirements and conditions. - The thermal analysis was based on the data for Case I (low power) and Case IV (high power) conditions of the design requirements given in Table I.

The maximum temperature allowed for the alternator winding hot spots is 400°F during steady state. 450°F is recommended as the upper limit for winding hot spot during nonoperating soakback from the turbine. A journal bearing temperature up to 400°F is permitted during steady state, while 450°F is permitted during soakback to minimize degradation of material.

Computer program. - Four Mini-BRU alternator thermal models were developed for use with the steady state and transient thermal analyzer computer programs. All thermal models accounted for (1) conductance between physically contacting surfaces, (2) forced convection between alternator surfaces and fluid streams, (3) natural convection between alternator surfaces and static gas nodes, (4) radiation between internal surfaces that view each other and where significant radiation is expected, and (5) heat generation attributed to electrical current, stray losses, and bearing and windage losses. Radiation heat transfer from the alternator was not considered; however, it was taken into account in the turbine section during soakback and startup.

In addition to heat transfer calculations, the computer program determines the fluid stream pressure drop, which includes the effects of fluid friction, pumping effects due to rotational flow, and flow area change.

Thermal Models. - The basic Mini-BRU alternator thermal model is shown in Figures 193 and 194. The latter is a detailed representation of the end view of the stator connected to the side view of the end-winding elements. Heat generated within each stack-winding element and end-winding element is primarily removed by conduction through the backiron elements to the cylindrically shaped damper ring. Overall, alternator cooling is achieved by heat rejection to the He-Xe gas flowing through the heat exchanger surrounding the alternator stator and field coild (Nodes 72, 74, 95, and 97). The heat exchanger consists of 0.060-in.-wide fins machined in the alternator housing.

The nodes and heat fluxes used to define the interfaces common to the alternator model and the AiResearch of Arizona turbine model are those associated with 5, 64, 89, 91, 107, 140, and 141 in Figure 193.

The first thermal model has a flow distribution through three paths as shown in Figure 195. After leaving the compressor outlet passage, 97 percent of the gas enters the alternator heat exchanger. The remainder flows into the inlet cavity at Node 142 and then passes through the thrust bearing spacer, Node 81. The gas then splits, with 1 percent flowing through the compressor side (unloaded side) of the thrust bearing before returning to the compressor outlet. The remaining 2 percent goes to the turbine inlet after passing through the loaded side of the thrust bearing and the two journal bearings.

Model 2 corresponds to the final alternator design, and was developed after the data on the first model indicated that adequate cooling of the thrust bearing and compressor journal bearing could be achieved by heat conduction through the copper heat shunt, Node 126, to the compressor impeller. Subsequently,

forced convection cooling of these two bearings was eliminated and the adopted cooling scheme is shown in Figure 196. As noted, the entire gas flow from the compressor is through the alternator heat exchanger before it splits into two paths. The main flow (98 percent) leaves the alternator while the remaining 2 percent enters the alternator cavity, Node 202, through two 0.050-in. holes. This gas then passes through the turbine journal bearing prior to entering the turbine.

In addition to the revised flow arrangement other changes incorporated in Model 2 are:

(1) Blockage of 6 finned passages within the heat exchanger

(2) Increase in fin height from 0.20 to 0.22 in.

and copper field coil bobbin with aluminum

(4) Revision of the top insulator stick within the stator to eliminate the slot opening

Prior to the blockage there was a total of 78 passages in the heat exchanger. Six passages were blocked to obtain additional space for the alternator wires. To regain part of the loss in heat transfer surface area resulting from the blockage, the fin height (0.20 in.) was increased by 10 percent. The third and fourth changes above were made for ease of manufacturing and to reduce windage losses within the rotor-to-stator gap.

Model 3 is shown in Figures 197 and 198 and was used for an overall alternator-turbine steady-state analysis and startup analysis. This model consists of a simplified version of Model 2 added to the turbine model. Simplification was achieved by using fewer nodes in the thrust bearing, stator, and heat exchanger regions in order to maintain the computer calculation time at a minimum level. Model 3 uses 173 solid nodes and 9 fluid nodes as compared to 142 solid nodes and 14 fluid stream nodes in Model 2.

Model 4, which is used for soakback analysis, is a variation of Model 3 with changes made mainly in the reference node numbers for the fluid streams and in the initial conditions. For soakback during shutdown of the alternator and interfacing equipment, all previous fluid streams now become solid nodes subject to natural convection heat transfer. Cooling of the alternator is accomplished primarily by heat transfer to the turbine section, which in turn rejects its heat load to the ambient by radiation from insulated surfaces.

Thermal Analysis Results. - The steady-state temperatures for Models 1 and 2 are presented in Figures 199 through 206 for the high- and low-power conditions. The results show that the temperatures of critical parts such as the alternator windings and foil-type bearings are safely below their design limits (400°F for the windings and 500°F for the bearings). Since Model 2 represents the final alternator model, the thermal evaluation herein is focused primarily on the performance of this model at the high-power operating condition. In this case the data mainly in Figures 203 and 204 are of interest. The results show a maximum stator winding temperature of 369°F and a maximum field coil temperature of 286°F. At the low-power condition the corresponding maximum temperatures indicated in Figures 205 and 206 are lower and are 289°F and 269°F, respectively. Reviewing the alternator bearings, a maximum temperature of 417°F is noted for the turbine journal bearing. This bearing temperature increases to 446°F at the low-power condition as a result of the lower gas flow. This gas flow is 0.0014 lb/sec at low power as compared to 0.0070 lb/sec at the high-power condition. If Model 1 flow arrangement had been retained, Figures 199 and 201 show that the maximum turbine bearing temperature would have been about 445°F.

Further evaluation of the results for Model 2 disclosed that the equivalent of 90 to 100 watts of heat from the turbine is abosrbed by the alternator structure. Additionally, 230 watts are generated due to rotational windage and bearing losses and 191 watts are produced within the stator, field coil, and rotor as a result of electrical current and stray losses. Of the total heat in the alternator, about 83 percent will be rejected to the cooling gas leaving the heat exchanger. The remainder will be rejected to the compressor impeller by conduction and to the bleed gas leaving the turbine journal bearing.

Figures 207 and 208 illustrate the results for the overall alternator and turbine model (Model 3). The main purpose of this model was to check the interface temperatures of Model 2. Ideally, if the interfaces in Models 2 and 3 are correct, the alternator data in Figures 207 and 208 should be comparable with those obtained from the overall Mini-BRU model, which was analyzed independently from the alternator. The results are shown in Table XXXV for certain nodes of interest and reveal that Model 3 data compare more closely with Model 2 than with Mini-BRU data. Significant differences are are particularly noted with Nodes 82, 94, and 111. Node 94 is the shaft node near the turbine journal bearing. Nodes 82 and 111 are the interface nodes on the turbine side of the turbine curvic coupling and up to 83° difference is noted between the data for Model 3 and Mini-BRU model. Nodes 120 and higher are the turbine nodes and are included for reference only.

TABLE XXXV. - NODE TEMPERATURE COMPARISON FOR VARIOUS MODELS

Node (See Figures 5 and 6)	Node Temperatures, °F		
	From MINI-BRU Model	From Model 2 High-Power Mode	From Model 3 High-Power Mode
1	NA	385	397
6	365	367	373
30	NA	366	385
47	258	258	256
50	NA	243	246
59	NA	276	281
72	NA	347	371
82	510	583	593
94	454	424	508
108	290	250	250
111	502	600	572
120	1112	NA	1132
131	1278	NA	1142
134	NA	NA	1031
139	323	NA	333
140	524	NA	478
141	743	NA	763
144	1553	NA	1539
147	1377	NA	1378
152	1514	NA	1522
154	1543	NA	1555

NA: Not available

Exact reasons for the discrepancies are not known but they are believed to arise from differences between models as a consequence of simplification, differences in heat transfer parameters used in the various models, and differences in modeling of certain components such as the journal bearings.

Since there are more details in Model 2, it is believed that the results from the evaluation of this model are more representative of the final alternator configuration.

The heat exchanger pressure drop $\Delta P/P$ and windage and bearing losses for Models 1 and 2 are summarized in Table XXXVI. As noted, the $\Delta P/P$ value generally exceeds the allowable limit of 0.001. Deviation from this value was permitted for Model 2, as it appeared that a slight increase in system pressure drop could be safely tolerated. Deviation was also permitted in the magnitude of the total windage and bearing loss. At the high-power condition, the windage and bearing loss is acceptable; however, the allowable limit is exceeded when the alternator is operated at low power.

TABLE XXXVI. - PRESSURE DROP $\Delta P/P$ TOTAL WINDAGE AND BEARING LOSS

Item	Operating condition	Allowable value	Model 1 result	Model 2 result
Pressure drop $\Delta P/P$	Low-power	0.001	0.00107	0.00127
	High-power	0.001	0.00103	0.00107
Windage and bearing loss, kW	Low-power	0.111	0.142	0.148
	High-power	0.240	0.243	0.230

Table XXXVII and Figure 209 present the input interface data for Model 2. In the analysis the compressor impeller was held at 250°F, and the turbine hub was held at 600°F. Other temperatures held constant were those at Nodes 5, 64, 91, and 107. The heat absorbed from the turbine structure varied as a function of temperature, as shown in Figure 209. Table XXXVII also includes the expected and calculated heat fluxes corresponding to the interface temperatures. The expected values were predicted after alternator heat flux curves were superimposed upon similar curves for the turbine model. A review of Table XXXVI shows that calculated heat fluxes generally match the expected values. The

The largest difference exists with the heat flux from Node 3 to Node 5 in which the computed value is 4.1 watts as compared with an expected value of 7.0 watts.

TABLE XXXVII. - MODEL 2 HEAT FLUX COMPARISON

Interface node	Interface heat flux path	Node temperature, °F	Expected heat flux, watts	Model 2 calculated heat flux, watts
5	3 to 5	370	7.0	4.1
64	64 to 67	258	83.2	88.9
91	91 to 92	301	106.3	100.7
107	107 to 108	379	4.3	4.3
Low-Power Condition				
5	3 to 5	333	7.9	8.6
64	64 to 67	232	53.0	53.4
91	91 to 92	298	97.5	86.6
107	107 to 108	393	10.0	13.0

To predict the field coil temperature range in Model 2, a condition corresponding to two failed-open field coils (Nodes 72 and 95) was simulated. Here it was estimated that each of the remaining two field coils (Nodes 74 and 97) would generate heat four times higher than normal. The results for this condition are shown in Figures 210 and 211 at the high-power mode. Temperatures of 335° and 356°F are seen for Nodes 74 and 97, respectively. Under normal circumstances, temperatures of 259° and 278°F, respectively, (from Figure 203), are expected for the two nodes. In view of the simulated failure condition, the field coil temperatures still meet the thermal requirement.

The startup transient temperatures are shown in Figures 212 and 213, respectively, for various nodes within the alternator and turbine. The initial temperatures were assumed to be 80°F except for Node 108 (compressor impeller) and the fluid

stream nodes. Due to an oversight, Node 108 erroneously was held constant at 250°F. The fluid stream temperatures were held constant at the expected final steady-state values in order to facilitate the analysis. For reference these initial fluid stream temperatures are summarized in Table XXXVIII. In addition, it was assumed that the thermal conductances of the materials comprising the alternator were relatively constant; however, in the turbine section, the thermal conductances were allowed to vary as a function of the temperature since temperatures approaching 1600°F were expected. Once activated, the temperature of each metal node was allowed to increase as a function of its thermal capacitance and thermal conductance.

TABLE XXXVIII. - INPUT TEMPERATURE FOR STARTUP CONDITION

Fluid stream node	Input temperature, °F	Fluid stream node	Input temperature, °F
101	205	218	1434
102	214	213	1409
103	218	214	1390
159	244	215	1373
208	1600	216	1359
209	1600	217	1362
210	1600	218	1362
211	1456	--	--

Figures 214 and 215 present the soakback temperatures for selected nodes within the alternator and turbine. The soakback calculations were limited to 12 minutes because of the long computer time involved. The soakback uses the initial conditions obtained from the steady-state analysis of Model 3 and from a list of initial temperatures provided by the system transient analysis. A review of Figure 214 shows a maximum turbine journal-bearing (Node 92) temperature of 501°F. While the bearing temperature peaked at about 6 minutes of soakback time, the field coil (Node 60) temperature still continued to increase at the end of 12 minutes. To predict the maximum possible temperature for the field coil in addition to the stator coil, an equilibrium temperature analysis was performed based on the 12-minute

performance data. This analysis took into consideration all thermal capacitances and temperatures and yielded a final alternator-turbine equilibrium temperature of 449°F. The temperature is conservatively high since radiation heat losses from the external surfaces of the entire model were not involved.

Figure 215 applies to the turbine nodes and shows temperature decay rates between 20° and 35°F per minute. For those alternator nodes picking up heat, Figure 214 shows temperatures rising at a rate of 10° to 25°F per minute.

Conclusion. - The thermal analysis indicates that the current baseline alternator design corresponding to Model 2 satisfactorily meets the thermal requirements and guidelines imposed upon it for the steady-state and transient nodes. The thermal performance data for the baseline design are shown in Figures 204 and 205.

Although not necessary, heat transfer from the turbine journal bearing could be improved since it will be exposed to relatively high temperatures at all power levels. If design changes permit, additional cooling could be obtained by increasing the bleed flow from its present value of 2 percent of compressor outlet flow.

Alternator Thermal Analysis (Zero Cooling Flow)

Summary. - A followup thermal analysis was conducted on the Mini-Brayton Rotating Unit (Mini-BRU) alternator to determine steady state temperatures under zero cooling flow conditions. Only leakage flow through the thrust and journal bearings and operation at low power and high power levels were investigated. The results for cooling flow conditions were previously reported in Reference (30) for the low and high power conditions.

The analysis was based upon the thermal model depicted in Figures 216 and 217 which are similar to Figures 1 and 2 of Reference (30) with the exception of the fluid stream path. The leakage fluid path of interest for the analysis is from the outlet of the thrust bearing (Node 210), through the compressor journal bearing (Nodes 211 and 212), rotor gap (Node 214), and turbine journal bearing (Node 217).

Updated values of thermal conductivity for the rotor section, revised journal bearing surface areas, and the following input data were used in the analysis:

	Low Power	High Power
Alternator output power, net dc kW	0.35	2.162
Compressor outlet temperature, °R	584.5	658.3
Compressor outlet pressure, psia	20.5	106.1
Alternator pressure, psia	18.0	89.0
Compressor outlet flow rate, lb/sec	0.0701	0.35
Alternator leakage flow rate, lb/sec	0.00028	0.00105
Bearing and windage losses, kW	0.111	0.240
Rotational speed, rpm	52,000	52,000
Node 210 leakage gas temperature, °F	320	400
Turbine shaft temperature, °F	600	750

The thermal results are shown in Figures 218 and 219 for the low-power condition and Figures 220 and 221 for the high-power condition. The results indicate the winding hot spot is satisfactory at low power operation. However at high power operation, the winding hot spot temperature is excessive at 412°F as compared with an allowable temperature of 400°F.

For the journal bearing a temperature of 500°F is permitted. In the absence of cooling gas flow, the 500°F limit will be exceeded by 55°F at the high power condition and 15°F at the low power condition.

Other results of interest relative to interface junctions are tabulated below:

	Heat Flux, watts	
	Low Power	High Power
Nodes 107 to 108	9.0	3.41
Nodes 64 to 67	35.0	55.3
Nodes 91 to 92	80.2	88.3
Nodes 5 to 6	- 4.3	- 1.5
Nodes 94 to 92	9.0	14.2

Alternator Thermal Analysis (Bonded Stator Damper Ring)

Summary. - A thermal analysis was conducted on the Mini-BRU alternator to determine steady-state temperatures at the high power level for the design having the aluminum damper ring bonded to the stator back-iron laminations. Previously it was specified that the damper ring would be shrunk on the stator backiron. The latest manufacturing method now involves bonding of this damper ring to the backiron using Cycleweld K-183 adhesive manufactured by the Chrysler Corporation Checmial Division. The adhesive will fill a 0.002 inch gap between the ring and the backiron.

The high power input conditions for the analysis are the same as listed on pages 1 and 2 of Reference 30. The thermal models are shown in Figures 222 and 223 which are similar to Figures 1 and 2 in Reference 30.

Figures 224 and 225 depict the alternator and alternator stator temperatures. The results are satisfactory as indicated by a maximum stator winding temperature of 374°F and maximum field coil winding temperature of 286°F. For comparison the corresponding temperatures were 369°F and 286°F, respectively, for the original design where the damper ring is shrunk on the backiron. The maximum winding temperature permitted over any long period of operation is 400°F.

Alternator Electrical Testing

Introduction. - This section presents results of tests conducted on the Mini-BRU alternator component. The unit was subjected to performance mapping and motoring start evaluations and to operation in conjunction with a control module to determine response to system load changes and transients.

A comparison of predicted and measured alternator performance is given in Table XXXIX. Overall measured efficiency was slightly lower than predicted.

It was determined that steady load losses and core losses were higher than predicted. These could be reduced by the following design modifications:

(1) Change stator winding to provide more than two circuits per phase and change wire size from 24 to a smaller diameter. These changes would tend to reduce eddy currents generated in the core under load conditions.

(2) Change present AL4750 nickle-steel stator lamination material to grain-oriented nickle-steel or silicon steel.

TABLE XXXIX. - COMPARISON OF PREDICTED VS MEASURED PERFORMANCE

Parameter	Predicted value	Test value
AC efficiency	*87.40% at 1.9 kW, 0.892 PF	**84.5%
DC efficiency	*85.13% at 1.928 kW	**84.19%
Negative sequence X_2	***0.197 per unit	0.353 per unit
Field time constants		
(a) Short circuit	0.0145 seconds (350°F)	0.045 seconds (350°F)
(b) Open circuit	0.0397 seconds (350°F)	0.058 seconds (350°F)
Phase unbalance		
(a) Single phase		16.47% (L-N)
(b) Two phase		13.01% (L-N)

*Corrected for 93 watts friction of the rotor and gas bearings at atmospheric pressure.
**Corrected for copper loss of test wiring and operating temperature of alternator.
***One per unit impedance = 5.371 ohms.

(3) Add copper damper bars or plated copper strips to outer diameter of rotor to decrease pole face losses.

Test rig description. - The alternator unit was tested in an alternator simulator test rig. This configuration is shown in Figure 226. The alternator rotor was assembled with mass components simulating the turbine and compressor inertial characteristics for acceleration and deceleration evaluations. The rotor was driven by a laboratory air turbine. The cross section of the rig is shown in Drawing 3604680.

For purposes of efficiency evaluation, the unit was mounted in a pneumostatically floated housing such that the reactive torque could be measured from a strain gaged lever arm. The unit was driven by a separately mounted air turbine drive with a floating quill shaft connection. The cross-section of this test setup is shown in Drawing 3605310. A photograph is shown in Figure 227.

The overall test facility utilized for the alternator performance mapping is shown in Figure 228.

Alternator performance tests. - The specific alternator performance tests are listed in Table XL. All tests, where applicable, were conducted in accordance with MIL-STD-705.

Discussion of results. - The plotted results of the alternator performance mapping are shown in Figures 229 through 234.

Tests which measured dc ripple voltage utilized the setup in Figure 235 except a low-pass filter consisting of a 50 microhenry choke coil and two 25 microfarad capacitors in parallel were connected between the rectifier and load bank.

The photograph No. 10 in Figure 236 was taken with the oscilloscope connected at the rectifier with the filter choke bypassed. Photograph No. 11 was with the oscilloscope connected across the rectifier output and the filter choke in series with a 1955 watt load. Photograph No. 12 was taken on a dual channel oscilloscope with the filter choke connected in series with a 1955 watt dc load. One oscilloscope channel was connected at the rectifier output and the other channel was connected across the dc load.

The 10,398 Hz ripple voltage spikes with the filter connected measured approximately 9.9 v rms at the rectifier output, and nearly 0.8 v rms at the load, as indicated on the Photograph No. 12 shown in Figure 236. This represents an attenuation of 21.9 dB with a 50-microhenry choke and 50-microfarad capacitor low-pass filter. The attenuation required for the BIPS application is 22.5 dB at 10,398 Hz.

TABLE XL. - ALTERNATOR PERFORMANCE TESTS

Test	Procedure MIL-STD-705
Winding resistance	401.1
Thermocouple calibration	-
Insulation resistance	301.1
High potential	302.1
Ac no load saturation and torque	410.1a
Short circuit saturation and torque	411.1a
Rated ac load current and torque	413.1a
Unblanced loads	620.1 and 2a
Harmonic analysis	601.4a
Dc load current, commutation angle and torque	-
Friction, windage, and core loss	415.0, 3.2.1 415.0, 3.2.4
Stabilized dc load test	-
No-load flux test	-
Open-circuit time constant	430.1a
Short-circuit time constant	-
Phase sequence	507.1c
Negative sequence impedance	422.1a

Subsequent filter redesign based on this and other related test data with a digital control system has been accomplished. It is anticipated that the digitally controlled BIPS will utilize a two-stage low-pass filter having an inductance-capacitance (LC) product of 0.003 per stage. This should result in approximately 43 dB attenuation at 10,398 Hz.

The significance of the negative sequence reactance, X2, being nearly 1.8 times the predicted value indicates a wide variance from computed data. However, the X2 test value of 0.353 P.U. corresponds closely to the average reactance values predicted in the analysis for direct axis subtransient, X"D (0.381 P.U.) and quadrature subtransient reactance X"Q (0.381 P.U.). According to Reference 42, the permeance from which the negative sequence reactance is derived varies between the direct- and quadrature-axis values and negative-sequence reactance is usually taken to be equal to the average of the direct- and quadrature-axis subtransient reactances X"D and X"Q.

The X"D and X"Q values were not determined during this test phase, but typical values for synchronous machines vary from 0.2 to 0.5 per unit, the average being close to the test value of 0.353.

Short circuit and open circuit time constants of 0.050 and 0.092 second, respectively, were measured at temperatures of 81°F and 147°F, respectively. Correcting these time constants for change in field resistance expected at 350°F results in time constants of 0.045 second and 0.058 second, respectively. The field inductance should not change appreciably between the test temperature and the predicted operating temperature.

Using the relation between open circuit and closed circuit time constants given in Reference 43:

$$T'_{DO} = \frac{L_F}{R_F} = T'_D \frac{X_d}{X'_d} = (0.045)\ (\frac{0.59}{0.433}) = 0.061 \text{ second}$$

where:

T'_{DO} = direct-axis transient time constant

T'_D = direct-axis transient short circuit time constant

X_d = direct-axis synchronous reactance

X'_d = direct-axis transient reactance

The calculated open circuit time constant of 0.061 second compares favorably with the corrected test value of 0.058 second. For the above calculations, the direct axis synchronous reactance was determined from the family of saturation curves Figure 229 as the ratio of the no-load phase voltage on the air gap line to the short-circuit current produced by the same value of field current. Per-unit-value was obtained by dividing by base impedance of 5.371 ohms.

Direct-axis transient-reactance value of 0.433 P.U. was obtained from the design analysis.

A series of data plots showing the measured versus calculated performance is given in Figures 238 through 246.

Motoring performance tests. - Motoring tests were conducted to evaluate motor compatibility, starting performance with 400 Hz synchronous power input, ramped induction power input, voltage and speed regulation and locked rotor motor torque.

Tests conducted and results.

(1) Motoring compatibility characteristics with sine wave power source - The test rig was wired and instrumented as shown in Figure 247. A 400 Hz sine wave inverter was utilized for source power. The variable dc power supply was energized to provide the required alternator current to start the unit.

(2) Synchronous motor compatibility using square wave ramped frequency inverter - The unit was wired and instrumented as shown in Figure 248. The unit was started by activating the power supply and monitoring the data as the unit accelerated. A preset lead angle between inverter output and rotor pole position, which increased linearly with speed, was used during each start. Optimum lead angle was determined by making a series of starts with incremental variations in lead angle. Rotor pole position was determined by detecting the presence of a notched compressor vane whenever it passed the magnetic speed sensor. Optimum lead angle was approximately 35 degrees at 6000 rpm increasing to approximately 90 degrees at 23,500 rpm.

The start inverter design prevented acquisition of locked rotor motor data at a specified frequency. Therefore, locked rotor test data was obtained by energizing the alternator stator with low frequency square wave power from the invertor, and taking data before the shaft began to rotate. A breakaway torque of 2 inch-pounds was measured with a torque wrench prior to the actual start.

Windage and friction were determined from the Mini-BRU roll down charactertistics after start inverter power was removed.

No load hysteresis and eddy current losses were determined by subtracting windage, friction, and stator I^2R losses from the no load power input. Power input was measured at a steady-state speed of 23,538 rpm obtained with 27.2 volts dc input to the square wave inverter.

(3) Unit voltage regulation and speed control - The unit was wired and instrumented as shown in Figure 249. Data was recorded at rated power and at maximum power.

(4) No load hysteresis, eddy losses, function and windage - The unit was wired and instrumented as shown in Figure 250. The unit was energized with 500 Hz and operated until steady-state temperatures were attained in the alternator windings. The unit was then allowed to roll down so that inertia data versus rolldown time could be used to calculate friction and windage losses.

(5) Locked rotor test - The same test setup was used as in (4) above. The rotor was locked and 400 Hz square wave power was applied. A plot of locked rotor torque versus input current is shown in Figure 251.

Discussion of test results.

Motoring results. -The test results for the various motoring starts conducted with a 400-Hz input are shown in Table XLI. The most rapid start to 12,000 rpm synchronous speed using a 400-Hz aircraft alternator for input power was achieved with initial Mini-BRU field current of 0.5 ampere dc. Field current was removed 1.7 seconds after start initiation. Acceleration to 12,000 rpm occurred 2.3 seconds after power was applied and required an average of 0.99 kW total 3-phase input power. Maximum line current during the

start was 70.5 amperes and maximum line-to-neutral voltage was 27.5 volts rms. Pull-in to synchronous speed occurred at a rotor slip speed of 500 rpm.

The most rapid induction motor start was 3.9 seconds with 300 ohms connected across the Mini-BRU field coils in parallel with a damper diode. The average power required was 0.5 kW (1.95 kW-seconds), maximum line current was 67 amperes at 26 Vrms line-to-neutral.

Bearing friction breakaway torque was measured at 2.2 inch-pound. Maximum locked rotor torque measured with a torque wrench was 4.0 inch-pound at 5 times rated current and 0.5 ampere dc field excitation using 400 Hz, sine-wave input power.

A comparison of the best Mini-BRU motoring performance, obtained with a fixed frequency sine wave power source, versus that obtained with the square wave source operating in a ramped frequency synchronous mode is presented in Table XLII.

Overall efficiency was determined by calculating the energy expended (E_x) in accelerating the Mini-BRU rotor to 23,538 rpm divided by the energy input to the power source used for motoring the Mini-BRU alternator. Linear acceleration was assumed.

Speed regulation and voltage control. - Maximum voltage surges of minus 22, to plus 15, volts from the 120 volts steady-state value occurred when the 1306.8 watt user load was switched on and off. Recovery to steady-state voltage took less than 5 milliseconds. These values are well within the minus 65 to plus 90 volts surge, 50 millisecond recovery allowed by the design specification.

Maximum voltage ripple of 1.5 volts peak-to-peak (0.53 V_{rms}) at 1.2 kHz repetition rate, 0.3 volts peak-to-peak (0.106 V_{rms}) at 10.3 kHz was detected on the dual beam scope when operating with 1306.8 watts user load. These values are just outside the limits allowed by MIL-STD-704B; however, the ripple at 10.3 kHz is within the limit allowed by the design specification.

Voltage and speed regulation test results are shown in Table XLIII.

TABLE XLI. - MOTORING CHARACTERISTICS, 400 HZ

Run No.	Accel. Time to N_{sync} Sec	Max I/ϕ Amps	Max V_{L-N} Vrms	Avg. I/ϕ Amps	Avg. V_{L-N} Vrms	Avg. Start Kva	Avg. Start Kw	Avg. P.F. %	Avg. Kva Sec	Avg. Kw Sec	Max Torque In-lb	R_F Ohms	I_F Amps	N_{slip} at Pull-In Rpm	Remarks
1	2.3	70.5	27.5	57.5	20	3.43	0.99	28.8	7.9	2.3	2.0	--	0.5	500	Dc field current removed 1.7 sec after start initiation.
2	4.0	70.5	26.5	54.0	21	3.40	0.65	16.7	13.6	2.6	1.5	--	1.0	500	Dc field current removed 2.8 sec after start initiation.
3	4.0	74.0	28.0	56.3	21.3	3.59	0.70	19.5	14.4	2.8	1.8	--	1.5	600	Dc field current removed 2.6 sec after start initiation.
4	4.5	71.0	27.5	58.3	22.2	3.89	0.49	12.6	17.5	2.2	1.4	∝	0	900	
5	5.0	70.5	26.5	57.0	23.9	4.1	0.63	15.4	20.5	3.12	1.3	75	0.072*	1000	*Max. induced current during start
6	6.6	67.0	26.0	63.4	24.4	4.64	0.57	12.1	30.6	3.76	1.2	150	0.036*	1000	
7	3.9	67.0	26.0	60.8	23.2	4.23	0.50	11.9	16.5	1.95	1.2	300	0.018*	900	

TABLE XLII. - COMPARISON OF START MODES

Parameter	Start Mode		
	Sine Wave		
	400 Hz	800 Hz	Ramped Square Wave
Accel. time to 1200 rpm	2.3 sec	2.0 sec	7.2 sec
Accel. time to 23,538 rpm	--	3.4 sec	28.0 sec
Peak line current, rms	70.5	61.5 a	36.9 a
Peak L-L voltage, rms	47.63	44.0 v	16.3 v
Input KVA-sec to 12,000 rpm	7.9	3.0	3.01
Input KVA-sec to 23,538 rpm	--	6.7	5.41
Input KW-sec to 12,000 rpm	2.3	2.4	3.01
Input KW-sec to 23,538 rpm	--	3.24	5.41
400 Hz hysteresis and eddy current loss	40.57 watts	--	--
785 Hz hysteresis and eddy current loss	--	--	31.6 watts
Percent overall efficiency (for start to 23,538 rpm)	--	50.1	37.5

TABLE XLIII. - VOLTAGE AND SPEED REGULATION TEST RESULTS

Voltage regulation percent	Speed regulation percent	Total power watts	User load watts	Parasitic load watts
--	--	1080.0	0	1080.0
0.083	0	1320.0	520	800.0
0.17	0	1105.8	1081	24.8
0.25	0	1621.4	1300	321.4
0.56	0.1	2403.0	2125	278.0

The formulae used to determine voltage and speed regulation are:

$$\% \text{ Voltage Regulation} = \frac{\text{No Load Voltage} - \text{Full Load Voltage}}{\text{No Load Voltage}} \times 100$$

$$\% \text{ Speed Regulation} = \frac{\text{No Load Speed} - \text{Full Load Speed}}{\text{No Load Speed}} \times 100$$

ALTERNATOR ROTOR DEVELOPMENT

Introduction

A key task was the development of the bimetallic brazed alternator rotor. A four pole Rice alternator configuration was selected as described in the previous section. A visual model showing the complex shape of the rotor is seen in Figure 252. The brazed Mini-BRU rotor prior to machining is shown in Drawing 3604369 and the final configuration of the Mini-BRU rotor is shown in Drawing 3604336 and Figure 253. It comprises HP9-4-20 magnetic pole material, INCO-713LC magnetic separator material and is bonded with Palniro No. 7 gold base braze alloy.

Nine conical-shaped test specimens that were similar in weight and size to the Mini-BRU rotor were fabricated and bonded. There were ten magnetic configuration rotors fabricated. Severe cracking problems were encountered when test specimens were subjected to heat treat method H-7A as developed in the TAC program, Contract NAS3-15687.

Concurrent with the preliminary bonding development, the rotor shape was designed based on the maximum HP9-4-20 pole material magnetic properties heat treated to H-7A specifications.

Four new combinations of test specimen preparation, bonding, and heat treat were devised and all four methods produced successful bonds without cracking while retaining acceptable magnetic properties: (1) the magnetic rotor configuration specimen had a larger diameter than the final diameter and was heat treated with method H-7B (eliminated the reheat to the normalizing temperature), (2) the specimen was bonded to the susceptor (a cylindrical can used to more evenly distribute the heat); the susceptor and braze material were removed by machining, (3) the specimen was heat treated following the bonding without any cooling and reheating cycles, termed heat treat method H-7C, and (4) a more ductile material (INCO-625) was used for the magnetic separator material in conical test specimens--both heat treat cycle H-7B and H-7C were used. A procedure using shims as braze alloy dams was developed which enabled 90 percent match eloxed surfaces to be brazed.

Magnetic Properties

Numerous steels were evaluated for magnetic qualities and strength; several non-magnetic materials were evaluated. The final alternator design is based upon magnetic properties of the HP9-4-20 rotor material as defined from material in the H-7A heat treated condition during the NASA TAC program and shown in Figure 254 as the "Magnetic Data stored in Computer

Math Model for HP9-4-20, 500°F". The non-magnetic separator material selected was INCO-713LC. Also shown in Figure 254 is a test data curve that represents the magnetic properties of the Mini-BRU HP9-4-2 rotor at 196°C (385°F) [approximately the 204°C (400°F) design temperature] from a specimen heat treated to the final Mini-BRU NAS3-19517 heat treat specification (H-7C).

The small difference in the magnetic data from the TAC program (heat treat method H-7A) and from the Mini-BRU program (heat treat method H-7C) was due in part to insufficient procedural control during the original magnetic property determination. This was overcome through the utilization of controlled Rowland Ring test specimens for magnetic data acquisition. The remaining cause of the difference between the TAC and the Mini-BRU magnetic data is due to the difference in heat treat methods H-7A and H-7C. A later section describes the development of the rotor bonding and heat treat method and includes magnetic property data at room and Mini-BRU operating temperature for heat treat methods H-7A and H-7C and compares this data to the TAC data.

Rotor Design

The design of the alternator is reported in detail in the previous section. Since the rotor design was conducted in parallel with the development of the rotor bonding, heat treat, and the consequential changes of magnetic properties the alternator magnetic design was based on the previously known TAC magnetic data.

Note that operation of the Mini-BRU with the input heat corresponding to 1/2, 1, 2, or 3 heat source capsules of 2400 W_t (thermal watts) capacity and the design point are marked on the ordinate of Figure 254. This figure shows that the magnetic properties of the Mini-BRU rotor are better (+) or worse (-) than the computer math model by the percentages shown on Table XLIV. In the worst case (6.6 percent less β than the mathematical model for a three capsule heat source) the efficiency of the alternator will be reduced approximately 0.5 percent. This is not considered to be detrimental, since the alternator output power for the three-capsule configuration would only change from 2.162 net dc kW (using data from the mathematical model curve for HP9-4-20 magnetics) to 2.150 net dc kW.

Alternator Rotor Bonding and Heat Treat

The preliminary test specimens were of a conical joint configuration (Drawing PA3604144, referred to as conical test specimens in this report) with dimensions and component weight similar to the Mini-BRU rotor (referred to as magnetic configuration rotors. Nine conical test specimens were fabricated

TABLE XLIV. - VARIATION OF MINI-BRU TEST DATA FROM MATH MODEL DESIGN CURVE

Heat input	Mini-BRU test data Δ Percent β
1/2 Capsule (1200 W_t)	+9.9
1 Capsule (2400 W_t)	+3.4
2 Capsules (4800 W_t)	-3.6
Design point (6240 W_t)	-6.2
3 capsules (7200 W_t)	-6.6

and serialized 101 through 109. Ten magnetic rotor configurations were fabricated and serialized 112 through 121.

Temperature distribution determination. - Two conical test specimens (No. 101 and No. 103) were subjected to a series of four tests in the vacuum hot press facility (Figure 255) to determine (1) the optimum induction heating coil configuration, (2) the need for a susceptor (a cylindrical shell between the specimen and the induction coil), and (3) the optimum radial clearance between the induction coil and the susceptor specimen. The test specimens were subjected to a scheduled compressive force in an atmospheric pressure of no more than 0.013 Pa (0.1 microns of mercury) for the bonding operations and the temperature distribution determination. The eloxed mating surface of the pole material is shown in Figure 256.

For these first four tests, no braze alloy was used. The rotor simulator pole material used was HP9-4-20 and the nonmagnetic separator was INCO-713LC. The final test setup of the conical test specimen in the vacuum chamber (same for magnetic rotor configuration) is shown in Figure 257. The final induction coil and susceptor configurations and the thermocouple locations for the conical test specimens (same for the magnetic rotor configurations) are shown in Figure 258. The results of Test Runs 1 through 4 are:

(1) Test 1 (Specimen No. 101) - The induction coil had 9 evenly-spaced turns. Radial clearance with susceptor was 9.4 mm (0.37 in.). The temperature spread at bonding temperature [1052°C (1925°F)] was 167°C (300°F).

(2) Test 2 (Specimen No. 102) - The induction coil had 10 evenly-spaced turns. No susceptor was used and the clearance between the induction coil and the test specimen was 9.4 mm (0.37 in.). The temperature spread was 83°C (150°F) at bonding temperature.

(3) Test 3 (Specimen No. 103) - The induction coil had 10 evenly-spaced turns. The susceptor was again used and the clearance between the induction coil and the test specimen was 7.62 mm (0.30 in.). The temperature spread was 56°C (100°F) at bonding temperature.

(4) Test 4 (Specimen No. 103) - The induction coil had 11 evenly-spaced turns with the center coil spaced 22 mm (7/8 in.) from each end group of 5 evenly-spaced coils. The clearance between the susceptor and the induction coils was 6.4 mm (0.25 in.).

The temperature spread at bonding temperature was only 8°C (15°F). The excellent temperature spread determined that this heating configuration would be used for all further bonding processes. This is the configuration shown in Figures 255, 257, and 258.

Preliminary Bonding Method Tests, No Heat Treat

Four bonding method tests were conducted with conical test specimens. Brazing was accomplished with the induction coil and susceptor configuration of Test No. 4 to verify the bonding method using braze alloy foil of Palniro No. 7. The eloxed surfaces were gold plated prior to assembly. Figure 259 shows the parts of the conical specimen prior to assembly in the vacuum chamber. The machined and eloxed conical surfaces per Drawing PA-3604144 were checked for fit by the use of clay when loaded with a compressive force comparable to that used during the bonding operation. An average gap and braze alloy foil thickness of 0.05 mm (0.002 in.) was used. No machining of the joint fitup beyond the original machining was required. For those specimens that were tested on the tensile load machine, the maximum machine load limit of 711,715 N (160,000 lb) was reached without failure which gave a tensile stress at the gauge section of 620.5 MPa (96,000 psi). All specimens were machined to 40.4 mm (1.59 in.) per Drawing PA-3604144 (Figure 260). The results of these test runs (Runs 5-8) are as follows:

(1) Test 5 (Specimen No. 106) - Tensile check made at room temperature to limit of tensile machine. There was evidence of yielding of the INCO-713LC without separation of the specimen.

(2) Test 6 (Specimen No. 103) - No mechanical testing performed. Specimen sectioned for metallurgical examination (Figure 261). No cracking was observed.

(3) Test 7 (Specimen No. 102) - Tensile check made at room temperature to limit of tensile load machine. Again, there was evidence of yielding of the INCO-713LC without separation of the specimen.

(4) Test 8 (Specimen No. 104) - Tensile check made at 204°C (400°F) to limit of tensile load machine. Again, there was evidence of yielding of the INCO-713LC without separation of the specimen.

TABLE XLV. - MINI-BRU ALTERNATOR ROTOR BONDING AND HEAT TREAT CYCLES

	Heat treat cycle		
	H-7A	H-7B	H-7C
Braze Alternator per process specification EMS 52468 at 1052°C (1925°F)	X	X	X
Furnace cool to room temperature	X	X	
Heat to 954°C (1750°F), hold one hour (Normalizing heat treat temperature)	X		
Furnace cool to room temperature	X		
Furnace heat at 389°C (700°F) per hour	X	X	
Hold at 760°C (1400°F) for five hours (Austenitize heat treat temperature)	X	X	X
Furnace cool at 56°C (100°F) per hour to 649°C (1200°F), hold one hour	X	X	X
Air cool to room temperature	X	X	X
Soak at -196°C (-320°F) for four hours	X	X	X
Soak at 538°C (1000°F) for four hours	X	X	X
Soak at -196°C (-320°F) for four hours	X	X	X
Soak at 538°C (1000°F) for four hours	X	X	X

Heat Treat Method H-7A

Parts were brazed per the process specification at 1052°C (1925°F) and furnace cooled to room temperature, followed by heat treat method H-7A (Table XLV). In all cases, the brazed specimens were proof-tensile tested to the limit of the testing machine (as described for Tests 5-8) after bonding.

(1) Test 9 (Specimen No. 105) - The specimen was a conical type. After heat treat, cracking was noted in the braze filler and adjacent INCO-713LC after the austentize cycle (Figure 262). Specimen was pulled apart and showed approximately 50 percent of the braze area was thermally cracked (Figure 263) at the periphery.

(2) Test 10 (Specimen No. 107) - This specimen was also a conical type. In an effort to lessen the cracking at the periphery, the heat treat was conducted with a larger diameter than Test 9, but the tensile rupture test results were similar to Test 9.

(3) Test 11 (Specimen No. 112) - This specimen was of the magnetic configuration type as were those of all succeeding tests. The braze alloy was laid up using 4 layers of 0.0127 mm (0.0005 in.) foil. Figure 264 shows the components of magnetic test Specimen No. 112 prior to assembly into the vacuum chamber. The assembly of the rotor poles and non-magnetic separator with Palniro No. 7 braze alloy inserted is shown in Figure 265. After bonding, the specimen was machined to an interim diameter of 43.9 mm (1.73 in.), Figure 266, proof-tested as previously described, and heat treated (H-7A). The magnetic properties of the HP9-4-20 after the H-7A heat treat is compared to the data from the TAC program in Figure 267. The specimen exhibited a cracking problem after the normalize cycle as did the conical specimens. The cracks were uniform around the full length of the bond line, but unlike the conical specimens this magnetic configuration did not fail during the proof test. It was postulated that the mechanism of crack initiation and propagation was joint-configuration sensitive. After the H-7A heat treat cycle, the specimen was tension tested to 413.7 MPa (60,000 psi), an arbitrary stress which is approximately 5 times the rotor design stress.

Program Redirection

The cracking problem brought about a program redirection that culminated in four possible solutions to the problem. These solutions are outlined below in the results of Tests 12-16. There was no proof testing before or after the heat treatment.

(1) Test 12 (Specimen No. 113) - Heat treat process H-7B was used, which eliminates the normalizing cycle after the bonding and is reheated to the austenitize temperature (Table XLV). The specimen was machined to 43.7 mm (1.72 in.) diameter after bonding and prior to heat treat. After heat treat (H-7B), cracking was observed at the bonding surface as in Specimen No. 112. The specimen was machined down to 40.4 mm (1.59 in.) and no crack indications were present.

(2) Test 13 (Specimen No. 114) - The specimen was bonded to the susceptor at the center 76 mm (3 in.) during the bonding cycle with the brazing alloy and the bonding joint setup was the same as for Specimen No. 112. It was given an H-7B heat treatment and machined to 40.4 mm (1.59 in.). No crack indications were present.

This and all succeeding specimens were machined and eloxed in a batch of 10. They were machined and eloxed such that the limits of the pole dimensions were reached prior to obtaining a perfect fit for the loading operation. The resulting mismatch was much greater than the expected average of 0.05 mm (0.002 in.), resulting in braze alloy voids at the surface about 6.4 mm (0.25 in.) deep. This joint gap was in excess of 0.0635 mm (0.0025 in.) average, resulting in objectionable void formation. The void formation was determined to be caused by a capillary flow mechanism and not that of insufficient braze alloy or solidification shrinkage. After the H-7C combination bonding and heat treat cycle, the specimen was machined to 40.4 mm (1.59 in.), and no crack indications were present, but the lack of joint fill relegated this rotor specimen to use on the bearing test rig or the alternator test rig.

(3) Test 14 (Specimen No. 115) - This specimen was bonded in the same manner as Specimen No. 112 (Test 11) except that heat treat cycle H-7C was used, i.e., high temperature cooling and all reheating cycles

above the phase transformation temperature were eliminated completely. The heat treat steps after the 760°F (1400°F) hold are necessary primarily to obtain the required magnetic properties. Note that for the higher alternator power ratings, the magnetic properties of HP9-4-20 after heat treat H-7C are slightly less than those of the properties after the H-7A heat treat (Figure 268) and are up to 6.6 percent less than those from the TAC H-7A heat treat process. The later magnetic data was tested with the new improved test procedures.

(4) Test 15 (Specimen No. 108) - The non-magnetic separator material for this test was INCO-625, heat treated to the H-7B heat treat process. It was used in a conical test specimen configuration. The selection of INCO-625 was based on its improved ductility and lower yield strength as compared to INCO-713LC. This allowed yielding of the INCO-625 during the thermal heat treat process at stress levels below the yield strength of the bond interface, thus precluding failure at the bond interface. Metallographic examination of the surface and cross-sections through the bond interface indicated that the bond was free of cracks. The magnetic properties of the HP9-4-20 material were determined for the H-7B heat treat process from samples from this specimen.

(5) Test 16 (Specimen No. 109) - This was also a conical test configuration, but it was processed using the H-7C heat treat specification. Surface metallographic examination showed no cracks in this specimen. The magnetic properties of the HP9-4-20 material were determined for the H-7C heat treat process from samples from this specimen.

(6) Test 17 (Specimen No. 116) - This and all succeeding magnetic configuration rotors were bonded and heat treated with the H-7C heat treat process. Shims of non-magnetic material were used to form brazing alloy dams at the outer periphery of the specimen (Figure 269). The machined specimen showed no cracks and the voids were filled with braze material.

(7) Test 18 (Specimen No. 117) - This and all succeeding test specimens were sent back to be further eloxed in an attempt to obtain a better fit. This specimen was bonded without the use of shims, but braze voids were evident as described for Specimen No. 115 when the specimen was machined. This specimen was also assigned to lab test functions such as the bearing test rig or the alternator test rig.

(8) Tests 19-22 (Specimen Nos. 118-121) - These specimens were fitted with shims, brazed and heat treated (in the same manner as was Specimen No. 116). All showed good braze material fill after heat treatment (H-7C) and machining to 40.4 mm (1.59 in.). No cracking was evident.

Spin Testing

One alternator rotor was selected from the final fabricated electromagnetic configuration rotors. Rotor S/N 118 was modified to the whirl pit spin configuration and spun to 175 percent of rated engine speed of 52,000 rpm. No diametrial growth was evident. The specimen was then spun through 100,000 rpm without growth but the bimetallic braze separated at 114,000 rpm. Failure analysis indicated a braze joint overload including the fact that the large rotor diameter had been misplaced axially 0.5 inch during the machining process.

One additional rotor (S/N 113) was machined to the whirl pit configuration and the rotor spin test was repeated. Stress analysis of the rotor bimetallic joint indicated that 88,000 rpm would double the stresses at the normal operating speed of 52,000 rpm. The second spin test was checked at 75,000, 90,000, 100,000, 110,000, 120,000 and 130,000 rpm. No diametrical growth occurred at these speeds. The whirl pit driving motor failed at 134,400 rpm, indicating the limit of the whirl pit capability. The spin test was considered to have met the task requirements.

The remaining Mini-BRU alternator rotors were integrity checked at 88,000 rpm to verify the reliability of the delivery rotors. All rotors passed the overspeed test without growth. Engine rotors are considered acceptable if they exhibit a stress safety factor of 2 or more by proving their integrity at 88,000 rpm or higher.

Conclusions and Recommendations

Of the four candidate processes, the H-7C heat treat process using the INCO-713LC non-magnetic separator was selected. The basis for this selection was:

(1) Improved cost effectiveness due to simplified thermal processing and virtually no loss of magnetic properties.

(2) Improved technical soundness which was not attainable with previous heat treatments of larger specimens.

(3) It allowed the use of existing hardware.

For subsequent programs, it is recommended that INCO-625 be used as the non-magnetic separator to further reduce the technical risk. Improved machinability of the INCO-625 over that of INCO-713LC could be effective in further reduction of manufacturing costs provided the mechanical properties are not impaired. New designs should use magnetic property specifications that are approximately 90 percent of the maximum magnetic properties tested and published rather than 100 percent to ensure sufficient magnetic property margin during preliminary design.

ALTERNATOR MATERIALS OFFGASSING

Introduction

The use of the Mini-BRU in a Columbium metal system raised the fear that volatization of certain elements in the alternator core might have detrimental effects on those refractory materials.

The alternator core contained a number of organic compounds. These elements and their estimated weights are given in Table XXXIV.

A program was initiated with the Battelle Columbus Laboratories to investigate and characterize the nature and quantity of effluents from the stator and to determine a means of preconditioning the stators to minimize this effluent.

Test Summary

It was established that the low viscosity epoxide impregnant (material designation 5) and the epoxy resin (12) were responsible for the majority of outgassing which is likely to be encountered during operation of the Mini-BRU system. The recommended procedure for reducing the volatile level is a two-stage process. The first stage recommended is a vacuum bake-out at approximately 250°F for a time period of about 100 hours. This process removes excess curing agents and any monomers which might be present. Figure 270 is indicative of the behavior observed during this vacuum bake-out. The material removed during this processing was found to be pyromellitic acid from the epoxy. As can be seen from Figure 270, after about 100 hours a point of diminishing returns is met and a more rigorous bake-out procedure need be performed.

The second process recommended is a higher temperature bake-out in a helium atmosphere. For this bake-out test pressurized helium was employed. As a means of quantifying the organic release the helium output flowed into a flame ionization detector (FID) of a Varian chromatograph. The signal output from the FID then was monitored to supply the information on the kinetics of the release reaction. Initial release rates were very encouraging in that the loss rate decreased fairly rapidly with time. (See Figure 271.) This fairly rapid rate was due to the slight amount of pyromellitic acid remaining within the alternator stator. The release of pyromellitic acid was at a value near zero by 750 to 800 hours at 330°F, but it became obvious that another process was also operative and that this second process was now the rate-controlling process. This second process was definitely the decomposition of a silicone. A material buildup on the FID was observed after 800 hours of

testing. A mass spectral evaluation of a portion of the material indicated a mass of about 143. This may be a decomposition fragment from a larger molecule. It is believed that the actual disproportionation of the resin is being observed. This is a very low rate and would only accound for a few grams over the entire lifetime of the system. It would appear however, that this reaction level is the best that can be obtained at 330°F. In actual operation, of course, the materials are not at a temperature this high so the loss rate would even be lower. From some of the rate curves and activation energies one can see that a rate of about 2/3 this value would be a pessimistic upper limit. An additional factor is that of the silicone, 60/143 is nonreactive, since this is a silica (SiO_2) decomposition product which most likely will be entrained in the gas.

The hydrocarbon potential for reaction then is approximately 0.2g/year at the Mini-BRU operating temperature, providing the steps enumerated above are followed to reduce its outgassing to the lowest achievable level.

Test Background

In an attempt to determine the nature, magnitude and rates of offgassing of the components of the Mini-BRU Alternator a number of tests on individual components were completed. Such tests included differential scanning colorimetry, gas chromatography--mass spectrometry, and weight loss studies. Results of these tests were useful in determining which of the stator components were major contaminants at operating temperatures within the stator. Bake-out of the assembled alternator-stators with continuous monitoring of the total offgassing species enabled predictions of the amount of volatiles per year to be expected at an operating temperature of 330°F.

Fingerprint Experiments

The first screening test for individual stator components was a series of experiments utilizing a Perkin-Elmer differential scanning calorimeter (DSC). The DSC is capable of determining transitions in materials as well as establishing the onset of degradation reactions. All runs were performed in helium thus there was no atmospheric interaction in the rates. A sample run for material number 5 is shown in Figure 272. The materials of most concern were found to be material number 5, the low viscosity epoxide impregnant, and material number 12, the epoxy resin; their DSC curves are Figures 272 and 273, respectively.

Continued testing of alternator components supported calorimetry findings that materials 5 and 12 could be significant offgassing contributors. Short term kinetic experiments were

performed on all organic materials used in the alternator-stator. Samples were suspended from a fine wire and lowered into a vacuum chamber. Weight loss was measured using a Cahn RG microbalance. A temperature span from 200° to 400°F was covered. Three major contributors of volatiles were identified as materials 5, 8, and 12; a low viscosity epoxide impregnant, a polyimide microcrystalline fungicide wax, and an opoxy resin, respectively. Material number 10, ML polyimide resin coated fiberglass, was also considered a possible significant contributor. Material 8 could be especially serious considering the magnitude of weight loss in relatively small times. However the total quantity of both material 8 and material 10 is quite small and most likely both are volatilized out in preliminary vacuum bake-out of the alternator-stator. The total weight loss from material 12 was about 1 w/o after 4 hours at 300°F but the loss rate had decreased to a low value in that time period. Similar weight loss behavior was observed for material 5; however, the total loss was approximately two times greater. Rate data at 400°F for materials 5 and 12 are shown in Figure 274 and Figure 275 respectively. From kinetic data obtained at various temperatures the activation energy material Sample 12C was calculated as 3.9 Kcal. The activation energy for material 5, the low viscosity epoxide impregnant, was also determined to be 5.2 Kcal.

To further evaluate materials 5 and 12 experiments were conducted with the computerized gas chromatograph-mass spectrometer. One form of the output is shown in Figure 276. Here the amplitude of selected mass spectral peaks is shown as a function of spectrum number. This quantity, spectrum number, is the number of complete spectra taken by the mass spectrometer and stored by the computer. A complete spectrum is taken about every 4 seconds so this is really a time base. Temperatures are superimposed on the figure so that an idea of what is coming off at what temperature can be obtained. It is shown in Figure 276 that even below 300°F there is a strong loss of a large chain aliphatic hydrocarbon. The parent peak is likely m/e = 341. The fragmentation pattern indicates this material to be composed of just carbon and hydrogen and is shown in Figure 277. At higher temperatures there is a second reaction leading to a smaller hydrocarbon whose parent is likely m/e = 134. This spectra is shown in Figure 278. At the higher temperature likely we are witnessing a thermal decomposition which occurs at a threshold temperature of about 400°F.

A similar analysis applied to material 5 indicates that the decomposition products are for the most part unsaturated hydrocarbons with some additional oxidants such as carbon dioxide and water. The data indicate these oxidants are easily removed from the materials, thus the outgassing products appear to be essentially hydrocarbons.

In an effort to determine the effects of processing variables on outgassing rates, microbalance experiments were performed on three different batches of material 12. Results are shown in Figure 279. Materials were labeled in their order of receipt at Battelle for evaluation. Even in the fairly short duration runs it can be seen that there are significant differences not only in the magnitude but in the steady-state evolution rate from these three batches. It is believed that component material 12 is the most persistant cause of volatilization in the alternator.

Alternator Stator Bake-Out

Experiments with the initial alternator stator called for bake-out in flowing helium at 50 psig at 330°F with continuous monitoring of the effluent by a gas chromatograph. This system was not capable of handling the load of volatiles and a break occurred in the system in the splitter value assembly. The control thermocouple assembly became coated with an insulating layer giving rise to a large temperature excursion in the alternator-stator. The recorder was set to monitor only a short temperature span so it was not possible to determine the magnitude of the excursion but some later tests indicate it could have reached near 600°F.

It became apparent that some initial vacuum outgassing at a moderate temperature would be necessary to pre-condition the alternator. The test setup shown in Figure 280 was assembled to perform this preconditioning. A temperature of 250°F was selected. Figure 281 shows the pressure within the chamber as the pump down continued on the second alternator-stator. Three grams of condensibles remained in the LN trap after 80 hours of outgassing. This deposit was analyzed for composition by liquid chromatography and was identified as pyromellitic acid.

After the vacuum bake-out, the alternator-stator was placed in the flow apparatus; however, some changes were made to ensure that conditions which created problems during the first alternator outgassing did not reoccur. A schematic diagram of this flow apparatus is shown in Figure 282. The first change was the addition of a pressure-sensitive switch which would shut off the heater if the pressure exceeded a pre-set value. The second change was the positioning of the control thermocouple in the gap between the heater and the containment vessel--rather than within the vessel. The final change was a replacement of the silicon controlled rectifier thermal supply with a simple potentiostat which limited the absolute voltage the heater could draw. Likely these were not necessary after the vacuum pre-treatment reduced the load; however, they insured the integrity of the alternator-stator. The alternator-stator was outgassed in the flow apparatus for about

400 hours at 330°F prior to shipment to ORNL for further testing. Total quantities of outgassing products were continuously monitored with the Varian chromatograph. At the completion of this bake-out stage the magnitude of volatiles had decreased by more than three orders of magnitude.

The outgassing procedure for the third alternator-stator included the initial vacuum bake-out followed by bake-out in the flow apparatus. Preceding the preliminary vacuum bake-out, the assembly was evacuated for 96 hours. The assembly was then heated to 250°F and was baked out under vacuum for 105 hours. The alternator-stator was then cooled to room temperature and the bake-out system was connected to the flow apparatus. Again the liquid nitrogen trap contained a deposit of condensibles. The deposit was analyzed by liquid chromatography and was identified as pyromellitic acid plus about 10 percent silicone. The initial vacuum bake-out results for the third alternator-stator are shown in Figure 283. Bake-out in the flow apparatus was conducted at 330°F and 50 psig helium. After 700 hours the outgassing followed an almost constant bake-out rate. While the rate of release continued to decline, the decline was almost imperceptible after that time. The overall release rate of the alternator-stator changed from an initial rate of 3×10^{-7} g/sec to about 2×10^{-8} g/sec. At this rate the total quantity of volatiles in the BIPS system caused by the stator would amount to less than one-half gram per year of operation at 330°F. At an operating temperature of 300°F, the offgassing rate would be 1.1×10^{-8} g/sec based on a ratio of activation energies.

COLUMBIUM TURBINE PLENUM DEVELOPMENT

Design Analysis

Introduction. - A stress analysis was performed on the Mini-BRU turbine nozzle and plenum utilizing the refractory material, Columbium 103, as the material of construction. Various configurations were studied to reduce the stress levels in critical areas to an acceptable value for a ten-year continuous life. The analysis on the final configuration included the following:

(1) The turbine inlet duct plenum juncture for discontinuity stresses

(2) Detailed creep analysis at the nozzle vane to determine the stress redistribution at various stages of the service life

(3) A rigorous three-dimensional creep analysis on the plenum for hoop tension

(4) A creep analysis on the plenum at locations of high elastic bending stress

Conclusion. - Based on the calculated metal temperature and material data supplied by NASA, the turbine nozzle and plenum are satisfactory from a stress standpoint for a ten-year continuous life.

Recommendations. - The following recommendations are necessary to attain the 10-year life:

(1) The turbine nozzle and plenum should be fabricated from the same material, i.e., Cb-103.

(2) The material Cb-103 should be properly annealed to guarantee a one percent creep strength of 8800 psi at 1600°F and 100,000 hours.

(3) The plenum should be fabricated from 0.050 in. sheet stock.

(4) The shroud should be stiffened as shown in Figure 284.

(5) Quality should be carefully controlled in the area where the vanes are welded to the shroud to assure high integrity weld joints.

(6) The turbine inlet duct (of 0.060 in. thick material) should be butt welded to the plenum as shown in the lower half of Figure 9, Section 5C.

Approach. - The approach to the analyses includes the salient features as outlined:

Turbine Nozzle. -

(1) The analysis of elastic stress due to pressure and temperature was performed on the turbine nozzle and plenum assembly.

(2) The critical stress region was found to be the vane-shroud juncture.

(3) Various configurations were studied to reduce the critical stress, at the vane attachment, to acceptable values.

(4) The most effective configuration change for reducing the critical stress was found to be increasing the shroud stiffness.

(5) The critical stress in the vane renders that part vulnerable to creep relaxation.

(6) In order to establish that the creep relaxation occurring in other regions of the plenum did not significantly increase the loading across the vane, a number of hinges was inserted at various bending locations in the plenum for an elastic stress analysis.

(7) This analysis showed the possibility to analytically isolate the vane for a creep relaxation study.

(8) A detailed creep analysis was performed on the nozzle vane.

Turbine Plenum. -

(1) A rigorous creep analysis was performed on the plenum. The primary stress contribution is from hoop tension due to pressure loading.

(2) A rigorous creep analysis was performed on the plenum skin at the location of the highest bending stress.

(3) An analysis was performed on the inlet duct (plenum juncture) by using a series of elastic stress solutions to represent the stiffened cutout for the duct. These solutions yielded an approximate solution for the critical discontinuity stress around the hole. This stress was evaluated for creep relaxation.

Discussion. -

(1) Turbine Nozzle - Figure 284 shows the final configuration, metal temperature distribution, and pressure differential of the turbine nozzle and plenum assembly. The subject structure is designed for a ten-year continuous life. The high metal temperature and the long service life make creep the design criterion. Columbium 103 is a refractory material having low and near-uniform thermal expansion coefficients and adequate creep strength up to 1700°F. For these reasons, the material was chosen as the first material candidate. The final configuration, as shown in Figure 284, is the result of a series of stress analyses. It shows that the shroud, under the action of pressure and temperature, will rotate counterclockwise, causing tensile stress at the vane trailing edge (T.E.) and compressive stress at the vane leading edge (L.E.). Figure 285 shows the elastic stress level due to pressure and temperature using an 0.08 in. thick shroud. The maximum tensile stress at the vane T.E. is 16,000 psi, which is unsatisfactory from the standpoint of creep. This tensile stress can be reduced to an acceptable value by stiffening the shroud as shown in Figure 286. The maximum tensile stress at the vane T.E. was reduced to 7500 psi, which is less than the material's one percent creep strength at 1550°F and 100,000 hours of continuous operation. The elastic stress solutions for the stiffened and unstiffened shroud are for a plenum skin thickness of 0.04 in. Figure 287 shows the final configuration with the stiffened shroud and an 0.05 in. thick plenum skin. The increase in skin thickness from 0.04 in. to 0.05 in. does not significantly change the nozzle loading but is necessary for reasons discussed in subsequent sections of this report.

A detailed creep analysis of the final configuration of the vane was performed by using Program 871. This program does not have the capability to analyze the combined turbine nozzle and plenum for creep. Therefore, it is necessary to isolate the vane for creep analysis. Since the metal temperatures of the plenum skin are well into the creep range, the isolation of the vane for creep analysis is possible only when the creep deformation of plenum skin does not change the loadings across the vane significantly. This proved possible by inserting a number of hinges in the plenum skin at various critical bending stress points. Refer to Figure 287, Nodes 291, 303 and 342 for hinge locations. The results, as shown in Table XLVII, indicate there is no

significant change in stress level across the vane due to the insertion of hinges. In performing the creep analysis on the vane, the actual cross section of the vane was modeled as shown in Figure 288. The boundary condition loading was taken from the elastic stress solution and treated as a constant loading during the entire service life. Figure 289 shows the peak tensile stress at the vane T.E. was relaxed by 41 percent at the end of 100,000 hours.

As shown in Table XLVII, the tensile stress due to pressure at the vane T.E. is higher than that due to the combination of pressure and temperature. This is because the temperature effect rotates the vane assembly clockwise, reducing the counterclockwise rotation due to pressure only. The creep deformation at the vane T.E. after 100,000 hours, as shown in Figure 289, is 0.00027 in. which is considered conservative since it is due to pressure loading alone. Figure 290 shows the creep relaxation of the vane from the L.E. to the T.E. as a function of service life due to both pressure and thermal loading.

In order to gain an insight as to the relative stiffness of the shroud vs the relative stiffness of the shroud and vane assembly, an elastic stress analysis was performed on the nozzle-plenum assembly for zero bending restraint provided by the nozzles. Table XLVIII is a summary of this investigation which compares the axial deflections of the shroud for zero and full moment restraints of the nozzles, with and without hinges on the plenum skin, for pressure plus temperature, and pressure alone.

The table shows that the nozzles provide significant moment restraint to the shroud although the absolute deflections of the shroud are very small, i.e., 0.00023 in. vs 0.00074 in. for pressure loading. As previously noted, the analysis for hinges in the plenum skin does not significantly affect the vane loading. Table XLVIII shows that the hinges do not significantly affect the axial deflection of the shroud, but in fact produce slightly lower shroud axial deflection.

The creep relaxation investigation of the turbine nozzle-plenum assembly shows that the critically stressed region of the nozzle (T.E.) undergoes 0.1 percent creep, and the axial face clearance of the turbine increases 0.0003 in. over the 100,000-hour service life of the unit.

TABLE XLVII. - STRESS LEVEL AT THE VANE ATTACHMENT

Node	No Hinges in Plenum Skin		3 Hinges in Plenum Skin		Radius (inches)
	Pressure and Temperature	Pressure Only	Pressure and Temperature	Pressure Only	
487	-1,400	-1,800	-1,000	-1,400	1.876 L.E.
486	-1,700	-2,700	-1,900	-2,800	1.804
485	- 300	- 800	- 300	- 800	1.750
484	1,500	300	1,500	300	1.700
483	2,100	1,400	2,000	1,300	1.650
482	3,100	2,700	2,900	2,600	1.600
481	4,000	4,600	3,700	4,400	1.550
480	5,500	8,100	5,000	7,700	1.500
479	7,500	8,900	6,700	8,700	1.483 T.E.

NOTES: (1) See Figure 1 for node location
(2) All stress units in psi

TABLE XLVIII. - AXIAL DEFLECTION OF THE SHROUD

Condition	Node 385*		Node 455*	
	Pressure and Temperature	Pressure Only	Pressure and Temperature	Pressure Only
Full moment restraint No hinges	0.00101	0.00023	0.00172	0.00014
Zero moment restraint No hinges	0.00145	0.00074	0.00204	0.00048
Full moment restraint 3 hinges	0.00098	0.00021	0.00171	0.00014
Zero moment restraint 3 hinges	0.00139	0.00068	0.00201	0.00046

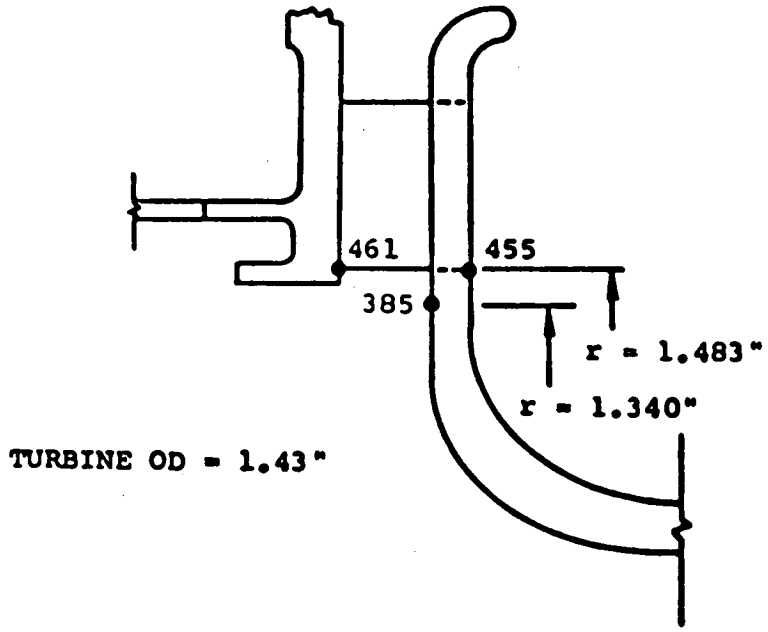

*Axial deflection w/t point "461"

(2) Turbine Plenum - A rigorous creep analysis was performed on the plenum with respect to hoop tension and axial loading. The one percent Larson-Miller curve, as shown in Figure 291, was first constructed based on creep data from NASA. The three-dimensional creep law was derived for 1500°F, 1550°F and 1700°F. The metal temperature of the plenum outer skin is 1550°F. Table XLIX shows the results of the creep investigation of the plenum skin, in hoop tension and after 100,000 hours, for two sheet thicknesses, 0.04 and 0.05 in. The change in thickness due to creep was negligible; however, the 0.04 in. skin undergoes 0.214 percent creep resulting in a diametral growth of 0.00994 in. whereas the 0.05 in. skin undergoes 0.013 percent creep resulting in a diametral growth of 0.00058 in. For the 1550°F temperature, Table XLIX also shows the sensitivity of the creep deformation to metal temperature. For example, the diametral growth of the 0.05 in. thick skin at 1700°F is 0.04 in. compared to 0.000108 in. at 1500°F.

The metal temperature of the maximum bending location is 1525°F (Node 291 in Figure 287). Another three-dimensional creep law was derived to calculate the creep strain at the section of maximum bending stress. The results are shown in Table L. The creep strains in axial, radial, and hoop directions after 100,000 hours are all less than 0.1 percent.

(3) Turbine Inlet Duct-Plenum Juncture - Two turbine inlet ducts are welded to the plenum skin at a 180 degree angular spacing. The ducts can be either butt welded or double fillet welded to the 0.05 in. sheet as shown in Figure 292. The duct-plenum juncture produces a stress concentration for the plenum hoop and axial loadings. The stress analysis of the juncture produces a stress concentration for the plenum hoop and axial loadings. The stress analysis of the juncture will consist of a series of elastic stress solutions. The initial analysis consists of a finite element solution of a simple cutout in the plenum skin. A separate model, as shown in Figure 293, was constructed by using Program BOSS 1 to evaluate the effect of the cutout on hoop tension. The result shows that the maximum stress is 12,667 psi, an increase of 260 percent from the nominal value of 4872 psi. The actual stress around the cutout will be lower than this value, as the juncture will provide additional stiffness. In order to compare the stress levels in the butt welded and double-fillet welded configurations, two models were used as shown in Figure 294. The junctures are treated as bodies of revolution around the centerline of the cutouts with

TABLE XLIX. - CREEP DEFORMATION AT MAXIMUM BENDING STRESS LOCATION (NODE 261) AFTER 100,000 HOURS

Temp (°F)	0.04 inch Plenum			0.05 inch plenum		
	ε_h^c	ΔR^c	Δt^c	ε_h^c	ΔR^c	Δt^c
1500	0.01%	+0.00023	-0.000004	0.00251%	+0.000054	-0.000001
1550	0.214%	+0.00497	-0.000081	0.013%	+0.00029	-0.000006
1700	3.2%	+0.0742	-0.0012	0.832%	+0.020	-0.0004

NOTES:

(1) The metal temperature at Node 261 is 1550°F.

(2) ε_h^c ... creep strain due to creep (in./in.)

ΔR^c ... radial deflection due to creep (in.)

Δt^c ... change in thickness due to creep (in.)

(3) + indicates increase
- indicates decrease

TABLE L. - CREEP DEFORMATION AT MAXIMUM BENDING STRESS

LOCATION (NODE 291) AFTER 100,000 HOURS

Temp (°F)	0.04 inch Plenum			0.05 inch Plenum		
	ε_R^c	ε_a^c	ε_h^c	ε_R^c	ε_a^c	ε_h^c
1525	2.45×10^{-5}	5.37×10^{-5}	2.95×10^{-5}	0.4×10^{-5}	1.0×10^{-5}	0.6×10^{-5}

NOTES:

(1) Metal temperature at the location of the maximum bending stress is 1525°F.

(2) ε_R^c ... creep strain in radial direction (in./in.)

ε_a^c ... creep strain in axial direction (in./in.)

ε_h^c ... creep strain in hoop direction (in./in.)

(3) See Figure 1 for node location.

an imposed axisymmetrical plenum skin loading. Finite element Program ISOPDQ was used to solve the problem. Figure 294 shows that the stress level in the butt welded configuration is slightly lower (2000 psi vs 2200 psi) than the double-fillet welded configuration. However, the maximum stress of the open-hole configuration is slightly less than double the maximum stress of the other two configurations. Since the two welded configurations showed no substantial differences in peak stress level, it is desirable to utilize the butt welded configuration as it is more efficient than a fillet weld joint. Comparing the stress levels in the butt welded configuration with the configuration without the juncture, it is seen that with an open hole, the stress level is approximately twice as much. Since the stress concentration of the open hole is approximately double the stress concentration of the butt welded configuration, the maximum stress calculated from the model shown in Figure 293 should be reduced by a factor of 1.88. However, the boundary condition loading applied to the models shown in Figure 294 is axisymmetrical.

In the actual plenum, the axial stress is only half the value of the hoop stress. As shown in Figure 295, the maximum stress for the case of uniform boundary condition loading is 30 percent lower than the maximum stress for the case when the boundary loading in the axial direction is half the value in the hoop direction. Therefore, the actual maximum stress in the plenum utilizing a 0.06 in. duct skin thickness, butt welded to the 0.05 in. plenum sheet, will be 2.6/1.88 x 1.3 = 1.80 times the nominal hoop stress of 4872 psi or 8780 psi. This stress level will result in a limited amount of creep relaxation over the service life of the plenum. However, the magnitude of the creep relaxation is not expected to approach the one percent creep deformation. Since the maximum stress extends over a very localized area, creep relaxation occurs and the loading is redistributed in the duct.

(4) Turbine Plenum Supporting Structure - The stress levels and metal temperatures are generally low in this region. The critical area is at Node 147 as shown in Figure 287, where the hoop tension is 7800 psi and the metal temperature is 1430°F. The material's 0.2 percent creep strength at 1430°F after 100,000 hours is estimated to be 9000 psi. No stress problem is anticipated in this region.

Results. - Results of the stress analyses are cataloged below:

Figure 214 shows the final configuration of the turbine nozzle and plenum.

Figure 285 shows the general elastic stress level with an unstiffened shroud and 0.04 in. thick plenum.

Figure 286 shows the general elastic stress level with stiffened shroud and 0.04 in. thick plenum.

Figure 287 shows the general elastic stress level with stiffened shroud and 0.05 in. thick upper plenum.

Figure 288 shows the vane cross-section used in the creep analysis.

Figure 289 shows the creep relaxation at the vane T.E.

Figure 290 shows the creep relaxation of the vane cross-section.

Figure 291 shows the one percent creep strength of Cb-103.

Figure 292 shows two configurations for the plenum-duct juncture.

Figure 293 shows the structure model for the plenum cutout.

Figure 294 shows the structural model for various cutout reinforcements under uniform boundary conditions.

Figure 295 shows the structural model of a flat plate with cutouts under different boundary conditions.

Table XLVII shows the stress level at the vane attachment under various conditions.

Table XLVIII shows the axial deflection of the shroud under various conditions.

Table XLIX shows the creep deformation of the outer plenum skin for various sheet thicknesses.

Table L shows the creep strains at the maximum bending location.

Examination of the Inlet Duct-Plenum Juncture Per ASME Unfired Boiler and Pressure Vessel Code

Summary - The Mini-BRU turbine inlet duct-plenum juncture design has been examined for conformance with the ASME Unfired Boiler and Pressure Vessel Code. This report documents the results of this study and compares it with the baseline analysis given above.

Conclusion - The recommended plenum skin thickness and duct-plenum juncture thickness as specified above satisfies the ASME Unfired Boiler and Pressure Vessel Code.

Discussion - The criteria used in the design of the inlet duct-plenum juncture was to provide a design of sufficiently low stress level to assure negligible creep deformation over the service life of the part. The final configuration is based on a very detailed stress analysis. The analysis shows that with 0.06 in. duct material butt welded to 0.05 in. plenum skin, the maximum local stress is 8780 psi. This stress level will result in a limited amount of creep relaxation over the service life of the plenum. However, the magnitude of the creep relaxation is not expected to approach the one percent creep strain since the maximum stress occurs over a localized area. Creep relaxation occurs and the loading is redistributed. Although the ASME Boiler and Pressure Vessel Code was not chosen as the design criteria for the duct juncture, the final configuration does satisfy the code. A comparison of the original analytic approach and the code requirement is shown below. It is noted that the boiler code does not provide analytic tools for rigorous stress analysis solution but rather provides design guideline by the use of simplified methods.

Plenum skin thickness, $t = 0.05$ in.

Inside diameter of duct, $d = 1.48$ in.

Duct thickness, $t_{np} = 0.06$ in.

Internal pressure, $p = 105$ psia

Working stress, $\sigma = 8900$ psi

(1 percent creep strength at 1550°F and 100,000 hours)

A. Per ASME Unfired Boiler and Pressure Vessel Code:

Required plenum skin thickness as defined in Par UG-37

$$t_r = \frac{Pr}{\sigma - 0.6p} = \frac{105 \times 2.32}{8900 - 0.6 \times 105} = 0.276 \text{ in.}$$

Required juncture thickness

$$t_{rn} = \frac{105 \times 0.74}{8900 - 0.6 \times 105} = 0.0088 \text{ in.}$$

Area of reinforcement required

$$A = dt_r = 1.48 \times 0.0276 = 0.0408 \text{ in.}^2$$

Area of reinforcement available

A_1 = larger of following

$= (E_1 t - T_r)d = (1 \times 0.05 - 0.0276)\ 1.48 = 0.0332 \text{ in.}^2$

or

$= (E_1 t - t_r)(t_n + t)2 = 0.0049 \text{ in.}^2$

A_2 = smaller of following

$= (t_n - t_{rn})5t = (0.06 - 0.0088)5 \times 0.05 = 0.0128 \text{ in.}^2$

$= (t_n - t_{rn})5t_n = 0.0154 \text{ in.}^2$

$A_4 = 2 \times 0.5 \times 0.05^2 = 0.0025 \text{ in.}^2$

Area provided by $A_1 + A_2 + A_4 = 0.0485 \text{ in.}^2 > A$

This is greater than the required area. More reinforcing element is not required, i.e., the recommended 0.06 in. juncture is sufficient.

$$\text{M.S.} = \frac{0.0485}{0.0408} - 1 = 0.19$$

B. Analytic approach as documented in the previous section:

Maximum hoop stress

$$\sigma_n = 8.780 \text{ psi}$$

1 percent creep strength at 1550°F and 10,000 hours is 8900 psi

$$\text{M.S.} = \frac{8900}{8780} - 1 = 0.0137$$

Although the duct-plenum juncture was not designed to meet the ASME Unfired Boiler and Pressure Vessel Code, the analytic results are in good agreement with the results per said code and is slightly conservative.

Effects of Mismatching of the Butt Weld Joints in the Mini-BRU Turbine Plenum

This analysis examines the effects of mismatching of the butt weld joints in the Mini-BRU turbine plenum and to determine the limits of such mismatch.

There are five butt weld joints in the turbine plenum; two in the circumferential direction at rear end; two axial weld joints and the plenum-duct juncture. The axial weld joint in the upper skin is the result of rolling 0.05 in. sheet metal into a cylinder. It carries the hoop tension due to pressure and is the most serious weld joint subject to mismatch.

A mathematical derivation of the surface stress increase due to mismatch, follows

For normal load P (hoop tension), Moment = Pe each side absorbs half moment

$$\sigma_{max} = \frac{P}{t}\left[1 + 3\left(\frac{e}{t}\right)\frac{1}{(1-\mu^2)}\right]$$

where μ is the poisson ratio.

The maximum hoop stress is 6300 psi occurring at the outer skin. The following table shows the relation between mismatch and the maximum bending stress.

Mismatch, e (inch)	Maximum Stress (psi)
0	6,300
0.002	7,130
0.005	8,377
0.006	8,792
0.008	9,623
0.010	10,454

The 1 percent creep strength of Cb-103 at 1600°F and 100,000 hours is 8,800 psi. Therefore, the maximum limit on the 0.05 in. sheet butt weld joint mismatch is 0.006 in. Since this increased stress is localized only along the weld, the magnitude of creep relaxation is not expected to approach the 1 percent creep deformation.

Refractory Turbine Plenum Fabrication

In April 1975, a subcontract was let to Fansteel Precision Sheet Metal to fabricate two C-103 turbine plenum/nozzle assemblies. The program consisted of the following tasks:

(1) Phase 1 - Joint Strength Evaluation

(2) Phase 2 - Configuration and Manufacturing Design Studies

(3) Phase 3 - Fabrication of Two Prototype Plenums

Phase 1 - Joint Strength Evaluation. - The objective of Phase 1 was to develop the weld or brazing joining techniques required to fabricate the plenum. In addition, tensile and stress rupture data were to be obtained for the joint configurations. A key element was the development of a bimetallic joining technique so that the C-103 plenum could be weld joined to the housing of the unit.

A test matrix, shown in Table L1, was developed to define the various combinations of materials and techniques to be

TABLE LI

Test Sample Identification (Material and Joining Method)

Test No.	Material	Weld Method	Joint
1	Cb to Cb	GTAW	Burn Down Flange
2	Cb to Cb	E.B.	Butt
3	Cb to 347 Cres	E.B.	Butt
4	Cb to Titanium	E.B.	Butt
5	Cb to 347 Cres	GTAW	Burn Down Flange
6	Cb to 347 Cres	E.B.	Butt
7	Cb to 347 Cres	Resistance	Lap
8	Cb to Titanium	GTAW	Butt
9	Cb to Titanium	E.B.	Butt
10	Cb to Titanium	Resistance	Lap
11	Cb to 347 Cres	Resistance Braze	Lap
12	Cb to 347 Cres	Resistance Braze	Lap
13	Cb to Cb	E.B.	Lap
14	Cb to 347 Cres	Explosive	Lap
15	Cb to Cb	GTAW	Burn-Down Flange

evaluated. Gas tungsten arc (GTA), electron beam (EB) and resistance welds were to be evaluated for C-103 to C-103, C-103 to CRES 347 and C-103 to Ti-6Al-4V joints. As the program progressed, a resistance braze technique was evolved and added to the list of candidates.

Test samples were fabricated by Fansteel and subjected to the tests shown in Table LII.

Columbium to columbium and columbium to titanium GTAW and EBW joints exhibited excellent strength and ductility at room temperature and at 500°F. The columbium to columbium EBW joints averaged 1.1 percent creep elongation in 1-in. gauge length at 1800°F with a 12 kpsi load.

Resistance seam welded joints in columbium to titanium exhibited good strength and ductility. Resistance welded joints in columbium to stainless were brittle at room temperature but were fairly ductile at elevated temperature. Their strengths were marginally low at room and elevated temperature.

A diffusion experiment at 800°F for 500 hours indicated no deleterious effects on joint strength nor ductility.

Fusion welded joints between columbium and stainless steel type 347 cracked during welding and were not physically tested.

From the work performed in Phase 1, the following conclusions were drawn:

(1) Columbium to columbium joints welded by the GTAW and EBW processes produce high strength joints exhibiting acceptable elongation and bend ductility. Creep elongation at 1800°F with a 12 kpsi load for 100 hours is 1.1 percent in 1-in. gauge length.

(2) Columbium to titanium joints welded by the GTAW, EBW, and resistance seam weld processes produce consistently strong, ductile joints.

(3) Columbium to stainless steel type 347 can be joined by resistance welding but the joints are brittle and weak. This system is not recommended for joints subject to thermal cycling nor joints requiring a pressurized gas tight seal. Fusion welded joints are so brittle, they crack during welding and are not structurally sound.

During the period of Phase 1, the extensive stress analyses were continued to both integrate the results of and guide format for the Fansteel tests.

TABLE LII. - QUALITATIVE TESTING REQUIREMENTS

Material Combination	Welding Method	Qty	Tensile R.T.	500°F	1800°F	Stress Rupture 1800°F/ 100 Hrs.	Bend	Metallographic Evaluation
Cb-103 - Cb-103	GTA	13	3		3	3	3	1
	EB	13	3		3	3	3	1
Cb-103 to Stainless Steel	EB	10	3	3			3	1
	GTA	10	3	3			3	1
	Resistance	10	3	3			3	1
Cb-103 to Ti-6Al-4V	EB	10	3	3			3	1
	GTA	10	3	3			3	1
	Resistance	10	3	3			3	1
*Cb-103- Stainless Steel	GTA	9	3	2			3	1

*These specimens only, prior to testing, shall be exposed to a vacuum of sufficient degree for not less than 500 hours at a minimum temperature of 800°F

Phase 2 - Configuration and Manufacturing Design Studies

This comprised an extension of the work completed in Phase 1 relative to performing joining evaluations on samples more nearly representing the actual configuration of the plenum. The following full size specimens were fabricated and inspected.

(1) Nozzle vane samples were fabricated by EWX machining the male and female members to obtain a pressure fit. Figure 296 shows a sample vane. Three of these samples were welded to various depths of penetration as shown in Figure 297. Subsequent analysis showed that crack-free welds could be obtained with adequate depth of penetration to meet the required strength.

(2) A full size nozzle ring as shown in Figure 298 was then fabricated, assembled, Figure 299, and welded as seen in Figure 300. Slightly more shrinkage occurred across the nozzle throat than was anticipated. Figures 301 and 302 show views looking at the interior and exterior of the nozzle area. A flow check revealed the nozzle to be about 7 percent undersize. Subsequent nozzles will be shimmed to a wider gap during welding.

(3) Further development of the resistance braze bimetallic joining technique was completed. The joints tested at 500°F were approximately 70 percent of the joint tensile shear tested at room temperature.

(4) A full size ring specimen comprising a C-103 to 347 CRES joint was resistance brazed with a Palniro strip between was successfully completed. This sample passed 500 psi pressure test and helium leak test evaluation.

(5) Additional C-103 electron beam welded lap joints were tested. Specimens endured 100 hours at 1800°F with a 12,000 psi load, with 0.9 percent average elongation.

From these results the following conclusions were drawn.

Resistance brazing of C-103 to 347 with Pal-Ni braze foil produced high quality joints with acceptable strengths at room temperature and 45,400 psi ultimate tensile shear strength with 16 percent average elongation at 500°F NDE examination

indicated no discontinuities and no through-joint leakage with the helium mass spectrometer technique.

The electron beam double weld lap joint produced high physical strength and good endurance at 1800°F in vacuum.

Edge welding of the vane to shroud by GTAW in an argon atmosphere weld chamber produced maximum joint thickness with full melt-down of the 0.060-in. weld projection. The degree of shrinkage falls well within the dimensional tolerances of the vane-shroud subassembly.

The plenum nozzle can be fabricated using the current design with the joining methods tested and reported herein.

Fabrication of two prototype plenums. - Based on the results of the Phase 1 and Phase 2 test program and the requirements of the AIRPHX stress analysis, a final configuration was achieved for the plenum. This is shown in Drawing 3604356.

Fabrication of the plenum was initiated upon receipt of the required C-103 material at Fansteel in August 1976.

The inlet nozzle plate was machined and submitted for nozzle area inspection. The nozzle area was calculated by measuring and summing the dimensions of each passage and by measuring the airflow through the nozzle. The results of this analysis are shown in Table LIII. Both nozzles indicated throat areas slightly lower than design, but within acceptable tolerance limits.

Of the two methods of measurement the dimensional method is judged the more accurate. The flow measurement is subject to deviations due to test conditions and swirl effects due to the direction of airflow.

The plenum outer skin was fabricated by deep drawing a C-103 sheet then swaging the ports for the inlet ducts. This subcomponent is shown in Figure 303.

Some minor weld problems were experienced during the fabrication. These problems were primarily with porosity in the welds. Fortunately, in all but one case the porosity occurred in low stressed areas where it could be tolerated.

One problem, however, occurred in the weld where the inlet duct is joined to the swaged plenum ports. This porosity was repaired by grinding out the affected area to expose the pore and then rewelding to repair the area.

TABLE LIII. - PLENUM NOZZLE COMPARISON

Nozzle S/N	Design Area	Dimensional Measured Area	Deviation From Design	Flow Measured Area	Deviation From Design
01	0.242	0.234	-3.3%	0.226	-6.6%
02	0.242	0.236	-2.5%	0.231	-4.5%

One of the completed C-103 plenums is shown in the two views of Figure 304 and Figure 305. Unfortunately, a decision was implemented on the BIPS program wherein a superalloy system was to be the initial test bed. The C-103 plenums were not used and remain on standby until a C-103 system is constructed.

THERMAL ANALYSIS

Introduction

The cooling scheme for the Mini-BRU is simple; it features (a) conduction of waste heat to the main flow path from the bearings and alternator, (b) bleed flow to augment turbine bearing cooling and to intercept heat transfer from the turbine wheel, and (c) insulation to minimize heat transfer from the turbine inlet structure. No shaft seals are used in the unit as the foil journal bearings serve this function.

Specified temperature limits,were found by analysis to be satisfied, with one qualification. Teflon coated foils in the turbine bearing would have marginal temperatures at low power levels (less than 2400 W_t heat source).

Conclusions and Recommendations

(1) The design concepts used for thermal management are simple, efficient, and satisfy the thermal requirements according to analysis.

(2) With the heat source smaller than one 2400 W_t module, such that the power output is less than 0.65 kW_e and compressor discharge pressure less than 33 psia, the turbine-end bearing foil temperature peak could exceed the specified steady state limit of 400°F applicable to Teflon coatings.

(3) Analytical uncertainties are highest in predicting metal temperatures in the hot turbine static structure.

(4) Bearing foils should be instrumented to verify the modeling procedure used to predict metal temperatures thereof.

(5) Cavity pressures and main flow pressures should be measured throughout the unit since this will provide the only means of evaluating cooling flow rates.

(6) Dimensional tolerances are critical on a few elements of the cooling system; the bleed gas metering orifices, the bore surfaces of the journal bearing carriers, and the fit of the copper sleeve inside the thrust runner and compressor wheel.

Thermal Requirements and Design Concepts

The primary thermal requirement which must be satisfied by the rotating unit design is that material temperature limits are not exceeded. This is a broad requirement which can be specified as follows:

(1) Temperature levels shall not reach those which would produce significant and permanent degradation of functional material properties within the time of exposure.

(2) Steady state temperature levels in high steady stress locations shall not reach those which would produce stress-rupture or one percent creep in the design life of 10 years.

(3) Temperature levels and/or gradients shall not reach those which would produce low-cycle-fatigue cracks in 1000 cycles of operation.

These must be satisfied by some combination of materials selection, mechanical design, and thermal management. The secondary thermal requirement is to minimize power system losses, which can be specified as follows:

(1) Where temprature control is needed to satisfy material temperature limits, it shall be done with minimum performance loss as first priority.

(2) The external insulation system shall be designed with minimum heat loss as first priority.

Materials exposed to hot gases in the turbine section are not considered temperature controllable although cooled turbine technology is available. To do so would penalize performance, cost, and reliability. Thus, items (1) through (3) were satisfied by materials selection and mechanical design in the turbine.

The rotating unit is completely self-cooled, i.e., no external heat sink is provided. All heat generated in the unit by electromagnetic and frictional processes and all heat transfer from the turbine section are ultimately rejected to the cycle gas. The principal elements of the internal cooling system are:

(1) An annular heat exchanger around and integral with the alternator frame, through which the compressor discharge flow passes. It handles the bulk of heat

rejection, absorbing all heat generated in the alternator and all heat transferred from the turbine static structure. Part of the frictional heat generated in the bearings also is conducted through the alternator end-bells and into this heat exchanger.

(2) A copper heat shunt within the rotor connecting the thrust bearing rotor to the compressor impeller. A large part of the thrust bearing frictional heat is thereby conducted into the steel impeller and convected from the hub surface into the cycle gas being compressed.

(3) Bleed flow (2 percent of cycle flow) from the downstream end of the alternator heat exchanger--it is metered, passes through the alternator cavity and the turbine-end journal bearing and returns to the cycle by passing over the turbine shaft and wheel backface to the rim of the wheel. It absorbs some of the frictional heat in the journal bearing and intercepts heat transfer from the turbine wheel. It is most effective at the higher power levels.

(4) Thermal isolation between the hot turbine nozzle and its mounting flange. Use of thin-shelled, Z-shaped structure with a fully multi-foil insulated exterior minimizes turbine heat loss and protects the alternator and the O-ring seal used in the mounting flange (O-ring is absent in a hermetically sealed unit).

The temperature limits listed below have been specified or considered acceptable under thermal requirement (1):

Organic O-ring seals	400°F steady state 450°F maximum
Teflon-coated bearing foils	400°F steady state 450°F maximum
Alternator stator/field windings	400°F steady state 450°F maximum
Alternator rotor (HP 9-4-20)	475°F steady state

Operating and Boundary Conditions

Two operating conditions have been analyzed; these represent the extremes of the output power range. During the analysis, no reasons were found to analyze intermediate power levels as temperatures throughout the unit are expected to vary monotonically with power level. The following cycle conditions for HeXe gas (MW = 83.8) were used in the analysis:

	High Power	Low Power
Net Output, kW	2.162 (3 heat source capsules)	0.350 (1/2 heat source capsule)
Compressor flow, lbm/sec	0.357	0.0715
Compressor inlet, °F/psia	74/70.6	-2/12.8
Compressor discharge, °F/psia	198/105.82	125/20.446
Alternator HX discharge, °F/psia	218/105.7	183/20.42
Turbine inlet, °F/psia	1600/105.0	1600/20.2
Turbine discharge, °F/psia	1336/71.6	1326/13.2

Aerodynamic conditions, internal heat generation, and bleed flows are:

	High Power	Low Power
Compressor impeller rim static, psia	91.05	18.30
Turbine wheel rim static, psia	88.62	16.592
Journal bearing friction, watts/bearing	38	32
Thrust bearing friction + windage, watts	96	59
Alternator windage, watts	93.3	22.5
Total EM losses, watts	195.6	56.0
Rotor speed, rpm	52,000	52,000
Bleed flow, percent	2.06	2.0

Terrestrial operation (one-g) was assumed with a vertical, turbine-end up, attitude. This is reflected in the bearing loss values above and in the calculation of free-convection heat transfer coefficients, both internal and external. External boundary values used on a turbine insulation system were invariant, ranging from 1.35 to 3.16 Btu/hr/ft^2/°F with 80°F ambient air. These were imposed primarily to simulate metal temperatures and not for evaluation of the turbine heat loss or insulation design. Actually, the external boundary conditions made little difference in metal temperatures when "super-insulation" properties were assumed.

Description of Analysis

General. - The basic analytical tool used was a general steady-state heat transfer program. This program is for finite-difference temperature solutions using relaxation techniques. It handles conduction, convection, and radiation modes and has the capability of simulating complex thermal systems, including finite-flow cooling streams.

Thermal modeling of the Mini-BRU was done by dividing the unit into parts so that the desired detail could be achieved in each part without exceeding the program limit of 400 thermal nodes. This also reduces computer time used for evaluating design changes which have no effect on other parts of the unit. The parts modeled separately are described as follows:

(1) Compressor-end - includes the compressor wheel, thrust bearing, copper heat shunt, journal bearing and alternator end-bell on the compressor side

(2) Turbine rotor - includes the turbine wheel and shaft, journal bearing, and the rotor back-shroud and support cylinder

(3) Turbine structure - includes the turbine inlet plenum, nozzle, shroud, exhaust duct, Z-shell support structure, mounting flange, alternator and end-bell on the turbine side, and insulation

The alternator was designed and analyzed separately (see earlier section) by the alternator designers with a thermal model including the alternator stator, field coils, rotor, and frame. The end-bells, heat sink surface, and the foil bearings were also included to provide suitable boundary conditions. The only area not included in any thermal model is the compressor structure, i.e., the inlet duct, shroud, diffuser, and supporting structure. These are in close proximity to the compressor through-flow and so will be within a few degrees of the local gas temperature along the main flow path.

Separate thermal models were used by the alternator designers and the turbine designers. In order to make the various thermal models compatible, it was necessary to match conditions at each interface between models, i.e., the temperature and heat flux at each interface must be identical with respect to both thermal models involved. For each of the operating conditions given in the operating and boundary conditions section, the steady state characteristic (heat flux versus temperature) was determined for each interface of each model. These were cross-plotted and used to simulate the neighboring model at each interface, i.e., the slope and intercept of each characteristic line establishing the equivalent thermal resistance and adiabatic temperature, respectively. A schematic of each of the three Phoenix models is presented in Figures 306, 307 and 308, respectively.

Bearing Cooling. - Special modeling programs have been developed to generate thermal models for gas-cooled foil bearings of the type used in the Mini-BRU. These are quite detailed three-dimensional models and so require a large number of thermal nodes, 110 for a journal bearing and 178 for a thrust bearing.

It was initially expected that all three foil bearings would be gas cooled. It was to be done by sealing the compressor side of the thrust bearing and injecting compressor bleed flow into the rotor rim cavity such that the cooling flow would be forced to pass through all three bearings in series and exit at the turbine-end. The compressor-end bearings, thrust and journal, were later found to be adequately cooled by conduction only, provided the conduction path from thrust rotor to compressor impeller was improved by means of a copper shunt. Nonetheless, these two bearings, as well as the gas-cooled bearing on the turbine-end, were modeled by use of the modeling codes and both are included in the overall model of the compressor-end, Model 1, shown in Figure 306. The number of nodes in this model is therefore very large, and it is necessary to show detailed schematics of the bearings separately. The thrust bearing schematic is shown in Figure 309 and the journal bearing schematic in Figure 310.

Likewise, the gas-cooled turbine-end bearing is part of the turbine rotor model, Model 2, Figure 307. A detailed schematic of this bearing is shown in Figure 311. A cooling flow diagram, shown in Figure 312, indicates the flow paths, flow rates, and computed gas temperatures at various points. The results are discussed in the next section, including the effects of scalloping the turbine wheel rim in order to achieve better thrust balancing.

The gas cooling design of the turbine-end bearing consists of a simple axial flow straight through the foil sway space and bearing film space. Axial grooves are machined in the bearing carrier bore surface in order to provide sufficient flow area. At the design cooling gas flow rate, the turbine bearing pressure drop is designed to match the overall pressure drop from compressor-end to turbine-end, setting the pressure drop (and flow) across the compressor-end bearings to zero. The design point for this purpose is the low power condition. At other conditions and/or with a scalloped turbine wheel, the pressures in the alternator cavity and at the compressor shaft are not matched, and some leakage occurs through the compressor bearings. The leakage rate is very small, however, as indicated in the table of Figure 312, since the compressor-end journal bearing, having no axial grooves, effectively acts as a shaft seal. The ability of this bearing to serve as a shaft seal arises from its small clearance and low pressure drop. The leakage flow is laminar and therefore, expressed as a percentage of cycle flow, depends only on pressure drop across the bearing and not on absolute pressure level. It is superior to a labyrinth seal of equal clearance, particularly at low pressure levels when flow Reynolds' numbers are low and friction factors high.

Friction heat is generated in a journal bearing in the film space, primarily where its thickness is minimum, and is distributed uniformly along the bearing length. Most of this heat is conducted into the foils and from there to the sway space. In the turbine-end bearing, some of this heat is carried away by the cooling flow and the rest is transferred to the bearing carrier by convection and by conduction through the contact areas of the foils on the bore surface. From there it is conducted through the end-bell to the alternator frame and into the main flow. The remaining heat enters the journal surface and is conducted axially to the inlet side, where it is convected to the cooling flow passing over the rotating surface upstream of the bearing. Since there is no appreciable cooling flow supplied to the compressor-end bearing, virtually all the frictional heat is transferred radially outward to the end-bell and into the main flow.

In the thrust bearing, up to 25 percent of the heat generated is due to windage at the rim of the thrust runner. It is primarily this portion which is convected into the bearing housing and conducted on to the alternator frame and enters the main flow. Frictional heat generated in the bearing films cannot escape across the foils and sway space because the thermal resistance there is high. It, therefore, enters the thrust runner surface, conducts inwardly to the shaft and

enters the copper sleeve inside the rotor. The copper conducts axially into the bore surface of the impeller, which dissipates heat to the main flow path along its hub surface and blades.

Results of Analysis

Computed metal temperatures are presented in Tables LIV through LIX, attached. Tables LIV and LV are for the compressor-end, Model 1, representing the high power and low power conditions, respectively. Some of the thermal nodes listed in the tables are not shown in the schematics; this is because some nodes are dummies and some are obscured from view or left out for clarity. These omissions do not alter the results except for the sake of completeness. Comparing the results of Tables LIX and LV with respect to the schematics of Figures 306, 309, and 310, it is seen that all temperatures and their gradients are highest for the high power level, except that slightly higher temperatures are seen in the impeller hub inlet region at low power. The bearing foil temperatures are well within their limits with the hot spot reaching 411°F in the thrust bearing and 372°F in the journal bearing. Each point shown in Figure 310 is a series of five thermal nodes numbered sequentially, ascending from compressor side toward turbine side.

Tables LVI and LVII apply to the turbine rotor, back-shroud, and bearing, Model 2. The appropriate schematics are Figures 307 and 311. The metal temperatures are higher at the low power condition except in the turbine wheel rim area, blades, and the outer part of the back-shroud. This is because the bleed flow has the highest cooling capacity or rate at the high power level and effectively cools the bearing and rotor to lower temperatures in spite of higher power losses in the bearings and alternator and of higher bleed gas supply temperature. The gas temperatures in the bleed flow path are spotted in Figure 312. At the rim of the turbine wheel, bleed gas temperatures exceed 1200°F. Much more heat is absorbed by the flow over the turbine wheel backface at high power because of increased backface windage and heat transfer coefficients, which increase with gas density. This also means increased heat transfer to the back-shroud and hence higher back-shroud metal temperatures and radial temperature gradients.

Peak metal temperature in the turbine wheel is about 1290°F and radial temperature gradients are maximum at the high power condition; this represents the worst case for life of the wheel. The life is well over 10 years according to the turbine stress analysis. In fact, a substantial growth potential exists for higher turbine inlet gas temperatures.

TABLE LIV. - MODEL 1 METAL TEMPERATURES, HIGH POWER LEVEL

STN	TEMP.	STN	TEMP.	STN	TEMP.	STN	TEMP.	STN	TEMP.
1	111.09	2	110.92	3	111.03	4	110.90	5	114.32
6	110.85	7	119.15	8	145.08	9	150.55	10	189.62
11	218.12	12	252.13	13	278.36	14	109.84	15	112.44
16	121.42	17	156.53	18	196.04	19	221.49	20	247.86
21	299.42	22	331.94	23	219.09	24	213.17	25	294.10
26	300.73	27	303.32	28	306.34	29	309.46	30	280.78
31	295.70	32	301.06	33	305.37	34	290.35	35	302.05
36	309.99	37	310.40	38	271.07	39	275.98	40	276.58
41	273.24	42	273.12	43	268.03	44	267.54	45	261.60
46	260.68	47	264.09	48	259.78	49	259.87	50	259.94
51	264.98	52	291.17	53	258.42	54	257.72	55	261.20
56	261.82	57	263.01	58	265.23	59	266.12	60	263.53
61	267.14	62	263.66	63	266.20	64	272.81	65	272.86
66	263.95	67	262.36	68	262.18	69	262.13	70	263.84
71	269.20	72	275.37	73	411.40	74	410.66	75	403.94
76	393.20	77	382.76	78	411.16	79	411.05	80	404.33
81	393.04	82	381.07	83	410.13	84	409.87	85	403.41
86	392.83	87	382.66	88	391.34	89	399.00	90	398.47
91	388.36	92	381.19	93	377.45	94	387.66	95	387.66
96	381.49	97	379.84	98	401.55	99	408.44	100	401.48
101	392.74	102	383.63	103	397.27	104	405.27	105	401.41
106	391.74	107	383.72	108	394.89	109	401.12	110	397.59
111	388.91	112	381.25	113	374.94	114	388.20	115	387.84
116	381.54	117	378.38	118	398.88	119	402.24	120	398.12
121	389.10	122	381.01	123	374.14	124	387.92	125	388.98
126	380.53	127	379.19	128	291.54	129	298.13	130	297.55
131	300.84	132	302.72	133	291.39	134	294.08	135	297.52
136	300.83	137	302.78	138	290.08	139	293.66	140	297.37
141	300.80	142	303.25	143	287.05	144	291.93	145	297.92
146	409.47	147	408.78	148	399.66	149	389.37	150	378.10
151	388.56	152	385.21	153	391.14	154	389.96	155	389.67
156	327.93	157	329.63	158	331.52	159	334.83	160	301.89
161	400.00	162	400.00	163	400.24	164	402.90	165	400.01
166	391.70	167	383.08	168	399.52	169	403.01	170	400.22
171	391.91	172	383.42	173	399.31	174	402.38	175	399.86
176	391.49	177	383.08	178	384.05	179	394.13	180	394.82
181	388.56	182	382.57	183	374.44	184	388.56	185	388.95
186	388.98	187	380.05	188	393.37	189	400.78	190	399.12
191	391.43	192	384.02	193	387.78	194	398.12	195	397.74
196	390.72	197	384.29	198	387.04	199	395.85	200	395.52
201	389.00	202	382.69	203	375.44	204	387.03	205	389.02
206	388.42	207	380.00	208	388.08	209	396.73	210	395.84
211	388.93	212	382.15	213	375.58	214	388.66	215	388.10
216	382.99	217	378.14	218	283.05	219	284.14	220	285.31
221	286.80	222	287.02	223	282.93	224	284.13	225	285.49
226	286.56	227	287.00	228	282.36	229	283.94	230	285.41
231	286.50	232	286.98	233	280.94	234	278.10	235	277.84
236	402.18	237	400.60	238	396.16	239	387.43	240	376.51
241	366.75	242	352.21	243	338.75	244	336.88	245	332.77
246	341.74	247	343.51	248	349.69	249	328.19	250	288.96
251	359.54	252	362.87	253	366.55	254	369.19	255	370.34
256	358.61	257	362.46	258	367.27	259	370.32	260	371.77
261	342.93	262	345.57	263	351.36	264	356.06	265	358.96
266	324.74	267	327.37	268	332.17	269	336.87	270	342.90
271	327.21	272	330.55	273	335.17	274	341.93	275	346.17
276	318.91	277	322.52	278	326.82	279	334.30	280	339.48
281	348.51	282	352.93	283	358.74	284	363.22	285	365.75
286	335.39	287	339.88	288	345.03	289	350.64	290	354.34
291	353.20	292	357.81	293	363.43	294	367.89	295	370.91
296	343.16	297	346.15	298	354.11	299	359.05	300	361.87
301	354.16	302	356.96	303	363.22	304	364.08	305	371.11
306	344.07	307	350.29	308	356.69	309	361.80	310	364.33
311	352.79	312	357.29	313	363.42	314	367.33	315	369.46
316	350.28	317	354.82	318	360.96	319	365.05	320	367.33
321	312.93	322	316.02	323	320.89	324	328.14	325	333.12
326	299.21	327	303.39	328	306.77	329	310.99	330	323.00
331	295.96	332	300.26	333	303.48	334	314.09	335	320.96
336	292.50	337	295.43	338	303.82	339	312.88	340	319.51
341	292.17	342	295.11	343	303.51	344	312.37	345	319.24
346	293.01	347	295.70	348	301.45	349	312.58	350	319.92
351	291.77	352	294.81	353	300.38	354	311.03	355	319.08
356	540.61	357	524.82	358	536.30	359	539.82	360	541.01
361	315.78	362	335.82	363	573.66	364	484.72	365	466.66
366	461.27	367	432.78	368	442.48	369	434.28	370	429.87
371	426.15	372	409.63	373	391.97	374	388.13	375	358.87
376	299.74	377	310.39	378	332.66	379	342.54	380	350.96
381	358.10	382	342.98	383	366.78	384	368.94	385	369.73
386	423.47	387	390.58	388	383.11	389	311.13	390	349.83

TABLE LV. - MODEL 1 METAL TEMPERATURES, LOW POWER LEVEL

STN	TEMP.	STN	TEMP.	STN	TEMP.	STN	TEMP.	STN	TEMP.
1	120.01	2	119.86	3	120.43	4	119.82	5	122.09
6	119.35	7	120.52	8	131.64	9	199.98	10	100.37
11	189.76	12	210.69	13	230.10	14	110.80	15	121.42
16	130.07	17	189.09	18	196.00	19	213.68	20	230.09
21	228.51	22	213.31	23	203.19	24	193.47	25	260.85
26	291.80	27	283.41	28	285.33	29	287.31	30	293.38
31	256.66	32	282.02	33	284.83	34	255.17	35	282.83
36	287.35	37	119.74	38	299.00	39	240.22	40	240.91
41	244.12	42	244.08	43	237.96	44	239.57	45	234.96
46	234.07	47	239.67	48	233.42	49	233.30	50	233.41
51	235.89	52	233.98	53	232.34	54	234.03	55	233.88
56	234.29	57	234.87	58	238.13	59	236.54	60	235.13
61	237.05	62	235.21	63	236.72	64	240.04	65	240.67
66	236.50	67	236.36	68	238.36	69	230.74	70	237.48
71	240.48	72	241.75	73	332.99	74	331.90	75	327.42
76	320.84	77	314.09	78	332.84	79	332.11	80	327.07
81	320.83	82	314.24	83	332.22	84	331.90	85	327.08
86	320.37	87	313.99	88	320.81	89	324.33	90	322.23
91	317.07	92	312.57	93	312.08	94	316.78	95	316.16
96	316.45	97	309.18	98	320.72	99	330.21	100	326.82
101	320.24	102	314.52	103	324.83	104	328.64	105	325.70
106	319.51	107	314.43	108	322.93	109	325.07	110	322.99
111	317.47	112	312.67	113	312.81	114	316.99	115	316.02
116	312.07	117	308.98	118	324.40	119	328.58	120	323.48
121	317.69	122	312.57	123	312.62	124	316.81	125	315.58
126	311.37	127	307.98	128	290.88	129	292.11	130	291.91
131	285.91	132	286.34	133	290.81	134	292.09	135	293.91
136	285.52	137	286.37	138	290.05	139	292.05	140	294.04
141	285.71	142	286.73	143	298.33	144	295.17	145	292.73
146	330.38	147	328.57	148	324.19	149	317.87	150	310.99
151	305.22	152	297.10	153	287.96	154	295.35	155	287.47
156	279.22	157	280.40	158	289.38	159	290.93	160	296.93
161	280.00	162	280.00	163	325.80	164	320.18	165	324.15
166	319.01	167	313.64	168	325.33	169	329.29	170	324.29
171	319.14	172	313.85	173	325.12	174	329.68	175	323.93
176	318.86	177	313.61	178	317.31	179	321.15	180	320.85
181	316.76	182	313.03	183	311.70	184	310.43	185	316.84
186	313.67	187	311.13	188	322.39	189	329.13	190	323.81
191	318.78	192	314.15	193	319.86	194	323.75	195	322.77
196	318.28	197	314.25	198	318.81	199	322.10	200	321.22
201	317.08	202	313.13	203	312.14	204	316.63	205	316.86
206	313.84	207	311.11	208	319.81	209	322.89	210	321.49
211	317.69	212	312.83	213	312.29	214	316.39	215	316.25
216	312.65	217	309.60	218	245.26	219	245.94	220	246.75
221	247.35	222	247.57	223	245.21	224	245.92	225	246.74
226	247.35	227	247.57	228	244.94	229	245.90	230	246.79
231	247.41	232	247.63	233	244.08	234	245.91	235	252.62
236	324.37	237	323.51	238	321.38	239	316.34	240	309.74
241	303.78	242	299.66	243	286.12	244	285.96	245	282.17
246	275.16	247	277.63	248	292.52	249	293.29	250	297.03
251	314.09	252	319.69	253	324.42	254	328.47	255	331.48
256	313.20	257	320.21	258	325.00	259	329.30	260	332.47
261	299.04	262	300.80	263	305.97	264	311.90	265	310.99
266	281.46	267	286.72	268	291.53	269	298.08	270	303.84
271	287.17	272	293.36	273	297.81	274	304.92	275	304.99
276	280.33	277	292.87	278	290.10	279	297.25	280	303.20
281	304.98	282	312.93	283	317.87	284	322.98	285	320.82
286	294.52	287	301.20	288	305.72	289	312.02	290	310.51
291	308.29	292	317.11	293	321.98	294	329.68	295	330.41
296	301.81	297	309.15	298	313.23	299	318.10	300	322.04
301	309.62	302	317.85	303	322.74	304	327.50	305	331.04
306	302.16	307	308.75	308	313.83	309	319.31	310	323.19
311	308.29	312	316.16	313	321.21	314	326.08	315	329.54
316	306.18	317	313.66	318	318.66	319	323.87	320	327.48
321	273.78	322	278.05	323	282.85	324	290.41	325	295.78
326	284.88	327	289.19	328	272.08	329	282.37	330	289.12
331	282.40	332	288.51	333	289.87	334	279.83	335	286.19
336	259.29	337	282.33	338	270.07	339	278.48	340	285.49
341	259.12	342	282.11	343	289.85	344	278.27	345	285.20
346	259.93	347	282.88	348	288.32	349	278.71	350	286.03
351	259.16	352	281.88	353	287.34	354	277.83	355	285.21
356	435.72	357	309.02	358	407.27	359	471.67	360	475.24
361	271.35	362	309.60	363	408.19	364	349.83	365	378.34
366	371.06	367	451.08	368	329.73	369	343.07	370	345.29
371	302.93	372	331.99	373	320.12	374	309.98	375	302.38
376	296.85	377	291.99	378	278.58	379	288.40	380	298.94
381	309.35	382	316.07	383	326.30	384	331.38	385	333.05
386	292.21	387	333.79	388	283.81	389	277.34	390	279.13

TABLE LVI. - MODEL 2 METAL TEMPERATURES, HIGH POWER LEVEL

SIN	TEMP.	SIN	TEMP.	SIN	TEMP.	SIN	TEMP.	SIN	TEMP.
1	462.80	2	500.00	3	475.57	4	496.69	5	517.80
6	517.52	7	472.32	8	493.70	9	517.84	10	557.58
11	582.47	12	606.87	13	635.93	14	674.95	15	733.84
16	813.21	17	891.33	18	938.06	19	945.43	20	944.37
21	979.81	22	1043.94	23	1038.46	24	1022.90	25	1027.83
26	1065.80	27	1087.35	28	1080.70	29	1070.40	30	1054.90
31	1029.29	32	1042.73	33	1043.52	34	1093.29	35	1102.52
36	1087.37	37	1080.65	38	1080.85	39	1025.09	40	1041.14
41	1058.53	42	1056.68	43	1134.24	44	1137.20	45	1097.43
46	1083.34	47	1075.76	48	1118.17	49	1115.89	50	1124.70
51	1158.97	52	1130.90	53	1072.76	54	1025.13	55	1039.69
56	1055.11	57	1070.92	58	1069.73	59	1176.70	60	1178.98
61	1193.75	62	1114.22	63	1102.21	64	1093.27	65	1088.28
66	1132.76	67	1152.00	68	1141.34	69	1138.92	70	1144.08
71	1150.68	72	1209.38	73	1175.27	74	1089.34	75	1083.98
76	1179.66	77	1196.39	78	1204.62	79	1202.17	80	1223.28
81	1242.75	82	1130.43	83	1164.70	84	1140.85	85	1141.77
86	1120.47	87	1111.64	88	1104.81	89	1100.07	90	1159.36
91	1210.37	92	1186.70	93	1167.05	94	1158.06	95	1155.19
96	1154.33	97	1159.65	98	1169.83	99	1242.66	100	1219.20
101	1097.80	102	1230.40	103	1233.33	104	1253.63	105	1275.04
106	1286.16	107	1187.77	108	1147.93	109	1138.11	110	1223.56
111	1250.08	112	1129.14	113	1120.58	114	1113.75	115	1110.31
116	1164.64	117	1244.59	118	1208.54	119	1154.09	120	1164.31
121	1272.90	122	1133.33	123	1124.60	124	1120.11	125	1220.81
126	1177.51	127	1166.68	128	1287.29	129	1258.82	130	1154.29
131	1141.17	132	1130.89	133	1125.52	134	1180.74	135	1177.22
136	1189.81	137	1195.96	138	451.17	139	475.09	140	501.86
141	403.29	142	412.53	143	421.79	144	430.32	145	437.39
146	403.23	147	412.24	148	422.33	149	430.82	150	437.80
151	390.74	152	397.67	153	407.20	154	415.29	155	421.54
156	379.10	157	384.37	158	393.07	159	400.64	160	406.14
161	380.36	162	386.63	163	396.24	164	404.21	165	410.03
166	374.60	167	380.76	168	390.25	169	398.21	170	403.88
171	395.47	172	403.43	173	413.87	174	422.22	175	428.93
176	384.25	177	391.09	178	400.32	179	408.49	180	415.02
181	398.91	182	407.09	183	417.66	184	425.09	185	432.94
186	389.06	187	395.76	188	405.83	189	413.22	190	420.05
191	399.70	192	407.98	193	418.62	194	427.04	195	433.87
196	389.54	197	396.41	198	405.48	199	413.81	200	420.59
201	398.31	202	406.49	203	416.97	204	425.39	205	432.02
206	395.81	207	403.80	208	414.00	209	422.40	210	428.97
211	371.35	212	376.16	213	384.18	214	391.50	215	396.80
216	360.68	217	366.47	218	376.15	219	384.08	220	389.37
221	358.48	222	364.68	223	374.04	224	381.95	225	387.11
226	356.64	227	363.01	228	375.29	229	380.48	230	384.90
231	356.49	232	362.40	233	375.18	234	380.33	235	384.72
236	353.50	237	357.91	238	371.60	239	380.66	240	388.07
241	352.69	242	356.21	243	371.24	244	380.32	245	387.68
246	583.21	247	578.64	248	591.26	249	599.70	250	606.35
251	504.07	252	482.49	253	466.60	254	434.82	255	416.14
256	744.03	257	1136.76	258	1378.11	259	1457.01	260	379.64
261	372.25	262	349.89	263	402.36	264	340.24	265	456.70
266	576.58	267	675.30	266	762.36	269	814.74	270	870.62
271	924.74	272	960.84	273	1107.62	274	1034.88	275	933.06
276	814.51	277	694.63	278	573.17	279	516.75	280	477.71
281	931.91	282	996.83						

TABLE LVII. - MODEL 2 METAL TEMPERATURES, LOW POWER LEVEL

STN	TEMP.	STN	TEMP.	STN	TEMP.	STN	TEMP.	STN	TEMP.
1	599.68	2	613.19	3	593.99	4	617.21	5	631.31
6	639.12	7	595.16	8	618.25	9	647.75	10	714.68
11	758.07	12	799.08	13	840.96	14	885.94	15	935.94
16	992.86	17	1036.79	18	1068.72	19	1081.49	20	1084.32
21	1080.04	22	1105.81	23	1101.59	24	1096.49	25	1097.51
26	1111.10	27	1111.69	28	1115.22	29	1112.63	30	1107.56
31	1099.29	32	1105.11	33	1105.73	34	1119.42	35	1121.02
36	1112.19	37	1116.16	38	1110.77	39	1101.14	40	1106.04
41	1111.01	42	1111.13	43	1129.15	44	1129.28	45	1122.41
46	1118.20	47	1116.39	48	1126.19	49	1126.19	50	1129.62
51	1136.62	52	1129.34	53	1116.20	54	1102.29	55	1106.31
56	1111.16	57	1116.18	58	1116.15	59	1141.30	60	1141.44
61	1147.09	62	1129.33	63	1125.71	64	1123.20	65	1122.09
66	1133.06	67	1135.75	68	1133.15	69	1133.28	70	1135.68
71	1138.50	72	1153.15	73	1142.22	74	1121.55	75	1121.32
76	1141.47	77	1145.16	78	1148.50	79	1147.49	80	1156.52
81	1164.99	82	1136.76	83	1148.16	84	1137.01	85	1157.30
86	1133.53	87	1130.75	88	1128.68	89	1127.27	90	1142.35
91	1163.54	92	1146.18	93	1140.43	94	1138.27	95	1138.41
96	1138.94	97	1141.18	98	1145.33	99	1169.30	100	1156.93
101	1126.60	102	1158.00	103	1159.15	104	1168.19	105	1178.15
106	1183.43	107	1160.07	108	1145.12	109	1141.61	110	1174.30
111	1185.48	112	1138.40	113	1135.32	114	1132.83	115	1131.58
116	1153.78	117	1187.17	118	1170.60	119	1149.54	120	1145.53
121	1200.40	122	1141.00	123	1137.44	124	1135.63	125	1179.01
126	1161.30	127	1156.64	128	1211.08	129	1196.52	130	1150.71
131	1144.70	132	1140.20	133	1137.92	134	1164.66	135	1183.34
136	1172.36	137	1169.52	138	552.10	139	578.37	140	606.86
141	453.88	142	468.02	143	482.93	144	498.16	145	513.73
146	453.89	147	467.15	148	482.65	149	497.53	150	512.35
151	434.44	152	444.33	153	459.46	154	471.57	155	481.85
156	425.85	157	434.42	158	448.07	159	459.67	160	468.41
161	430.97	162	440.46	163	454.90	164	467.41	165	477.45
166	425.12	167	433.94	168	447.97	169	459.95	170	469.01
171	446.04	172	457.34	173	472.89	174	486.79	175	499.46
176	434.95	177	445.01	178	459.29	179	472.25	180	482.97
181	449.65	182	461.20	183	477.04	184	491.32	185	504.53
186	440.11	187	450.09	188	464.85	189	478.68	190	490.14
191	450.47	192	462.10	193	477.99	194	492.28	195	505.55
196	440.70	197	450.78	198	465.51	199	479.37	200	490.90
201	448.94	202	460.40	203	476.02	204	489.99	205	502.52
206	446.31	207	457.53	208	472.90	209	486.58	210	498.55
211	419.36	212	426.93	213	439.70	214	450.46	215	457.74
216	411.17	217	418.48	218	431.79	219	442.51	220	449.38
221	408.86	222	415.87	223	429.07	224	439.55	225	445.99
226	407.59	227	415.17	228	431.11	229	438.71	230	444.24
231	407.38	232	414.92	233	430.88	234	438.42	235	443.89
236	403.98	237	409.27	238	427.39	239	438.93	240	447.23
241	403.05	242	408.12	243	426.46	244	437.84	245	445.96
246	642.84	247	629.87	248	651.42	249	665.88	250	679.80
251	604.65	252	584.40	253	567.20	254	524.89	255	467.46
256	934.88	257	1147.32	258	1319.80	259	1317.03	260	425.42
261	412.60	262	399.01	263	528.72	264	396.73	265	480.64
266	580.94	267	671.72	268	755.58	269	804.87	270	852.37
271	896.23	272	939.59	273	1009.73	274	980.40	275	953.50
276	912.72	277	857.13	278	757.08	279	708.93	280	674.89
281	952.44	282	999.05						

TABLE LVIII. - MODEL 3 METAL TEMPERATURES, HIGH POWER LEVEL

STN	TEMP.	STN	TEMP.	STN	TEMP.	STN	TEMP.	STN	TEMP.
1	1557.94	2	1545.80	3	1555.16	4	1550.93	5	1548.01
6	1524.48	7	1492.52	8	1460.28	9	1467.04	10	1444.93
11	1388.93	12	1416.59	13	1471.46	14	1513.68	15	1537.07
16	1543.11	17	1560.11	18	1562.21	19	1539.18	20	1537.75
21	1513.39	22	1514.78	23	1531.70	24	1536.19	25	1540.32
26	1544.48	27	1549.35	28	1552.17	29	1553.75	30	1363.95
31	1335.24	32	1331.37	33	1471.17	34	1442.31	35	1405.34
36	1516.19	37	1299.49	38	1234.45	39	1160.94	40	1074.65
41	990.05	42	910.19	43	839.15	44	787.85	45	738.85
46	683.05	47	592.09	48	533.40	49	479.74	50	474.24
51	450.05	52	398.77	53	344.83	54	340.00	55	328.07
56	325.09	57	331.38	58	326.26	59	320.05	60	308.04
61	295.29	62	292.87	63	272.10	64	273.55	65	274.82
66	294.66	67	292.26	68	295.61	69	307.00	70	310.84
71	322.19	72	331.35	73	331.36	74	330.48	75	330.93
76	330.42	77	331.07	78	331.08	79	331.07	80	307.40
81	308.34	82	308.40	83	308.97	84	307.71	85	310.67
86	309.60	87	308.87	88	309.54	89	310.64	90	322.24
91	337.85	92	348.94	93	358.56	94	440.58	95	582.23
96	579.18	97	700.46	98	817.41	99	886.82	100	955.45
101	1025.65	102	1105.34	103	1077.94	104	970.45	105	803.78
106	739.87	107	632.71	108	579.17	109	530.97	110	330.70
111	308.61	112	358.97	113	359.39	114	104.05	115	93.49
116	89.36	117	100.32	118	97.46	119	98.86	120	616.58
121	1147.60	122	991.21	123	1272.78	124	745.94	125	1105.19
126	1063.00	127	709.44	128	869.03	129	652.10	130	309.88
131	647.49	132	292.10	133	177.40				

TABLE LIX. - MODEL 3 METAL TEMPERATURES, LOW POWER LEVEL

STN	TEMP.	STN	TEMP.	STN	TEMP.	STN	TEMP.	STN	TEMP.
1	1489.74	2	1486.51	3	1493.19	4	1494.55	5	1488.14
6	1472.68	7	1453.74	8	1434.58	9	1438.36	10	1431.99
11	1411.46	12	1430.23	13	1459.64	14	1476.28	15	1481.81
16	1482.58	17	1490.80	18	1482.53	19	1476.01	20	1479.99
21	1458.95	22	1455.02	23	1464.37	24	1468.53	25	1470.13
26	1473.61	27	1478.36	28	1481.64	29	1386.47	30	1385.07
31	1390.39	32	1342.24	33	1417.23	34	1392.01	35	1359.45
36	1458.44	37	1201.30	38	1207.72	39	1141.66	40	1063.45
41	986.33	42	919.36	43	849.79	44	803.38	45	759.83
46	690.49	47	624.57	48	570.76	49	519.81	50	514.17
51	491.96	52	443.75	53	392.87	54	388.36	55	375.49
56	372.43	57	380.76	58	377.46	59	373.44	60	365.44
61	356.84	62	355.21	63	337.71	64	334.49	65	334.97
66	344.94	67	342.99	68	345.44	69	352.61	70	356.27
71	369.47	72	380.52	73	380.63	74	380.36	75	380.39
76	380.35	77	380.52	78	380.51	79	380.50	80	351.16
81	352.47	82	352.19	83	352.55	84	350.74	85	353.46
86	353.03	87	352.74	88	353.03	89	353.66	90	384.76
91	379.96	92	391.29	93	397.68	94	486.22	95	589.92
96	682.52	97	797.43	98	822.28	99	876.93	100	930.62
101	984.22	102	1046.03	103	1022.61	104	951.54	105	869.59
106	776.32	107	649.07	108	641.76	109	603.81	110	390.34
111	352.47	112	397.94	113	397.89	114	135.69	115	110.49
116	101.11	117	125.87	118	120.44	119	119.26	120	639.48
121	1117.93	122	968.10	123	1248.98	124	757.73	125	1137.35
126	1050.44	127	720.32	128	874.11	129	672.33	130	433.98
131	866.20	132	410.89	133	277.40				

Foil hot spot temperatures in the turbine-end bearing are as high as 510°F at the low power condition and, therefore, are marginal with respect to the specified temperature limit for steady state operation. Figure 313 is an isothermal diagram of an unwrapped foil showing in detail the metal temperatures at the low power condition assuming zero eccentricity. The maximum temperature difference in a foil is found to be approximately 90°F.

Tables LVIII and LIX provide temperatures in the turbine static structure and insulation system, Model 3. The material used for all the hot structure, up to the bolted flange, was refractory metal, C-103. A major consideration in this material selection was to avoid joining refractory metal ducts to conventional alloys in a high temperature region. The partially enclosed region between the turbine inlet nozzle and the Z-shell support structure is packed with low conductivity insulation of the multi-foil type. Super-insulation of the multi-layered reflective foil type also will cover the external surfaces of the turbine inlet plenum and exhaust duct to minimize heat loss to the environment. Performance of the insulation system was not evaluated in this study, but the inclusion of estimated insulation properties in the thermal model produced wall temperatures sufficiently close to cycle gas temperatures that these may be used directly in subsequent evaluation of insulation systems.

In Figure 301, only a few of the insulation thermal nodes are identified, those representing the insulation surface exposed to the environment. All other insulation temperatures are bounded by metal temperatures so these are omitted for clarity. Metal and insulation temperatures and their gradients in the hot structure are seen to be highest at the high power condition. This is because heat transfer coefficients along the hot gas path (the heat source) increase with gas density. The alternator frame, which serves as a heat sink, is somewhat at low power due to the higher turbine bearing temperature and lower heat transfer coefficients along the main flow path. This effect also produces higher temperatures in the turbine mounting flange and much of the Z-shell structure at low power, but these are still sufficiently low so that the temperature limit for the O-ring seal there is not reached.

Figures 314 and 315 show some transient temperature results obtained from the overall thermal model constructed jointly by extending the alternator model. Temperatures versus time at representative locations in the turbine end, bearing, and alternator are shown for periods following an instantaneous start to high power conditions and s subsequent instantaneous shutdown. It is found that very high temperature response rates

in the turbine nozzle and shroud region would occur with an instantaneous start. Elsewhere, the response rates are moderate or low. Although not shown, a more detailed model was also constructed for a nozzle vane and its sidewalls. This model showed the temperature difference between the vane trailing edge, and the sidewall reached a maximum of 800°F after only two seconds following a sudden start. These results were not used to predict transient stresses or fatigue life due to the realization that starting would not be instantaneous. However, it indicates potential thermal low-cycle fatigue problems if very rapid starts are made.

Of more interest is the thermal soakback situation following a sudden shutdown, since this is a more realistic condition, especially if emergency stoppages are made. It is found that the turbine bearing temperature level can rise as much as 60°F during soakback. This is considered marginal with respect to degradation of the foil coating material. In the alternator, maximum temperatures were not reached after 12 minutes of real time; but, taking the worst case of no further heat loss to the environment, an equilibrium temperature level of 450°F was calculated. This is not considered harmful to the alternator materials over relatively short durations.

Comment

The analytical results described herein indicate marginal temperatures in only one area at one operating point; namely, the turbine bearing foil hot spot at the low power level. It exceeds the specified steady state temperature limit, and soakback temperatures following a rapid shutdown from this condition may exceed the specified maximum temperature limit by as much as 120°F.

The low power condition, as used in this analysis, represents the original low extremum of the design power range, which was a 1/2 heat source module configuration. This is no longer considered a realistic condition for design as no application is being considered with less than one 2400 W_t heat source module. Therefore, an estimate was made of the cooling flow, boundary conditions, and alternator interface conditions with the current 2400 W_t heat source configuration, and the turbine-end thermal models rerun accordingly. The results indicated the turbine bearing temperatures to be well under the 4000°F limit, actually closer to those at the high power condition rather than low power.

Even so, the bearing temperatures could easily be reduced further by a minor design change to the turbine back-shroud. The objective here would be to reduce axial heat conduction toward the bearing through the cylindrical portion of the shroud around the turbine wheel shaft.

STRESS AND DYNAMIC ANALYSIS

Summary. - This section provides a summary of the structural analysis of the Mini-BRU turbine and compressor rotors. The report specifically covers the steady-state elastic finite element stress analysis of the wheels, the blade and splitter natural frequency analysis, and the tie-bolt load and stress analysis. The rotating group can be seen in Drawing 240610.

Turbine Wheel Stress Analysis

Conclusions. - The turbine rotor will meet the stress and 10-year life requirements of the Mini-BRU mission. The analysis indicated the turbine wheel to have a conservative state of stress. The wheel in the scalloped configuration has a burst margin of 3.53, a minimum 0.1 percent creep life of $7.43(10)^6$ hours, and a low cycle fatigue life greater than 10^6 start cycles. Figure 316 presents a summary of stress and life at the high power condition. The high predicted creep life would permit substitution of a material such as Astroloy. Astroloy has approximately the same conductivity and density. Growth due to thermal expansion would be slightly different.

Only the fundamental frequency of the turbine blade should present any problems. The second mode for the blade occurs at approximately twenty-five times engine speed and the fundamental splitter frequency is approximately sixty-four times engine speed. These frequencies are much higher than anticipated excitations. The calculated interference of the blade fundamental frequency and the stator passing frequency occurs at 20 percent below design speed.

The tie-bolt has a maximum temperature well out of the creep range. Its low cycle fatigue life is greater than 10^5 start cycles. Load relaxation should not be a problem. The minimum tie-bolt load is approximately four times the load required to prevent separation of the rotor.

Introduction. - The configuration and design parameters of the Mini-BRU permitted the design of a conservative turbine rotor. The Mini-BRU turbine wheel operates at a low tip speed (about one-third current gas turbine designs), with short blade and splitter heights, in a noncorrosive environment at temperatures consistent with the high strength range of superalloys. The tie-bolt is configured such that its maximum temperature is well out of the creep range and the temperature difference between the tie-bolt and its outer structure is small.

The lower tip speed results in a lower stressed turbine wheel than most gas turbines. Due to the low stress levels burst margin and low cycle fatigue did not limit the design. Metal temperatures are consistent with the higher strength range of the wheel material. The combination of moderate

temperature and low stress values result in little problem with creep. The short height of the blades and splitters result in high natural frequencies. These high natural frequencies are far above the low integral order excitations leaving only the higher frequency excitation to contend with. The noncorrosive environment eliminates the corrosion and corresponding loss in properties common to gas turbines. Load relaxation and the possibility of failure of the tie-bolt is minimized by operating the tie-bolt at a low maximum temperature and at a low temperature difference with respect to the system it is locking up. The small temperature difference results in a smaller minimum load and a smaller load range. With the peak temperature well below the creep range the possibility of creep relaxing the tie-bolt load is averted.

Approach. - A tie-bolt and radial turbine wheel configuration similar to the BRU was selected for its advantages in the design of the tie-bolt. A tie-bolt passing through the bore of the turbine wheel was examined early in the design phase. As a result of excessive creep relaxation of the tie-bolt load, in the initial configuration, the BRU type configuration was chosen.

The parameters setting blade thickness and height result in a blade with a natural frequency on the order of stator passing frequency. Attempts to drive the frequency safely above the interference were unsuccessful. The final design has a calculated frequency that interferes at a speed 20 percent below design speed.

Two turbine wheels were analyzed. One is scalloped to adjust thrust load; the other is unscalloped.

(1) Turbine Wheel - Two configurations of the Mini-BRU turbine wheel were analyzed; the primary design, a scalloped wheel, and an unscalloped wheel as a secondary design. Both wheels were analyzed using the elastic finite element stress simulation program, ISOPDQ. Steady-state stresses and deflections were calculated for the high power condition. The finite element model grids are shown in Figures 317 and 318. The normal blade thickness is shown in Figure 319 and β, the blade turning angle, shown in Figure 320. The temperature distribution used is shown in Figure 321.

Separate models were used in the calculation of hub stresses and blade stresses. These models treated the balance material as blades (unable to support hoop load) and assumed a symmetric axial restraint at the turbine wheel to tie-bolt joint. The models differed in their treatment of the blade thickness. The model simulating hub stresses used the blade tangential thickness distribution to accurately

model the load of the blades. The model simulating hub stresses used the blade tangential thickness distribution to accurately model the load of the blades. The model simulating blade stresses used the normal thickness distribution to accurately model the centrifugal stress in the blade. Plots depicting the results of the stress analysis are composites of the two models. Figures 322, 323, 324, and 325 are plots of the stress distribution in the scalloped wheel at the higher power condition. Figures 326, 327, 328, and 329 are plots of the scalloped wheel at room temperature and 52,000 rpm. Figures 330, 331, 332, and 333 are plots of the stress distribution in the unscalloped wheel at the high power conditions. Figures 334, 335, 336, and 337 are plots of the stress distribution in the unscalloped wheel at room temperature and 52,000 rpm. Figures 338, 339, and 340 are deformation plots based on tangential blade thickness.

Deformations for a condition 20 seconds after engine starting were calculated using coarse temperatures from the transient thermal analysis. Temperatures are reported in Reference (1). The deformation of the scalloped configuration at 20 seconds is shown in Figure 339.

The stress levels of the wheels are quite low. The combination of low stresses and moderate temperature result in a very long creep life. The scalloped wheel has a much higher creep life than does the unscalloped wheel due to higher thermal stresses in the front face region near the tip of the unscalloped wheel. If the scalloped design were used, a forged material such as Astroloy could be substituted for the INCO-713LC. Astroloy's thermal conductivity and density are nearly identical to INCO-713LC. Astroloy's tensile and fatigue properties are better than the INCO-713LC and at the scalloped design limiting creep location Astroloy's creep properties are only slightly worse.

(2) Turbine Blade Natural Frequency - The turbine blade and splitter were each modeled on computer program 1322, VIBE1. A constant temperature, representative of the blade, was used due to the complexity of modeling the predicted temperature distribution. The hub fillet was neglected due to modeling problems. The hub was modeled as "built in" except in the scalloped region. The scalloped region was modeled as fixed in one model and free in a separate model. Little difference in frequency was observed between the fixed and free cases.

Due to the low radial height to meridional length ratio some grid problems were encountered in the analysis. The grid used is shown in Figure 341. The element used in this analysis technique is a constant thickness plate element. The combination of the constant thickness element and a reasonably coarse grid made simulation difficult. As a check on the results, a cantilever plate correlation was used to ratio the results of static frequency measurements of the PFE, BRU turbine blade. This wheel was similar in geometry, but larger. The correlation used is shown below.

$$f_M = f_B \left(\frac{\ell_B}{\ell_M}\right)^2 \left(\frac{t_M}{t_B}\right)\left(\frac{\psi_M}{\psi_B}\right)$$

where: f = static frequency

ℓ = exducer height

t = blade thickness at the exducer hub

ψ = a blade taper ratio parameter

The correlation assumes the exducer geometry to be directly relatable to fundamental blade frequency. This assumption is borne out in several other designs reviewed as long as the designs are generally similar. The two methods of predicting blade frequency checked within approximately 50 out of 12,000.

It was judged that both methods would tend to predict low due to neglected secondary effects. A 20 percent margin with respect to an interference with turbine nozzle passing frequency, seventeen times engine speed, was selected as acceptable. As can be seen in the Campbell diagram of Figure 342, the predicted fundamental frequency is below the possible interference with nozzle passing. Attempts to raise the frequency above nozzle passing frequency and achieve reasonable margin were unsuccessful.

Blade modes above the fundamental are quite high. The frequencies of predicted modes are listed on Figure 342.

The splitter was also modelled using VIBE1 in the same manner as was the blade. The model is shown in Figure 343. Frequencies predicted by the analysis

are tabulated on Figure 342. The frequencies are very high and are not expected to be a problem.

(3) Tie-Bolt - The rotor tie-bolt system shown in Drawing 240610 was simplified to a system of linear springs for the purpose of analysis. The outer structure, the alternator, compressor wheel, and thrust runner, were assumed to have an axial stiffness much greater than the tie-bolt. Their spring rates were therefore neglected. Thermal deflections combined with initial loading conditions were imposed on the spring system and tie-bolt loading was calculated. Tensile stresses were calculated from the loading.

The minimum required axial load was set by the requirement to prevent axial separation of the turbine curvic. Loads considered were dynamic moment, axial load due to torque transmission through a curvic, and thrust loading. The dynamic moment calculated at steady-state operation with a maximum unbalance of 0.0005 in. mass eccentricity was multiplied by 10.0 to cover passing through critical speeds during acceleration. The axial load due to torque transmission was multiplied by 1.5 to cover the acceleration condition. With the addition of the separating thrust load, the required minimum axial load was on the order of 300 lbs.

Initial calculations to approximate the engine operating loads and required preload were based on the conservative assumption of "half hot" conditions. The "half hot" assumption for acceleration assumes the outer structure at steady-state temperature with the tie-bolt at half steady-state temperature. For shutdown the reverse is assumed. The load distribution based on these assumptions is shown in Figure 344. Further definition of the temperature distribution was later gained from the shutdown transient thermal analysis. The effect of shutdown temperatures on load are also shown in Figure 344 demonstrating the conservatism of the original assumptions. Table LX following summarizes maximum tensile stresses and loads for a nominal tolerance build condition at various operation conditions.

TABLE LX. - TIE-BOLT STRESSES AND DEFLECTIONS

	Tie-Bolt Deformation (in.)	Load (lbs)	Max. Stress (psi)	Tie-Bolt Spring Rate (lb/in.)
Assembly	0.014	3010	77.4	$2.15\ (10)^5$
Steady State	0.0134	2550	65.5	$1.91\ (10)^5$
"half hot" Accel	0.0208	4010	103.1	$1.93\ (10)^5$
"half hot" Shutdown	0.0064	1220	31.4	$1.91\ (10)^5$
"calculated" Shutdown	0.0133	2510	64.6	$1.89\ (10)^5$

The tie-bolt will not limit the life of the Mini-BRU engine. Temperature and stress combinations are well out of the creep range, and the low cycle fatigue life is greater than 105 start cycles.

Rotor Dynamics Analysis

A rotor dynamics analysis of the Mini-BRU rotating group was conducted. Figure 345 shows the model used in the analysis. The journal foil bearings were assumed to be linear elastic springs with radial spring rates of 3500 lb/in. Table LIX shows the mechanical properties of the rotor/bearing system.

TABLE LXI. - MECHANICAL PROPERTIES OF THE MINI-BRU ROTOR/BEARING SYSTEM

Bearing Span, Center to Center, in.	3.63
Journal Bearing Spring Rate, lb/in.	3,500
Thrust Bearing Torsional Spring Rate, in.-lb/rad	100,000
Rotor C.G., from Center of Front Journal Bearing, in.	2.023
Rotor I_p, in.-lb-sec^2	0.00162
Rotor I_D, in.-lb-sec^2	0.0396
Rotor Weight, lb	2.206
Compressor (steel) Weight, lb	2.206
Compressor (steel), I_p, in.-lb-sec^2	0.00024
Turbine Weight, lb	0.519
Turbine I_p, in.-lb-sec^2	0.0006

The alternator located at the center of the bearing span acts as a negative spring, and its influence on the system varies with speed. Figure 346 shows the estimated negative spring rate as a function of speed. The intersection of the spring rate curve and the first and second critical speed plots determine the calculated first and second critical speeds (8,500 rpm and 15,800 rpm, respectively). The bending critical (125,700 rpm) remains above the limiting speed of the engine and hence, is not shown on the figure. Mode shapes for the first and second criticals are presented in Figure 347.

Because of the known nonlinearity of the foil bearings and uncertainty pertaining to their dynamic spring rates, a plot of critical speed versus journal bearing spring rate is presented in Figure 348 to cover a wide range of journal bearing

spring rates. As expected, the larger spring rate increased the first two criticals but did not appreciably affect the bending critical. The plot indicates that spring rates between the range of 2,500 lb/in. and 7,000 lb/in. are satisfactory.

The absolute dynamic bearing loads calculated with 0.0005 in. eccentricity are presented in Figure 349. The low spring rate combined with the high bending critical result in low dynamic bearing loads near the operating speed. These loads must be superimposed to steady state unidirectional loads due to maneuvers and rotor weight to obtain total bearing loads.

Compressor Stress Analysis

Material selection. - The Mini-BRU compressor disk was analyzed for steady-state stresses and displacement (flowering) characteristics. The low tip speed (500 ft/sec) results in very low stresses relative to current state-of-the-art impellers.

Aluminum was analyzed initially because of its desirable mechanical and fabrication characteristics. However, the small radius at the inducer hub results in little face area that must resist the axial tie-bolt load. Originally during a transient run the required tie-bolt axial load was calculated to be 6,000 lb; high axial stresses at the inducer precluded the use of aluminum as a candidate material.

Other candidate materials included titanium and various steels. It is intended that the compressor aid in cooling the thrust and front journal foil bearings by conducting heat away from the bearing area and transferring it into the flowstream. Hence, a good conductor is desirable. This precludes titanium and 17-4PH as material candidates. Stainless Steel 410 and ASTM 4340 were the remaining materials to be considered. Even though ASTM 4340 has better conduction properties, its low resistance to corrosion and limited use as a compressor material make it an undesirable risk. On the other hand, the excellent internal damping characteristics of SS410 and its wide usage as a compressor material was the basis for its selection as the compressor material. Although subsequent analysis showed that the maximum transient tie-bolt load was only approximately 3,000 lb (see Figure 350, the impeller material has remained Stainless Steel 410.

Stress deflection analysis - The Mini-BRU impeller stress and deflection analysis was performed using a finite element computer program ISOPDQ (finite element model shown in Figure 351. The analysis included rotation of the impeller at 62,400 rpm (120 percent speed), a 3,000-lb axial tie-bolt load, and the thermal gradient (see Figure 352.

Impeller dispalcements (see Figure 353) result primarily from the thermal gradient and the tie-bolt load. Axial deflection at the exducer (flowering) is 0.0015 inch, and the maximum axial displacement at the inducer is 0.00038 in. Radial displacements of the impeller are, in general, smaller and less significant than axial deflections.

The low tip speed of the compressor makes the disk stresses relatively low. Figure 354 shows lines of constant equivalent stress. The 3,000-lb tie-bolt load caused highest stresses at the inducer hub. Maximum stress (principal) reached 37,100 psi in this area. The high axial stress is due to the limited amount of hub area at this location. Since the yield strength of SS410 is 99,000 psi (100°F) it is clear that the material will be lightly loaded. Peak tangential stresses are lower than peak axial stresses.

The high axial stress on the wheel causes a compressive tangential component which partially neutralizes bore tangential stresses due to rotation. Compressive tangential stresses are (-11,600 psi) in the hub beneath the inducer. Bore stresses are lower than peak axial stresses.

The high axial stress on the wheel causes a compressive tangential component which partially neutralizes bore tangential stresses due to rotation. Compressive tangential stresses are (-11,600 psi) in the hub beneath the inducer. Bore stresses reach a maximum of 24,200 psi. Equivalent stresses closely follow axial stresses as illustrated in the figures.

Burst margin at 62,400 rpm for the impeller defined by the equation

$$N_{burst} = \left(\frac{0.85 \times \text{ultimate stress}}{\text{Average Tangential Stress}} \right)^{1/2}$$

is 3.83. This large number indicates the low stresses in the wheel.

Blade stresses. - A blade stress analysis (steady state) was conducted for the Mini-BRU impeller using the finite element (BOSS1) computer program. The full blade is shown in Figure 355 as a function of radius versus axial distance and shows lines of constant thickness. The relatively simple blade has a thickness of 0.015 in. at the shroud all along the blade. At the hub, the thickness is 0.025 in. and varies linearly from the hub to the shroud. The one line through the blade indicates a line of constant thickness of 0.020 in.

There is no reduction of blade thickness at the inducer or exducer, because the low speed reduces effect of shock losses at these regions.

Figure 356 shows lines of constant steady state stress for the compressor blade. Highest stresses occur near the discharge where centrifugal forces tend to straighten the backward curved blades. It is evident that the blades are very lowly stressed for steady state conditions, leaving much margin for vibrational stresses.

Blade natural frequencies. - Mode shapes and frequencies of the compressor blade design were investigated. The blade is thick for its height ("B" width) and this results in high blade natural frequencies. The fundamental mode, shown in Figure 357, occurs at 27,977 cps. Maximum stresses for this mode occur near the inducer hub as indicated.

The second mode occurs at a very high frequency, 68,284 cps and shown in Figure 358. Maximum stresses for this mode occur in several locations as illustrated in the figure. Several higher modes were also calculated at 76,299 cps, 96,380 cps, and 104,084 cps. These frequencies are sufficiently high to preclude possible excitation from traditional excitation sources as shown from the interference diagram of Figure 359. In fact, a 25/rev excitation is required to excite the fundamental blade frequency at 27,977 cps. Hence blade vibration should not be a problem for this design.

Turbine and Compressor Clearance Analysis

Introduction. - A thorough investigation into the deflection characteristics of the Mini-BRU closed cycle engine was conducted. Of primary importance was the valuation of the variations in room temperature clearances which exist at the turbine wheel-turbine shroud interface. The conditions which were considered were an engine start, steady state operation, a shutdown, several periods of time during soakback and finally an engine start during soakback.

Discussion. - The analyses were performed for essentially two engine configurations, one with a cast Inconel 713LC turbine wheel and the other with a forged Astroloy wheel. Both configurations assumed nonscalloped wheels. In general, the slightly higher coefficient of thermal expansion for Astroloy resulted in maximum clearance closures with this material. Figure 360 shows all the Mini-BRU materials which were used in the analysis. Note that at the turbine plenum flange, for this deflection analysis only, it was assumed that the bimetallic joint did not exist but rather that the part

was continuous columbium. This was done since, presently, the material for this section has not been chosen. The static structural deflections include the effects of the temperature and pressure loads; whereas, the rotor deflections account for the thermal effect and also the centrifugal strain and Poisson's contraction.

In an attempt to evaluate the worst-case relative excursions of the turbine wheel and shroud, several conditions were investigated. First, an engine start was considered. Initially the engine was assumed to be cold. This closed cycle engine should heat up during a start essentially like other engines, where the static structure heats at a more rapid rate than the turbine wheel and remainder of the rotating group. This process causes the shroud to grow away from the wheel both axially at the tip and radially at the turbine discharge end. Then, as the engine continues operating, the rotating group gradually reaches steady-state temperatures and thermally expands axially toward the shroud. Since it is not likely that any rubbing problem would occur during the start condition, no analytical evaluation of the relative deflections for this condition were performed. Transient thermal data for an engine start was available from a transient thermal analysis which was performed. The temperatures used for the soakback conditions which follow are also taken from this transient analysis.

The steady-state high power condition was performed to evaluate the operational clearances. The steady-state temperatures used for the machine are shown in Figure 361, and were determined from the thermal analysis. iThe axial deflections for the turbine shroud and wheel were determined relative to the thrust bearing (Figure 360). Tables LXII and LXIII present the steady-state deflection results, the axial and radial wheel-shroud interface deflections along with the resultant change in the initial room temperature clearance; a positive change being an increase in clearance and a negative one being an increase in clearance and a negative one being a decrease in the clearance. At the turbine inlet there is a net reduction in the axial cold clearance of 0.0034 in. and 0.0039 in. using the Inco 713LC and Astroloy wheels respectively. At the discharge end, the radial excursions result in a net closure of 0.0027 in. for the Inconel versus 0.0029 in. for the Astroloy. In addition to these critical areas, the deflections along the entire interface are given. With the present 0.007 in. to 0.009 in. build clearances, the operating clearances are shown in Table LXIV. These deflections are for a nonscalloped turbine wheel. For the scalloped wheel the axial deflections at the turbine inlet would reduce clearance approximately an additional 0.001 in., and there is essentially no difference in radial expansion at the turbine discharge end.

TABLE LXII. - TURBINE WHEEL--TURBINE SHROUD CALCULATED DEFLECTIONS RELATIVE TO THRUST BEARING

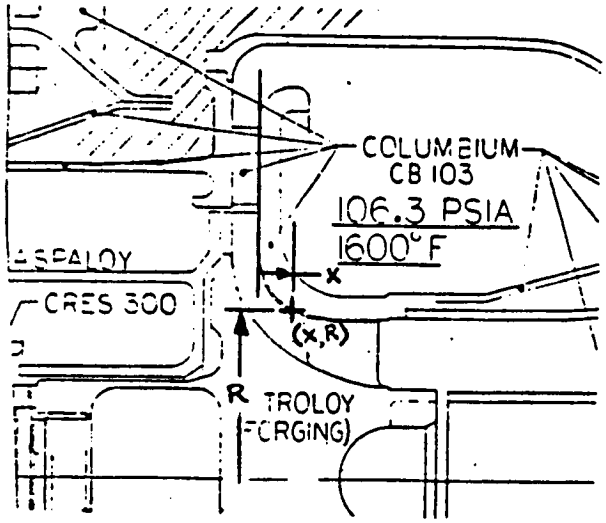

WHEEL MATERIAL	✓	INCO 713 LC
		ASTROLOY

OPERATING CONDITION

STEADY STATE

TURBINE WHEEL AND SHROUD DEFLECTIONS

	RADIUS	X	δ_{WHEEL} (AXIAL)	δ_{WHEEL} (RADIAL)	δ_{SHROUD} (AXIAL)	δ_{SHROUD} (RADIAL)	CHANGE IN R.T. CLEARANCE Δ (AXIAL)	CHANGE IN R.T. CLEARANCE Δ (RADIAL)
TURBINE INLET	1.428	0 (ref)	.0165	.0121	.0131	.0085	-.0034	-.0036
	1.30		.0163	.0109	.0131	.0077	-.0032	-.0032
	1.20		.0162	.0099	.0131	.0072	-.0031	-.0027
	1.10		.0163	.0090	.0131	.0066	-.0032	-.0024
	1.00	.074	.0167	.0082	.0133	.0060	-.0034	-.0022
	.913	.17	.0174	.0075	.0138	.0054	-.0036	-.0021
		.27	.0183	.0073	.0143	.0051	-.0040	-.0022
		.37	.0191	.0072	.0148	.0049	-.0043	-.0023
		.47	.0200	.0073	.0154	.0048	-.0046	-.0025
		.57	.0211	.0074	.0159	.0047	-.0052	-.0027
TURBINE DISCHARGE		.67	.0220	.0074	.0165	.0047	-.0055	-.0027

- $\Delta = \delta_{SHROUD} - \delta_{WHEEL}$
- A POSITIVE (+) Δ IS AN INCREASE IN THE ROOM TEMPERATURE CLEARANCE EXISTING BETWEEN THE SHROUD AND WHEEL
- A NEGATIVE (-) Δ IS A DECREASE IN THE ROOM TEMPERATURE CLEARANCE EXISTING BETWEEN THE SHROUD AND THE WHEEL

TABLE LXIII. - TURBINE WHEEL--TURBINE SHROUD CALCULATED DEFLECTIONS RELATIVE TO THRUST BEARING

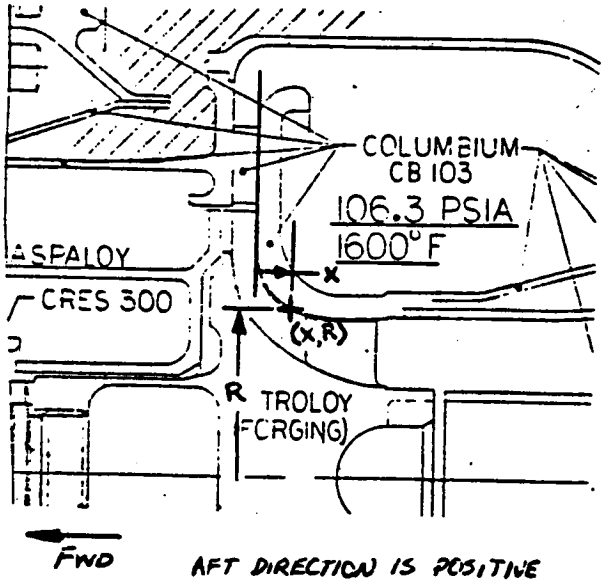

WHEEL MATERIAL		INCO 713 LC
	✓	ASTROLOY

OPERATING CONDITION

STEADY STATE

TURBINE WHEEL AND SHROUD DEFLECTIONS

	RADIUS	X	δ_{WHEEL} (Axial)	δ_{WHEEL} (Radial)	δ_{SHROUD} (Axial)	δ_{SHROUD} (Radial)	CHANGE IN R.T. CLEARANCE Δ (AXIAL)	CHANGE IN R.T. CLEARANCE Δ (RADIAL)
TURBINE INLET	1.428	0 (ref)	.0170	.0123	.0131	.0085	-.0039	-.0038
	1.30		.0169	.0110	.0131	.0077	-.0038	-.0033
	1.20		.0167	.0101	.0131	.0072	-.0036	-.0029
	1.10		.0168	.0091	.0131	.0066	-.0037	-.0025
	1.00	.074	.0172	.0083	.0133	.0060	-.0039	-.0023
	.913	.17	.0180	.0077	.0138	.0054	-.0042	-.0023
		.27	.0189	.0074	.0143	.0051	-.0046	-.0023
		.37	.0197	.0074	.0148	.0049	-.0049	-.0025
		.47	.0206	.0075	.0154	.0048	-.0052	-.0027
		.57	.0216	.0076	.0159	.0047	-.0057	-.0029
TURBINE DISCHARGE		.67	.0225	.0076	.0165	.0047	-.0060	-.0029

- $\Delta = \delta_{SHROUD} - \delta_{WHEEL}$
- A POSITIVE (+) Δ IS AN INCREASE IN THE ROOM TEMPERATURE CLEARANCE EXISTING BETWEEN THE SHROUD AND WHEEL
- A NEGATIVE (-) Δ IS A DECREASE IN THE ROOM TEMPERATURE CLEARANCE EXISTING BETWEEN THE SHROUD AND THE WHEEL

TABLE LXIV. - TURBINE OPERATING CLEARANCES

	Turbine inlet		Turbine discharge	
Wheel material	INCO-713LC	Astroloy	INCO 713LC	Astroloy
Steady state operating clearance, in.	0.0036 to 0.0056	0.0031 to 0.0051	0.0043 to 0.0063	0.0041 to 0.0061

The next condition in the engine cycle which was evaluated was a shutdown in which the unit was at steady-state temperature but no differential pressure loads existed on the structure. This condition essentially decreased axial turbine inlet clearances an additional 0.0015 in. over the steady-state values for both wheels. All of these results are shown in Tables LXV and LXVI.

The maximum axial inlet closure was not determined until several periods of time during soakback were evaluated. Details of the soakback thermal analysis were obtained from the transient thermal analysis where temperatures were calculated from shutdown to twelve minutes following shutdown. The deflections of the turbine wheel for shutdown were calculated, rather than being determined analytically by use of the computer analysis program which was used for steady-state conditions. The reasons that this soakback condition created worst case results were that the unit is a closed system and thereby all the heat had to be absorbed within the engine. The turbine wheel, which has a considerable amount of stored heat, cools slower than the shroud, and as it cools conducts the heat forward into the remainder of the rotating group. This creates a larger rotor axial deflection aft than during steady state. The heat in the shroud also redistributes into its supporting coned structure and these thermal gradients induce shroud deflections comparable to those during steady state. After evaluating the transient temperature data, the 4 and 12 minutes after shutdown conditions were chosen to be analyzed. Figures 362 and 363 show the temperatures for these conditions. The 4-minute condition, shown in Tables LXVII and LXVIII, produced the maximum reductions in axial clearances which were 0.0049 in. with the Inconel and 0.0052 in. with the Astroloy. The radial reductions in clearance for the soakback conditions were not as large as those at steady state. Tables LXIX and LXX show the critical excursions for the 12 minutes after shutdown condition. All of the data from the transient analysis is contained in Reference (5).

TABLE LXV. - TURBINE WHEEL--TURBINE SHROUD CALCULATED DEFLECTIONS RELATIVE TO THRUST BEARING

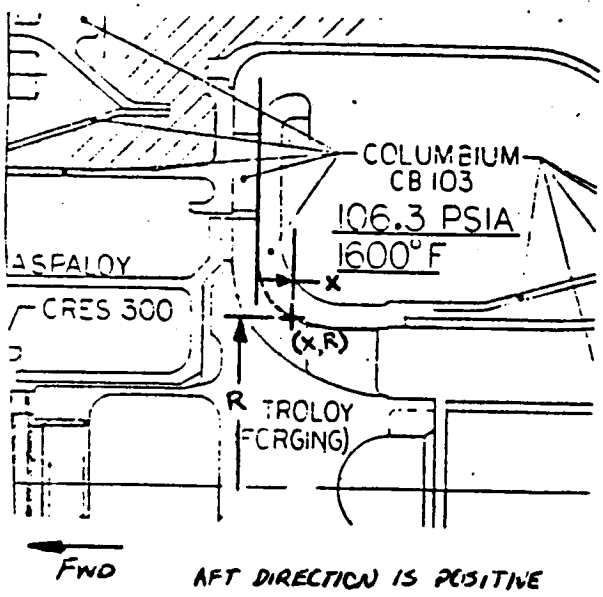

WHEEL MATERIAL	✓	INCO 713 LC
		ASTROLOY

OPERATING CONDITION

SHUTDOWN:

STEADY STATE TEMPERATURE, BUT NO PRESSURE

TURBINE WHEEL AND SHROUD DEFLECTIONS

	RADIUS	X	δ_{WHEEL} (Axial)	δ_{WHEEL} (Radial)	δ_{SHROUD} (Axial)	δ_{SHROUD} (Radial)	CHANGE IN R.T. CLEARANCE Δ (AXIAL)	CHANGE IN R.T. CLEARANCE Δ (RADIAL)
TURBINE INLET	1.428	0 (ref)	.0165	.0121	.0116	.0086	-.0049	-.0036
	1.30		.0163	.0109	.0115	.0079	-.0048	-.0030
	1.20		.0162	.0099	.0114	.0073	-.0048	-.0026
	1.10		.0163	.0090	.0114	.0067	-.0049	-.0023
	1.00	.074	.0167	.0082	.0116	.0061	-.0049	-.0021
	.913	.17	.0174	.0075	.0121	.0054	-.0053	-.0021
		.27	.0183	.0073	.0125	.0051	-.0058	-.0022
		.37	.0191	.0072	.0130	.0049	-.0061	-.0023
		.47	.0200	.0073	.0136	.0048	-.0064	-.0025
		.57	.0211	.0074	.0141	.0047	-.0070	-.0027
TURBINE DISCHARGE		.67	.0220	.0074	.0147	.0047	-.0073	-.0027

- $\Delta = \delta_{SHROUD} - \delta_{WHEEL}$
- A POSITIVE (+) Δ IS AN INCREASE IN THE ROOM TEMPERATURE CLEARANCE EXISTING BETWEEN THE SHROUD AND WHEEL
- A NEGATIVE (-) Δ IS A DECREASE IN THE ROOM TEMPERATURE CLEARANCE EXISTING BETWEEN THE SHROUD AND THE WHEEL

TABLE LXVI. - TURBINE WHEEL--TURBINE SHROUD CALCULATED DEFLECTIONS RELATIVE TO THRUST BEARING

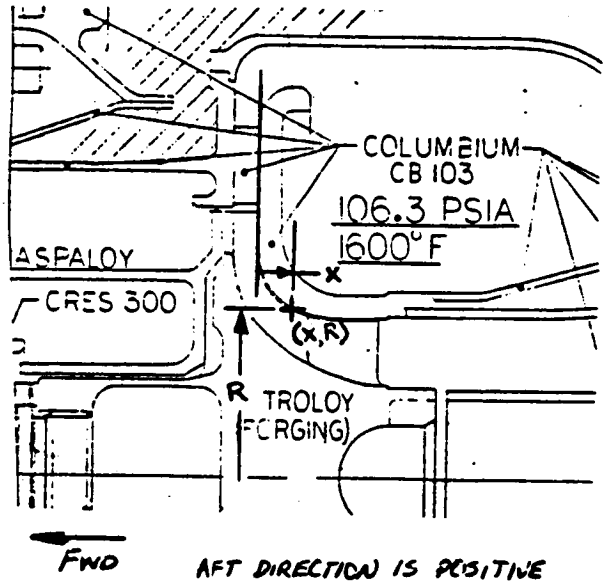

WHEEL MATERIAL		INCO 713 LC
	✓	ASTROLOY

OPERATING CONDITION

SHUTDOWN:

STEADY STATE TEMPERATURE, BUT NO PRESSURE

TURBINE WHEEL AND SHROUD DEFLECTIONS

	RADIUS	X	δ_{WHEEL} (Axial)	δ_{WHEEL} (Radial)	δ_{SHROUD} (Axial)	δ_{SHROUD} (Radial)	CHANGE IN R.T. CLEARANCE Δ (AXIAL)	CHANGE IN R.T. CLEARANCE Δ (RADIAL)
TURBINE INLET	1.428	0 (ref)	.0170	.0123	.0116	.0086	-.0054	-.0037
	1.30		.0169	.0110	.0115	.0079	-.0054	-.0039
	1.20		.0167	.0101	.0114	.0073	-.0053	-.0028
	1.10		.0168	.0091	.0114	.0067	-.0054	-.0024
	1.00	.074	.0172	.0083	.0116	.0061	-.0056	-.0022
	.913	.17	.0180	.0077	.0121	.0054	-.0059	-.0023
		.27	.0189	.0074	.0125	.0051	-.0064	-.0023
		.37	.0197	.0074	.0130	.0049	-.0067	-.0025
		.47	.0206	.0075	.0136	.0048	-.0070	-.0027
		.57	.0216	.0076	.0141	.0047	-.0075	-.0029
TURBINE DISCHARGE		.67	.0225	.0076	.0147	.0047	-.0078	-.0029

- $\Delta = \delta_{SHROUD} - \delta_{WHEEL}$
- A POSITIVE (+) Δ IS AN INCREASE IN THE ROOM TEMPERATURE CLEARANCE EXISTING BETWEEN THE SHROUD AND WHEEL
- A NEGATIVE (-) Δ IS A DECREASE IN THE ROOM TEMPERATURE CLEARANCE EXISTING BETWEEN THE SHROUD AND THE WHEEL

TABLE LXVII. - TURBINE WHEEL--TURBINE SHROUD CALCULATED DEFLECTIONS RELATIVE TO THRUST BEARING

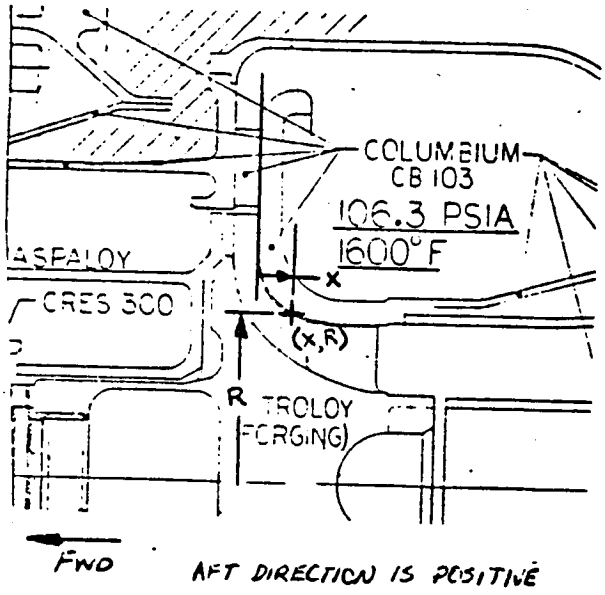

WHEEL MATERIAL	✓	INCO 713 LC
		ASTROLOY

OPERATING CONDITION

SOAKBACK:

4 MINUTES AFTER SHUTDOWN

TURBINE WHEEL AND SHROUD DEFLECTIONS

	Radius	X	δ_{WHEEL} (Axial)	δ_{WHEEL} (Radial)	δ_{SHROUD} (Axial)	δ_{SHROUD} (Radial)	CHANGE IN R.T. CLEARANCE Δ (AXIAL)	CHANGE IN R.T. CLEARANCE Δ (RADIAL)
TURBINE INLET	1.428	0 (ref)	.01810		.01325		-.0049	
	1.30		.01815		.01329		-.0049	
	1.20							
	1.10							
	1.00	.074						
	.913	.17						
		.27						
		.37						
		.47						
		.57						
TURBINE DISCHARGE		.67		.00670		.00427		-.0024

- $\Delta = \delta_{SHROUD} - \delta_{WHEEL}$
- A POSITIVE (+) Δ IS AN INCREASE IN THE ROOM TEMPERATURE CLEARANCE EXISTING BETWEEN THE SHROUD AND WHEEL
- A NEGATIVE (-) Δ IS A DECREASE IN THE ROOM TEMPERATURE CLEARANCE EXISTING BETWEEN THE SHROUD AND THE WHEEL

TABLE LXVIII. - TURBINE WHEEL--TURBINE SHROUD CALCULATED DEFLECTIONS RELATIVE TO THRUST BEARING

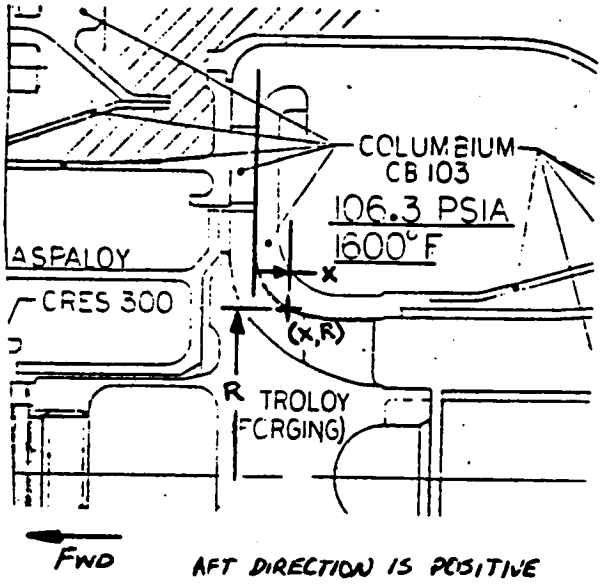

WHEEL MATERIAL		INCO 713 LC
	✓	ASTROLOY

OPERATING CONDITION

SOAKBACK:

4 MINUTES AFTER SHUTDOWN

TURBINE WHEEL AND SHROUD DEFLECTIONS

	RADIUS	X	δ_{WHEEL} (Axial)	δ_{WHEEL} (Radial)	δ_{SHROUD} (Axial)	δ_{SHROUD} (Radial)	CHANGE IN R.T. CLEARANCE Δ (AXIAL)	CHANGE IN R.T. CLEARANCE Δ (RADIAL)
TURBINE INLET	1.428	0 (ref)	.01842		.01325		-.0052	
	1.30		.01847		.01329		-.0052	
	1.20							
	1.10							
	1.00	.074						
	.913	.17						
		.27						
		.37						
		.47						
		.57						
TURBINE DISCHARGE		.67		.00690		.00427		-.0026

- $\Delta = \delta_{SHROUD} - \delta_{WHEEL}$
- A POSITIVE (+) Δ IS AN INCREASE IN THE ROOM TEMPERATURE CLEARANCE EXISTING BETWEEN THE SHROUD AND WHEEL
- A NEGATIVE (-) Δ IS A DECREASE IN THE ROOM TEMPERATURE CLEARANCE EXISTING BETWEEN THE SHROUD AND THE WHEEL

TABLE LXIX. - TURBINE WHEEL-TURBINE SHROUD CALCULATED DEFLECTIONS RELATIVE TO THRUST BEARING

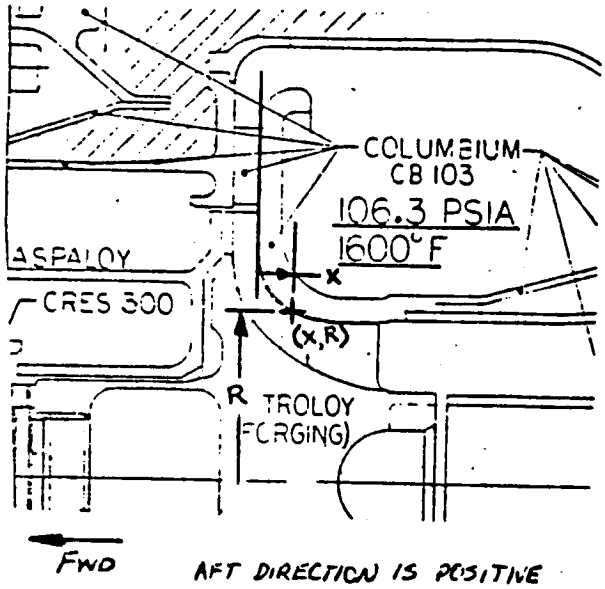

AFT DIRECTION IS POSITIVE

WHEEL MATERIAL	√	INCO 713 LC
		ASTROLOY

OPERATING CONDITION

SOAKBACK:

12 MINUTES AFTER SHUTDOWN

TURBINE WHEEL AND SHROUD DEFLECTIONS

	RADIUS	X	δ_{WHEEL} (Axial)	δ_{WHEEL} (Radial)	δ_{SHROUD} (Axial)	δ_{SHROUD} (Radial)	CHANGE IN R.T. CLEARANCE Δ (AXIAL)	CHANGE IN R.T. CLEARANCE Δ (RADIAL)
TURBINE INLET	1.428	0 (ref)	.01755		.01394		-.0036	
	1.30		.01758		.01402		-.0036	
	1.20							
	1.10							
	1.00	.074						
	.913	.17						
		.27						
		.37						
		.47						
		.57						
TURBINE DISCHARGE		.67		.00570		.00846		-.0022

- $\Delta = \delta_{SHROUD} - \delta_{WHEEL}$
- A POSITIVE (+) Δ IS AN INCREASE IN THE ROOM TEMPERATURE CLEARANCE EXISTING BETWEEN THE SHROUD AND WHEEL
- A NEGATIVE (-) Δ IS A DECREASE IN THE ROOM TEMPERATURE CLEARANCE EXISTING BETWEEN THE SHROUD AND THE WHEEL

C-3

TABLE LXX. - TURBINE WHEEL--TURBINE SHROUD CALCULATED DEFLECTIONS RELATIVE TO THRUST BEARING

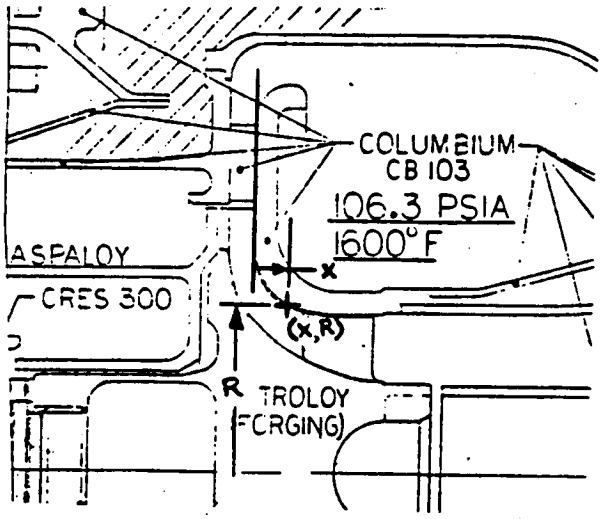

WHEEL MATERIAL		INCO 713 LC
	✓	ASTROLOY

OPERATING CONDITION

SOAKBACK:

12 MINUTES AFTER SHUTDOWN

TURBINE WHEEL AND SHROUD DEFLECTIONS

	RADIUS	X	δ_{WHEEL} (Axial)	δ_{WHEEL} (Radial)	δ_{SHROUD} (Axial)	δ_{SHROUD} (Radial)	CHANGE IN R.T. CLEARANCE Δ (AXIAL)	CHANGE IN R.T. CLEARANCE Δ (RADIAL)
TURBINE INLET	1.428	0 (ref)	.01793		.01394		-.0040	
	1.30		.01790		.01402		-.0039	
	1.20							
	1.10							
	1.00	.074						
	.913	.17						
		.27						
		.37						
		.47						
		.57						
TURBINE DISCHARGE		.67		.00600		.00346		-.0025

- $\Delta = \delta_{SHROUD} - \delta_{WHEEL}$
- A POSITIVE (+) Δ IS AN INCREASE IN THE ROOM TEMPERATURE CLEARANCE EXISTING BETWEEN THE SHROUD AND WHEEL
- A NEGATIVE (-) Δ IS A DECREASE IN THE ROOM TEMPERATURE CLEARANCE EXISTING BETWEEN THE SHROUD AND THE WHEEL

The final condition which was evaluated produced the maximum reduction in radial clearance at the turbine discharge end. In this condition, it was assumed that the engine was started during the soakback cycle, and that the trailing edge blade reached steady-state operating temperature prior to the temperatures changing elsewhere. This conservative assumption produces radial clearance reductions of 0.0030 in. and 0.0033 in., respectively, for the Inconel and Astroloy wheels, as shown in Tables LXXI and LXXII. These reductions are only slightly greater than those at steady-state operation.

A summary of the changes in the clearances between the shroud and wheel is shown for each condition in Table LXXIII. In addition to the variations at the turbine inlet and discharge, a point in the knee is also included.

Maximum Flange Loads

This section documents the calculated maximum allowable flange load for the Mini-BRU turbine discharge flange and the compressor inlet flange.

The same structural model used for the turbine plenum analysis was used to calculate the turbine discharge flange loads. The flange loads were transmitted from the recuperator through the connecting duct. The maximum flange loads were defined as the loads which will not produce deflections more than 0.001 in. along the turbine shroud. The stress levels due to the flange loads were insignificant.

The compressor inlet flange loads were also transmitted by the connecting duct with the recuperator due to thermal expansion and pressure in the duct. The inlet housing was modeled as shown in Figure 360 by utilizing program ISONON. Moment and shear were applied at the flange. The maximum change of face clearance of the compressor shroud was less than 0.001 in. due to the applied flange loading. There is no local yielding.

Table LXXIV summarizes the maximum allowable flange loads for turbine exhaust and compressor inlet.

Turbine Backshroud Stresses

The turbine backshroud, an item with a large thermal gradient, was analyzed for stress and deflection. The backshroud serves the dual function of controlling turbine backface windage losses and ducting the turbine end bearing cooling flow to the turbine gas stream.

TABLE LXXI. - TURBINE WHEEL--TURBINE SHROUD CALCULATED DEFLECTIONS RELATIVE TO THRUST BEARING

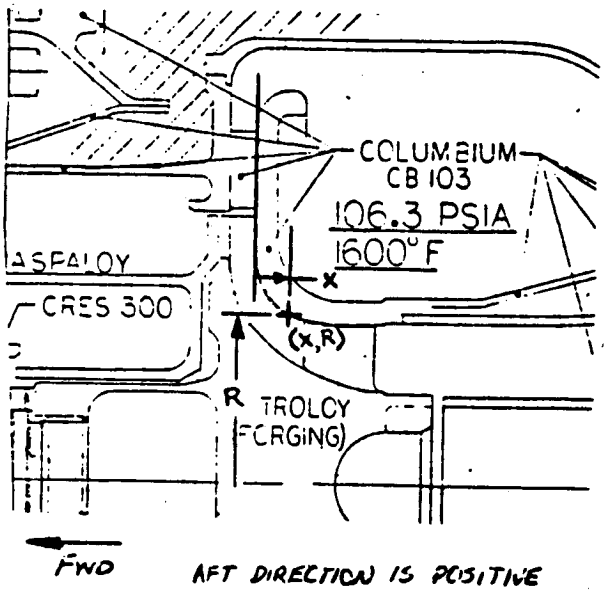

WHEEL MATERIAL	✓	INCO 713 LC
		ASTROLOY

OPERATING CONDITION

TRANSIENT CONDITION:

A START 12 MINUTES AFTER A SHUTDOWN

TURBINE WHEEL AND SHROUD DEFLECTIONS

	RADIUS	X	δ_{WHEEL} (Axial)	δ_{WHEEL} (Radial)	δ_{SHROUD} (Axial)	δ_{SHROUD} (Radial)	CHANGE IN R.T. CLEARANCE Δ (AXIAL)	CHANGE IN R.T. CLEARANCE Δ (RADIAL)
TURBINE INLET	1.428	0 (ref)						
	1.30							
	1.20							
	1.10							
	1.00	.074						
	.913	.17						
		.27						
		.37						
		.47						
		.57						
TURBINE DISCHARGE		.67		.00649		.00346		-.0030*

* THIS VALUE IS -.0028 WITH A START AT 4 MINUTES FOLLOWING SHUTDOWN

- $\Delta = \delta_{SHROUD} - \delta_{WHEEL}$
- A POSITIVE (+) Δ IS AN INCREASE IN THE ROOM TEMPERATURE CLEARANCE EXISTING BETWEEN THE SHROUD AND WHEEL
- A NEGATIVE (-) Δ IS A DECREASE IN THE ROOM TEMPERATURE CLEARANCE EXISTING BETWEEN THE SHROUD AND THE WHEEL

TABLE LXXII. - TURBINE WHEEL-TURBINE SHROUD CALCULATED DEFLECTIONS RELATIVE TO THRUST BEARING

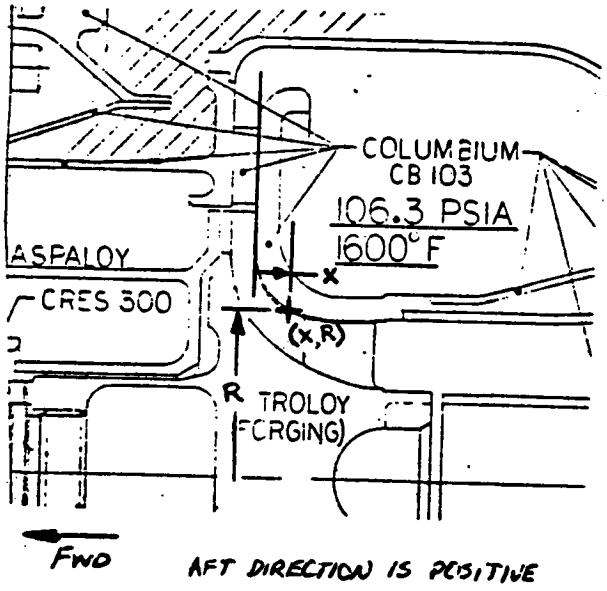

WHEEL MATERIAL		INCO 713 LC
	✓	ASTROLOY

OPERATING CONDITION

TRANSIENT CONDITION:
A START 12 MINUTES AFTER SHUTDOWN

TURBINE WHEEL AND SHROUD DEFLECTIONS

	Radius	X	δ_{WHEEL} (Axial)	δ_{WHEEL} (Radial)	δ_{SHROUD} (Axial)	δ_{SHROUD} (Radial)	CHANGE IN R.T. CLEARANCE Δ (AXIAL)	CHANGE IN R.T. CLEARANCE Δ (RADIAL)
TURBINE INLET	1.428	0 (ref)						
	1.30							
	1.20							
	1.10							
	1.00	.074						
	.913	.17						
		.27						
		.37						
		.47						
		.57						
TURBINE DISCHARGE		.67		.00671		.00346		-.0033 *

* THIS VALUE IS -.0030 WITH A START AT 4 MINUTES FOLLOWING SHUTDOWN

- $\Delta = \delta_{SHROUD} - \delta_{WHEEL}$
- A POSITIVE (+) Δ IS AN INCREASE IN THE ROOM TEMPERATURE CLEARANCE EXISTING BETWEEN THE SHROUD AND WHEEL
- A NEGATIVE (-) Δ IS A DECREASE IN THE ROOM TEMPERATURE CLEARANCE EXISTING BETWEEN THE SHROUD AND THE WHEEL

TABLE LXXIII. - SUMMARY OF CHANGES IN THE ROOM TEMPERATURE CLEARANCE AT THE TURBINE WHEEL-TURBINE SHROUD INTERFACE

Condition	Reference table	Turbine inlet		Knee		Turbine discharge	
		INCO713LC wheel	Astroloy wheel	INCO713LC wheel	Astroloy wheel	INCO713LC wheel	Astroloy wheel
Steady state	I, II	-0.0034	-0.0039	-0.0041	-0.0046	-0.0027	-0.0029
Shutdown	III, IV	-0.0049	-0.0054	-0.0052	-0.0058	-0.0027	-.0029
Soakback - 4 min. after shutdown	V, VI	-0.0049	-0.0052	(1)	(1)	-0.0024	-0.0026
Soakback - 12 min. after shutdown	VII,VIII	-0.0036	-0.0040	(1)	(1)	-0.0022	-0.0025
Start, 12 min. after shutdown	IX, X	(1)	(1)	(1)	(1)	-0.0030	-0.0033

(1) Not determined

A negative change is a decrease in the room temperature clearance existing between the shroud and the wheel

TABLE LXXIV. - MAXIMUM ALLOWABLE FLANGE LOAD

	Moment (in.-lb)	Shear (lb)	Axial load (lb)
Turbine exhaust flange	400	300	300
Compressor inlet flange	500	400	450

*When moment, shear and axial loads were applied simultaneously, the moment and shear should be reduced by 50 percent.

The calculated temperature distribution for the backshroud is shown in Figure 365. The corresponding stresses and deflections are shown in Figures 366 and 367.

SYSTEM INTEGRATION ANALYSIS

Introduction

In December 1974 a task was added to the program to conduct a system study. The study task was further subdivided into three tasks as follows:

Task I - System layout including duct sizing, thermal losses, duct and component insulation study and selection, and investigation of required material protection

Task II - System weight estimates, materials selection, controls analysis, and system transient analysis

Task III - Final report of study and publication of a Configuration Control Document (CCD) which would detail all that is known about the system

Figure 368 shows the logic network utilized for the task. Design criteria for required meteroid protection was obtained from the NASA while design information on insulation systems was provided by Thermo Electron Corp., Waltham, Mass. Due to the protection requirements associated with the use of refractory metals, a high vacuum test environment and an insulation system with a low outgassing characteristic were needed. Previous investigation had shown that only multifoil insulation would meet this requirement. Further, only multifoil insulation would meet the thermal loss goal with a reasonable weight penalty (i.e., 100 watts loss and <20 lbs for a ground system). Thermo Electron provided the insulation system for the MHW MHW HSA, therefore, they were selected for the design of a similar system for the Mini-BRU. Thermo Electron utilized the concept of wrapping 3/4-in. wide molybdenum foil with zirconia impregnated on one side on all the components and ducting to a thickness sufficient to limit thermal loss. Flanges would be welded, and the foil built up over them to minimize heat leaks. This system was utilized for the DoE BIPS Workhorse Loop.

Culmination of this effort was the design of a ducting system based on this insulation system, with duct thickness determined by stress-life-temperature consideration, meteoroid criteria, or physical size--whichever was the more conservative.

Task I - System Design

System design. - A number of layouts were completed to show a sample of the variety of component arrangements available to tailor the system to any application. A sample layout is shown in Drawing SKP32516. The final system layout was completed under the DoE BIPS program. Preliminary layouts were also completed for the Workhorse Loop (WHL), the Ground Demonstration System (GDS) and the Isotope Brayton Flight System (IBFS).

System insulation. -

(1) Insulation selection - Analyses were conducted to determine the optimum insulation for the components and ducts.

Thermo Electron Corporation (TECO), Linde of Union Carbide, and Johns-Manville, were contacted to ascertain if the low thermal loss goal of the Mini-Brayton System could be met. The losses predicted for a Min-K (fibrous) system manufactured by Johns-Manville were higher than desired, and the potential outgassing problem precluded the Min-K from further study. Linde indicated that the geometry was too difficult for successful installation of their insulation. Only TECO was confident that the multifoil could be successfully applied such that the thermal loss was limited to a few hundred watts. Consequently, TECO was engaged to consult with AiResearch on the application of multifoil to the Mini-BRU system.

Multifoil exhibited great promise because of the method of manufacture. The zirconia particles which separate the foils are sprayed on the foil and form weak mechanical bonds; hence a weak thermal bond. The insulation is particularly effective in a hard vacuum by limiting radiation. Typically, 60 to 100 foil layers are used.

(2) Multifoil discussion -

(a) Multifoil is a high temperature, vacuum insulation requiring pressures of 10^{-5} Torr or less to be effective.

(b) Multifoil cannot bear mechanical loads. It is composed of 0.0005 to 0.001 in. thick metal foil separated by a sparse layer of zirconia. The zirconia particles must be sparsely distributed to preclude conduction losses.

(c) The quality of the insulation is dependent on the installation (i.e., method of application). Seams or edges are to be avoided as the loss can range from 0.1 to 0.3 w/cm of seam.

(d) Differential thermal expansion of the insulation must be considered. This is the reason the layers are 0.004 in. thick.

(e) The conductivity of the insulation does not seem to be a function of the foil chosen.

(f) The loss through penetrations will be equal to double the loss of the item which penetrates.

(g) Penetration for mounts must be carefully designed using ceramics where possible to cut the direct conduction path. (This is important regarding the recuperator mounts.)

(h) Losses in the 1400°F temperature range were estimated to be 0.01 w/cm^2 for 60 to 100 layers of foil.

(i) Edge losses can be reduced by factors of 2 to 5 by using interlocking tabs which will thicken the ends.

(j) The insulation must frequently be held in place by an outside structural layer (skin) or by thin wires through the insulation.

(k) The plating-substrate (an advanced technology TECO developed approach) method could eliminate all joint and minimize the losses to the theoretical values.

(m) Effective edge designs are the beveled:

These designs are especially effective when interlocking or overlapping of foils are used.

(n) The losses of a given geometry cannot be estimated until the installation has been made because of the uncertainty in edge loss and the iteration required to determine the assembly procedure.

(o) All point loadings (sharp corners, instrumentation running along surfaces, flanges, etc.) must be reduced through the use of contoured sheet metal to create a smooth surface.

(3) Component insulation -

(a) Recuperator - Loss from the recuperator was estimated to be 70 watts through the foil plus 70 watts due to axial effects. Prime areas of concern are the mounts and joints between the insulation pieces. Stainless steel appears to be a viable candidate because of the lower life requirement of the GDS and the lower axial conduction potential. Trial application with a mockup will be required to achieve the best insulation configuration. Interlocking of the foils at edges will minimize these losses.

Instrumentation leads will be routed from the hot end of the recuperator to the cold end along the outer shell for egress from the insulation. This will allow accurate performance measurement with minimum heat loss penalty.

Mounts must be designed to minimize thermal loss. Candidate designs are strap-type mounts, cold end only mounts, ceramic separators between hot and cold parts of the mounts, or a combination of the above. Ceramics must be used in compression only, and an interesting potential candidate, if the technology exists, is metallized zirconia. A design iteration between the mount and insulation designers is required to minimize this thermal loss.

(b) Mini-BRU - The insulation between the turbine plenum and compressor collector was fabricated as a cylinder and a disk with a stepped joint configuration. The outside of the turbine plenum was insulated in place on the WHL by wrapping.

(c) Ducting - Ducting was insulated by a zirconia impregnated foil tape 3/4 to 2 in. wide. Ducts were wrapped in a helical fashion to the weld joints. A thickness of 60 to 100 layers was used; the joints would be taped subsequent to the welding. This technique was developed insitu as the WHL was assembled.

TECO has calculated the following losses for the GDS without losses due to instrumentation (20 to 100 W_t) or support structure.

Heat Sources (2)	480 W
Engine Alternator	24 W
Recuperator	71 W
Plumbing	64 W
TOTAL	639 W

If the advanced technology plating technique is used, these losses could be reduced to 470 W.

Armor model. - The equation below was used to estimate the armor requirement for the Mini-Brayton System. The input for the equation was defined by NASA. The duct area to be protected was assumed to be the total circumferential area of all of ducting and headers including an estimate of the radiator ducting based on the Mini-BRU Preliminary Design Study.

$$t_a = \frac{a}{2.54}\,\gamma\left(\frac{6}{\pi}\right)^{1/3}\rho_p^{1/3}\left(\frac{62.43\rho}{\rho_t}\right)^{\Phi}\left(\frac{\bar{v}}{c}\right)^{\theta}\left[\frac{\alpha A\tau}{-\ell nP(o)}\right]^{\frac{1}{3\beta}}\left[\frac{2}{3n\theta\beta+2}\right]^{\frac{1}{3\beta}}$$

where T_a = required single material armor thickness, in.

a = thin plate and spall adjustment, 1.75

γ = 2 if experimental value is unavailable

ρ_p = meteoroid particle density, gm/cc

ρ_t = radiator (target) material density, lb/ft^3

Φ = 1/2

$\bar{v}$ = average meteoroid velocity, ft/sec

$c = 12\sqrt{E_t g/\rho_t}$ where E_t is Young's modulus at radiator operating temperature, $lb/in.^2$, and g is 32.2 ft/sec^2

θ = 2/3

α =
constants obtained from flux distribution curve
β =

A = vulnerable target area of radiator, ft^2

τ = mission time in days

P(o) = design probability of no critical damage to radiator system

n = 1 (valid for oblique penetration dependent upon the normal component of velocity

This approach was used with the 1969 NASA Meteoroid Environmental Model (NASA SP-8013). This model specifies the following:

ρ_p = 0.44 gm/cc

v = 65,616 ft/sec (20 km/sec)

$\alpha = 3.12 \times 10^{-11}$ gm^{β}/ft^2 day

From the above equation for the required material thickness, it can be seen that the thickness is proportional to $\rho^{-1/6} E^{-1/3}$, where ρ and E are the density and modulus of elasticity of the target material, respectively. A comparison of typical thickness requirements for aluminum, beryllium, and stainless steel is shown below to illustrate the significance of the correct material selection.

	ρ lb/ft^3	E psi	Thickness inch	Weight / Weight of Aluminum
Aluminum	174	10×10^6	0.1	1.00
Beryllium	116	42×10^6	0.066	0.44
Stainless Steel	490	29×10^6	0.059	1.67

This chart indicates the potential weight advantage of beryllium, if it can be shown to be an effective armor, i.e., does not shatter.

System pressure drop. - The nominal size and configuration of the ducting were based on SKP32516 for the GDS. This design minimizes duct length and number of turns to produce the desired low pressure drop design. Pressure drop in the compressor inlet and radiator inlet ducts was included in the radiator design problem. The reference GDS cycle is shown in Figure 369.

Pressure drop in the ducting was based on the friction factor data of Nikuradse as a function of Reynolds number and surface roughness. Turning loss was calculated by the SAE method which expresses turning loss as a function of angle and Reynolds number. Surface roughness was assumed to be 63 micro-inches for every case.

Table LXXV indicates the weight and pressure drop of the ducting for the reference GDS cycle. The radiator ducting weight and pressure drop are shown for reference only as this is considered to be part of the radiator design. The design pressure drop goal of the ducting in the reference cycle is 0.0042--note that the above described ducting pressure drop is less than the design goal. The allowable stress level is based on the peak pressure at the three HSA case.

Based on the ducting described above, it appears that the radiator skin can be used as a bumper for the ducting. If the bumper is assumed to be as valuable as three times as much armor placed on the ducting, a 0.040 in. thick aluminum fin and similar covered ends would give the ducting a reliability of 99 percent for a five-year mission. The beryllium can placed around the heat source would give the heat exchanger a similar reliability. The recuperator would also have a 0.99 reliability for the five-year mission.

TABLE LXXV. - DESIGN PARAMETERS FOR SYSTEM DUCTING

Duct Location	Material	Allowable stress (KSI)	Temperature (°R)	Wall thickness	Reynold's number	Velocity (FPS)	Inside diameter	Weight (lb)	ΔP/P
Compressor Discharge b	SS	30	610	0.023	74200	10.0	2.25	1.0	0.00014
Recuperator Discharge	Hast X	2	1757	0.052	32600	29.0	2.25	2.0	0.00072
Heat Source Inlet	Hast X/CB103	2	1757	0.038	26200	37.0	1.4	0.85	0.00017
Heat Source Discharge	CB103	2	2060	0.038	23500	44.0	1.4	0.64	0.00014
Turbine Discharge	Hast X/CB103	2	1778	0.052	33000	45.0	2.25	2.7	0.0018
Total								7.2	0.0029
Radiator Ducting	SS	30	610/480	0.023	90000	15		6.0	0.0006

The resultant system reliability will be approximately 0.96 for a five-year mission. Actual reliability will be greater when the thickness of the ducting is entered into the reliability computation. The ducting thickness was eliminated, thus far, from the reliability considerations as the damage to the insulation system and its detrimental effect on system performance is as yet unknown without extensive analysis.

Task II - System Analysis

System reliability. - A reliability analysis of the entire IBFS was undertaken and completed. An existing computer program named PREDICTOR was used to determine electronic and electrical reliability parameters. This program uses MIL-HDBK-271A, MIL-HDBK-217B, and RADC notebook methods for reliability predictions. The capability of the program is such that as the program progresses one can:

(1) Update circuits, as control circuits are redefined, and easily add or remove components from the reliability input

(2) Perform redundancy, duty cycle, etc. studies to enhance the reliability

(3) Investigate various reliability modes (i.e., satellite orbital, missile launch, manned orbital, etc.)

(4) Perform failure modes and effects analyses

(5) Maintain visibility of parts using the program option PARTS-LIST which lists piece part count, price, vendor information, etc.

(6) Perform maintainability studies should a manned mission or repair capabilities study warrant it.

(7) Investigate effects of extreme heat or cold easily. The program automatically performs the tedious task of determining electronic and electrical reliabilities with a simple set command on ambient temperature.

Transient analysis. - A transient simulation was modeled from an existing computer program to analyze system performance during start-up, shutdown, and step changes in user load. It is intended that this program should be used as an aid to:

(1) Define thermal transients which are imposed on the heat exchanger to be used as an aid in performing the heat exchanger stress analysis.

(2) Define a control system for use during start-up which is compatible with the heat exchanger [per above Item (1)].

(3) Define control gains and limits which are adequate to control the system from the considerations of stability, droop, and engine protection.

(4) Define limits on the alternator in terms of power margin necessary to prevent overspeed.

(5) Define shutdown transients in terms of how rapidly the engine passes through critical speeds, etc.

A sample of the output from this program is given for a preliminary number of conditions. A sample of a transient system response is shown in Figure .

Task III - Configuration Control Document

A Configuration Control Document (CCD) was prepared and published and subsequently revised several times under the DoE BIPS program.

CLOSURE

A Mini Brayton Rotating Unit was designed, fabricated and conformance tested in accordance with the contractual requirements. This unit was subsequently transferred to the DoE BIPS program, Contract No.EY-76-C-03-1123 and tested in a simulated space environment. Refer to Reference 44 for details of this program.

A second unit was fabricated but was not tested; it remains on standby for future test requirements.

All analyses conducted on the unit indicate a conservative, reliable design completely capable of functioning for a 10-year mission life in a space environment in either a superalloy or refractory configuration.

SYMBOLS

A	-	Area, inches^2
B	-	Blockage or percent blocked area
b	-	Meridional passage height, inches
C_B	-	Backface clearance (in.)
C_p	-	Static pressure recovery, $(P_{S_2}-P_{S_1})/(P_2-P_{S_1})$
c_p	-	Constant pressure specific heat
C_V	-	Constant volume specific heat, Btu/lb-°R
L	-	Diffuser meanline flowpath length, inches
M	-	Mach number
MW	-	Molecular weight
N	-	Shaft speed, rpm
P	-	Pressure (psia)
Q	-	Streamline entropy function
R	-	Radius (in.)
Re	-	Reynold's number, $W\mu R_T$
T	-	Temperature (°R)
ΔT	-	Temperature rise, °R
V	-	Velocity, ft/sec
W	-	Mass flow (lb_m/sec)
w	-	Normal distance between adjacent blade surfaces, inches
X	-	Axial length
β_s	-	Swirl angle, degrees
γ	-	Ratio of specific heats, C_p/C_v
δ	-	Normalized pressure, P/14.696
δ^*	-	Boundary layer displacement thickness, inches
η	-	Adiabatic efficiency, $\left[(P/P_1)^{\frac{\gamma-1}{\gamma}}-1\right] \Big/ \left[T/T_1-1\right]$
θ	-	Normalized temperature, T/518.688
μ	-	Dynamic viscosity, lb_m/ft-sec

SYMBOLS (Contd)

Subscripts:

eff	-	effective
geo	-	geometric
OA	-	overall
m	-	meridional
s	-	static condition
t	-	throat
T	-	total condition
u	-	tangential direction
1	-	impeller inlet
2	-	impeller exit
3	-	diffuser exit

Superscript:

'	-	relative condition

REFERENCES

1. AiResearch Internal Memorandum: ES:CJP:0038:082174.

2. Johnsen, Irving A., et al, "Aerodynamic Design of Axial-Flow Compressors," NASA SP-36.

3. Runstadler, P., "Pressure Recovery Performance of Straight-Channel, Single-Plane Divergence Diffusers at High Mach No.'s."

4. Schlichting, H., K. Gersten, "Calculation of Flow in Axisymmetrical Diffusers with the Aid of the Boundary Layer Theory," Braunschweig; "Zeitschrift fur Flugwissenschatten."

5. Carmichael, A.D., and G.N. Pustintsev, "The Prediction of Turbulent Boundary Layer Development in Conical Diffusers," J. Mechanical Eng. Science, December 1966.

6. McMillan, O.J. and J.P. Johnston, "Performance of Low-Aspect-Ratio Diffusers with Fully Developed Turbulent Inlet Flows Part I - Some Experimental Results," ASME 73-FE-12.

7. Fox, R.W., and S.J. Kline, "Flow Regime Data and Design Methods for Curved Subsonic Diffusers," Journal of Basic Engineering, Vol. 84, Series D, September 1962.

8. Lee, J.B., and E.A. Zanelli, "Gas Turbine Compressor Development Program for 1.5/3 kW Generator Set," AiResearch Report 75-311130, December 1975.

9. Truckenbrodt, E., "A Method of Quadrature for Calculation of the Laminar and Turbulent Boundary Layer in Case of Plane and Rotationally Symmetrical Flow," NACA TM-1379.

10. Katsanis, T., and W.D. McNally, "Fortran Program for Calculating Velocities and Streamlines on a Blade-to-Blade Stream Surface of a TMndem Blade Turbomachine," NASA TN D-5044, March 1969.

11. Aerodynamic Design of Axial-Flow Compressors, NASA SP-36, 1965.

12. Weigel, C., and C.L. Ball, "Reynolds Number Effect on Overall Performance of a 10.8-Centimeter (4.25 in.) Sweptback-Bladed Centrifugal Compressor," NASA TN D-6640, January 1972.

13. Wasserbauer, C.A., M.G. Kofskey, and W.J. Nusbaum, "Cold Performance Evaluation of a 4.59-inch Radial-Inflow Turbine Designed for a Brayton-Cycle Space Power System," NASA TN D-3260, February 1966.

14. Kofskey, M.G., and D.E. Holeski, "Cold Performance Evaluation of a 6.02-inch Radial Inflow Turbine Designed for a 10-KW Shaft Output Brayton Cycle Space Power Generation System," NASA TN D-2987, February 1966.

15. Futral, S.M., Jr., and C.A., Wasserbauer, "Off-Design Performance Predictions with Experimental Verifications for a Radial-Inflow Turbine," NASA TN D-2621, February 1965.

16. Kofskey, M.G., and C.A. Wasserbauer, "Experimental Performance Evaluation of a Radial-Inflow Turbine over a Range of Specific Speeds," NASA TN D-3742, November 1966.

17. Kofskey, M.G., and W.J. Nusbaum, "Effects of Specific Speed on Experimental Performance of a Radial-Inflow Turbine," NASA TN D-6605, February 1972.

18. Nusbaum, W.J., and M.G. Kofskey, "Cold Performance Evaluation of 4.97-inch Radial-Inflow Turbine Design for Single-Shaft Brayton Cycle Space-Power System," NASA TN D-5090, March 1969.

19. Nusbaum, W.J., and M.G. Kofskey, "Cold Performance Evaluation of a 4.54-inch Radial-Inflow Turbine over a Range of Reynolds Numbers," NASA TN D-3835, February 1967.

20. Rohlik, H.E., "Analytical Determination of Radial Inflow Turbine Design Geometry for Maximum Efficiency," E-3996.

21. Rohlik, H.E., and M.G. Kofskey, "Recent Radial Turbine Research at the NASA Lewis Research Center," ASME 72-GT-42, 1972.

22. Futral, S.M., and D.E. Holeski, "Experimental Results of Varying the Blade-Shroud Clearance in a 6.02-inch Radial Inflow Turbine," NASA TN D-5513, 1970.

23. Futral, S.M., and C.A. Wasserbauer, "Experimental Performance Evaluation of a 4.59-inch Radial-Inflow Turbine with and Without Splitter Blades," NASA TN D-7015, 1970.

24. Nusbaum, W.M., and M.G. Kofskey, "Radial-Inflow Turbine Performance with Exit Diffusers Designed for Linear Static Pressure Variation," TM X-2357, 1971.

25. Kofskey, M.G., and M.E. Haas, "Effect of Reducing Rotor Blade Inlet Diameter on the Performance of a 11.66-Centimeter Radial-Inflow Turbine," NASA TMX-2730, March 1973.

26. Stewart, W.L., W.J. Whitney, and R.Y. Wong, "A Study of Boundary-Layer Characteristics of Turbomachine Blade Rows and Their Relation to Overall Blade Loss," ASME Paper No. 59-A023, January 1960.

27. Hiett, G.F., and I.H. Johnston, "Experiments Concerning the Aerodynamic Performance of Inward Flow Radial Turbines," Institution of Mechanical Engineers Paper 13, April 1964.

28. Watenabe, I., I. Ariga, and T. Mashimo, "Effects of Dimensional Parameters of Impellers on Performance Characteristics of a Radial-Inflow Turbine," ASME Paper No. 70-GT-90, May 1970.

29. Zweifel, O., "The Spacing of Turbo-Machine Blading, Especially with Large Angular Deflection," Brown-Boveu Review, Vol. 32, 1954.

30. Stewart, W.L., "Analysis of Two-Dimensional Compressible-Flow Loss Characteristics Downstream of Turbomachine Blade Rows in Terms of Basic Boundary-Layer Characteristics," NACA TN 3515, July 1955.

31. Katsanis, T., "Fortran Program for Calculating Velocities and Streamlines on a Blade-to-Blade Stream Surface of a Turbomachine," NASA TN D-5425, 1968.

32. Rogo, C., "Development of a High Tip Speed Radial Turbine System for a Small Turboalternator," SAE Paper No. 710552, June 1971.

33. Amann, C.A., and D.W. Dawson, "The Power Turbine and Its Diffuser," SAE Paper No. 690032, June 1969.

34. Sovrau, G., and E.D. Klomp, "Experimentally Determined Optimum Geometries for Rectangular, Conical, or Annular Cross-Sections," General Motors Research Publication GMR-511, November 1965.

35. Adenubi, S.O., "Effects of Axial Turbomachine Type Discharge Conditions on Performance of Annular Diffusers - An Experimental Study," Stanford University, M.E. Dept Report PD-16, April 1972.

36. Kofskey, Milton G., D.E. Holesk, "Cold Performance Evaluation of a 6.02-Inch Radial Inflow Turbine Designed for a 10 Kilowatt Shaft Output Brayton Cycle Space Power Generation System," NASA TND-2987, February 1966.

37. Wasserbauer, C.A., M.G. Kofskey, W.J. Nusbaum, "Cold Performance Evaluation of a 4.59-Inch Radial Inflow Turbine Designed for a Brayton Cycle Space Power System," NASA TND-3260, February 1966.

38. Nusbaum, W.J., and M.G. Kofskey, "Cold Performance Evaluation of a 4.97-Inch Radial Inflow Turbine Designed for Single Shaft Brayton Cycle Space Power System," NASA TND-5090, March 1969.

39. Nusbaum, W.J., and C.A. Wasserbauer, "Experimental Performance Evaluation of a 4.59-Inch Radial Inflow Turbine Over a Range of Reynolds Number," NASA TND-3835, February 1967.

40. Sorran, G., and E.D. Klomp, "Experimentally Determined Optimum Geometries for Rectangular Conical or Annular Cross-Sections," General Motors Research Publications GMR-511, November 1965.

41. Ikeda, K., "Mini-Brayton Rotating Unit Alternator Steady-State and Transient Thermal Analysis," AiResearch Report 74-10930, October 30, 1974.

42. Fink, Donald G., John M. Carroll, "Standard Handbook for Electrical Engineers", 10th edition, 1969, McGraw-hill, N.Y.

43. Clarke, Edith, "Circuit Analysis of AC Power Systems", Vol. II, John Wiley and Sons, New York, 1950.

44. "Brayton Isotope Power System Phase I Final Report", AiResearch Manufacturing Company of Arizona, Report No. 31-2919, July, 1978.

45. Dobler, Fix and L.G. Miller, Mini-Brayton Rotating Unit Foil Bearing Development, NASA CR-159442, 1978.

DISTRIBUTION LIST

Recipient	Address
Attention: J.H. Dunn (MS 500-202) (15) L.W. Schopen (MS 500-305) (1) Technology Utilization (MS 3-19) (1) Library (MS 60-3) (2) W.D. Klopp (MS 105-1) (1) R.H. Titran (MS 105-1) (1) S.H. Gorland (MS 501-7) (1)	NASA Lewis Research Center 21000 Brookpark Road Cleveland, OH 44135
Attention: J.P. Mullin (Code RPP) (1) L. Holcomb (Code RPI) (1)	National Aeronautics and Space Administration Washington, D.C. 20546
Attention: Accessioning Department (30)	Nasa Scientific & Technical Information Facility P.O. Box 8757 Balt/Wash International Airport, MD 21241
Attention: Library (1)	NASA - Marshall Space Flight Center Marshall Space Flight Center, AL 35812
Attention: Library (1)	NASA Flight Research Center P.O. Box 273 Edwards, CA 93523
Attention: Library (1)	NASA-Ames Research Center Moffitt Field, CA 94035
Attention: Library (1)	NASA-Goddard Space Flight Center Greenbelt, MD 20771
Attention: Library (1)	NASA-Langley Research Center Langley Station Hampton, VA 23365
Attention: Library (1) A. Redding (1)	Jet Propulsion Laboratory 4800 Oak Grove Drive Pasadena, CA 91103
Attention: D. Kenney (MS 82-2200) (1)	ERDA Division of Nuclear Research Washington, D.C. 20545

Recipient	Address
Attention: Library (1)	Air Force Systems Command Aeronautical Systems Division Wright-Patterson Air Force Base OH 45438
Attention: C. Alexander (1)	Battelle Memorial Institute 505 King Avenue Columbus, OH 43201
Power Infrmation Center	University of Pennsylvania 3401 Market Street, Room 2107 Philadelphia, PA 19104
Attention: Library (1)	The Boeing Company Aero-Space Division Box 3707 Seattle, WA 98124
Attention: Library (1) D. Wein (1)	General Electric Company Missile & Space Vehicle Dept. 3198 Chestnut Street Philadelphia, PA 19104
Attention: E.C. Kruger (1)	Sundstrand Energy Systems 4747 Harrison Avenue Rockford, IL 61101
Attention: Frank Welling (1)	Naval Ship Engineering Center Hyattsville, MD 20782
Attention: R.L. Statler (1) R. Beard (1)	Naval Research Laboratory Code 6623 Washington, D.C. 20375